

Modelling the Endothelial Cell Response to Fluid Flow

Richard J. Allen

Centre for Mathematics and Physics in the Life Sciences
and Experimental Biology, University College London

Supervisors: Professor David Bogle and Professor Anne Ridley

Thesis submitted for the degree of Doctor of Philosophy (Ph.D.)
at University College London

November 2008

I, Richard John Allen, confirm that the work presented in this thesis is my own. Where information has been derived from other sources, I confirm that this has been indicated in the thesis.

A handwritten signature in blue ink that reads "R.J. Allen". The signature is written in a cursive style with a large initial 'R' and 'A'.

Richard J. Allen

Acknowledgments

This Ph.D. was carried out between October 2005 and October 2008 at the Centre for Mathematics and Physics in the Life Sciences and Experimental Biology (CoMPLEX), University College London (UCL). It was funded by the Engineering and Physical Science Research Council (EPSRC).

This work was supervised by Professor David Bogle (UCL) and Professor Anne Ridley (King's College London). I take this opportunity to thank both of my supervisors for their support and insights. I also thank Dr. Konstantinos Lykostratis (a previous Ph.D. student of Professor Ridley who studied shear stress signalling in endothelial cells (Lykostratis, 2005)) whose thesis motivated some of the research reported in chapters 5 and 6.

The Brownian dynamic modelling presented in chapter 3 was carried out in the Kamm Laboratory, Massachusetts Institute of Technology (MIT) courtesy of a Bogue scholarship awarded by UCL. I thank Professor Kamm for hosting my visit and Tae Yoon Kim for the fruitful collaboration.

Lastly I thank my family for their consistent and unwavering support through many years of education.

Abbreviations

ADP - Adenosine Diphosphate
Arp - Actin Related Protein
ATP - Adenosine Triphosphate
BD - Brownian Dynamic
BIR - Boundary Integral Representation
CCA - Common Carotid Artery
CPM - Cellular Potts Model
DPAB - Dense Peripheral Actin Band
EC - Endothelial Cell
ECM - Extra Cellular Matrix
FA - Focal Adhesion
FAK - Focal Adhesion Kinase
GAP - GTPase Activating Protein
GDP - Guanosine Diphosphate
GEF - Guanine Nucleotide Exchange Factor
GTP - Guanosine Triphosphate
LDLs - Low Density Lipo-protein
MLC - Myosin Light Chain
MLCK - Myosin Light Chain Kinase
MLCP - Myosin Light Chain Phosphatase
MYPT - Myosin Phosphatase Target Subunit
MTOC - Microtubule Organising Centre
PDE - Partial Differential Equation
WASP - Wiskott-Aldrich Syndrome Protein
WAVE - WASP family Verprolin-homologous protein

Abstract

In vitro endothelial cells respond to fluid flow by elongating in the direction of flow. How the mechanical signal is transformed into an organised and directed response is poorly understood.

The most studied and crucial aspects to this response are; actin filament alignment, mechano-transduction, signal transduction, Rho GTPase localised activation and lamellipodium formation. The goal of this project is to understand how these separate facets interact and lead to a coordinated response.

The flow is modelled over a 3D virtual cell, which naturally gives the force the flow exerts on the cell surface via a boundary integral representation. This force is coupled to a Kelvin-body model of mechano-transduction which links, via a focal adhesion associated protein, Src, to a partial differential equation model (PDE) of the Rho GTPases Rac and Rho. The PDEs are integrated over a 2D projection of the 3D cell giving a time course for protein concentration at any point in the cell. It is demonstrated that a mechano-transducer that can respond to the normal component of the force is likely to be a necessary (though perhaps not sufficient) component of the signalling network.

In some processes cross talk between the GTPases is thought to be important in forming spatially-segregated zones of activation, for example in the front and back of migratory cells. This research shows that local signalling in endothelial cells could be initiated by the force normal to the surface of the cell and maintained by limited diffusion. Modelling indicates the EC signalling response to fluid flow may be attenuated by a change in morphology.

Rac and Rho activation and deactivation are validated against experimentally reported time courses that have been taken for whole cell averages. However it will be demonstrated that these time courses do not characterise the process and therefore there is a need for more quantitative local measure of protein activation.

Contents

Acknowledgments	3
Abbreviations	4
Abstract	5
List of Figures	7
1 Introduction	8
1.1 Endothelial Cell Polarisation and Alignment	10
1.1.1 Spatial Heterogeneity	11
1.2 Project Goals	12
1.3 Thesis Structure	12
2 Prior Cytoskeleton Modelling	14
2.1 Cytoskeleton Biology	14
2.1.1 Microtubules	15
2.1.2 Intermediate Filaments	16
2.1.3 Actin Filaments	16
2.1.4 The Mechanics of the Cytoskeleton	17
2.2 The Cytoskeleton as a Continuum	19
2.2.1 Fluid Mechanics Approach	19
2.2.2 Results and Criticism	21
2.2.3 Stress-Induced Alignment	23
2.3 Integro-Differential Modelling	25
2.4 Extending the Integro-Differential Model	27
2.4.1 Extended Model	28
2.4.2 Stability Analysis	30

2.4.3	Discussion of Integro-differential Model	36
3	Brownian Dynamic Modelling of Arp2/3 complex nucleated Actin Polymerisation	39
3.1	Lamellipodia	39
3.1.1	Regulation of Lamellipodia	40
3.1.2	Force Induced by Actin Polymerisation	43
3.2	Modelling of lamellipodium extension	43
3.2.1	Brownian Dynamics	45
3.3	Results of the BD model of membrane extension	52
3.4	BD Model of Membrane Extension - Discussion	61
4	Modelling the Flow over a Single 3D Cell	65
4.1	Stokes Flow	65
4.2	Flow in an Artery	67
4.3	The Boundary Integral Representation	70
4.4	Solution Strategy	76
4.5	Numerical Implementation of the Boundary Integral Representation	77
4.5.1	Discretising the surface	78
4.5.2	Integrating over a Surface Element	80
4.5.3	Solving the linear problem	84
4.5.4	Flow Parameters	86
4.6	Results - Flow over a single Cell	87
5	Modelling Endothelial Cell Mechano-transduction	96
5.1	Candidate Mechano-transducers	96
5.1.1	Ion Channels	97
5.1.2	Glycocalyx-Cytoskeleton transduction	98
5.1.3	Focal Adhesions as Signalling Centres	99

5.2	Modelling Mechano-transduction	101
5.2.1	Modelling the mechanical effect of normal surface force	102
5.2.2	Transducing the Mechanical Signal	105
6	Modelling Rho GTPase Activity	112
6.1	Rho GTPase Background	112
6.1.1	Rho GTPase Regulation	112
6.1.2	Rho GTPase Targets	112
6.1.3	Rho GTPase Crosstalk	115
6.2	Modelling the Role of GTPases in Endothelial Cell Elongation	118
6.3	Rho GTPase Model - Results	124
7	Conclusion	131
7.1	Project Goals	131
7.2	Endothelial Cell Polarisation and Elongation: A Hypothetical Overview	137
7.3	Experimental Evidence and Model Validation	138
8	Future Work	142
8.1	Multiple Cells	142
8.2	Cellular Potts Modelling	143
8.3	Other Research Directions	146
	References	148
	Index	162

List of Figures

1.1	Endothelial cell dimensions	9
1.2	Pathogenesis of atherosclerosis	10
1.3	The modules of endothelial cell polarisation	11
2.1	Microtubule structure	15
2.2	Filament alignment in EC in response to fluid flow	17
2.3	Tensegrity structure.	18
2.4	Poiseuille flow	20
2.5	2D representation of an endothelial cell	20
2.6	Continuum model results	21
2.7	Integro-differential model of filament alignment	30
2.8	Standard linear stability analysis	33
2.9	Uniform block function	34
2.10	Plot of $\text{Det } J$ of the integro-differential system	35
2.11	Stability of the Isotropic State	36
3.1	Lamellipodia extension	40
3.2	Actin filament	41
3.3	Arp2/3 nucleated actin branching	42
3.4	Brownian ratchet model of membrane extension	44
3.5	Binding in the BD model	48
3.6	Simulated Arp2/3 branching	49
3.7	Severing the simulated network	51
3.8	Membrane position in BD model	53
3.9	Initial conditions in the BD model	54
3.10	BD simulation at 0.51mM	55
3.11	BD simulation at 0.70mM	56

3.12	BD simulation at 0.51mM with severing	56
3.13	BD simulation at 0.38mM with severing	57
3.14	BD simulation at 0.59mM with severing	58
3.15	BD simulation at 0.51mM with severing	58
3.16	BD simulation at 0.12mM with severing	59
3.17	BD simulation at 0.59mM with severing	60
3.18	BD simulation at 0.29mM with severing	61
3.19	BD simulation at 0.019mM with severing	62
4.1	Poiseuille flow in an artery	67
4.2	Flow in a cylindrical artery	68
4.3	Discretisation of the plane	78
4.4	The discretised cell surface	79
4.5	Mapping a surface element to the standard triangle	80
4.6	Singularity of the free space Green's function	82
4.7	Integrating a singular triangle	83
4.8	The regularised singularity of the Green's function	84
4.9	Convergence of the iterative arnoldi method	87
4.10	Total shear stress as a function of μk	88
4.11	Maximum shear stress as a function of μk	89
4.12	Streamlines of the flow over a single cell	90
4.13	Convergence of the numerical method	92
4.14	Shear stress on the cell surface	93
4.15	Unit force on the cell viewed from aside	94
4.16	Unit force on the cell from above	94
5.1	The integrin complex	100
5.2	Kelvin body model	103
5.3	Mechano-transducer extension	106

5.4	Src activation due to mechano-transducer extension	107
5.5	Approximation to the mechano-transducer extension results	108
5.6	Fold Src increase as a whole cell average	110
5.7	Distribution of active Src in a single cell	111
6.1	Rho GTPase regulation	113
6.2	Rho GTPase targets	114
6.3	MLC regulation and effectors	115
6.4	Speculative heuristic model of EC elongation	116
6.5	Solution of heuristic model of EC morphological change.	117
6.6	Proposed interaction of Rho, Rac and Src	119
6.7	Diffusion on the hexagonal lattice	122
6.8	Diffusion on the cell boundary	123
6.9	Simulated Rac-GTP distribution	125
6.10	Simulated whole cell average of Rac-GTP, Rac GEF and Rac GAP . .	125
6.11	Rac-GTP distribution with altered diffusion characteristics	126
6.12	Whole cell average of Rac-GTP distribution under altered diffusion .	127
6.13	Activation of Rac in a cell aligned parallel to the flow	128
6.14	Activation of Rac in a cell aligned perpendicular to the flow	129
6.15	Whole cell average of Rac activation in three different morphologies .	129
6.16	Whole cell average of Rho activation in three different morphologies .	130
7.1	FA Maturation	136
8.1	Flow over four cells	142
8.2	Cellular Potts Model of a Single Cell	145
8.3	Cellular Potts Model of six cells	145

1 Introduction

The focus of this project is the study of how endothelial cells (ECs) respond to fluid flow. Following the onset of flow ECs undergo a wide variety of intra-cellular signalling including: ion channel activation, MAPK (mitogen activated protein kinase) signalling, NF- κ B (nuclear factor kappa B) activation, Rho GTPase activation, integrin activation, PECAM-1 (platelet endothelial cell adhesion molecule) activation and activation of phosphoinositide 3-kinases (Wojciak-Stothard & Ridley, 2003; Tzima *et al.*, 2001, 2002; Davies, 1995). *In vitro* the signalling response initiates a structural reorganisation of the following: cytoskeleton, organelle localisation and focal adhesions, which results in mechanical stiffening, flattening of the cell and alignment of the cell in the flow direction (Davies *et al.*, 1997; Ballerman *et al.*, 1998; McCue *et al.*, 2006; Wojciak-Stothard & Ridley, 2003; Tzima *et al.*, 2002). Focal adhesions, which attach the cell to the extra-cellular matrix, become aligned with the flow. However the total area of the cell adhered to the extra-cellular matrix remains approximately constant (Davies *et al.*, 1994), however it is also reported that adherence to the extra-cellular matrix is increased in response to fluid flow (Ballerman *et al.*, 1998).

The EC response to laminar fluid flow is referred to as a shear-stress activated process (Goldfinger *et al.*, 2008; Tzima *et al.*, 2001, 2002, 2005; Wojciak-Stothard & Ridley, 2003; Hoger *et al.*, 2002). In this thesis it will be argued that the normal force may complement the shear-stress activated signalling pathways. However the role of shear-stress signalling in the EC response to laminar fluid flow should not be underestimated.

In order to sense the direction of fluid flow ECs polarise and establish distinct up and downstream signalling regions, which determines the direction in which to extend. The alignment of ECs is believed to be crucial in the correct formation and function of the endothelium. Typically ECs are tens of μm wide and long and about five μm in depth at the highest point (figure 1.1).

The endothelium is a monolayer of ECs that line the entire vasculature system. In the endothelium ECs are joined to each other via cell-cell junctions that construe mechanical properties on the endothelium, and - more importantly - are selectively permeable to materials (for example ions) and cells (for example monocytes) crucial to biological function. It has also been shown that toxic substances (such as nicotine) can open these junctions to allow larger molecules to pass through the wall (Hawkins *et al.*, 2004).

Nicotine is an example of a factor that can increase permeability through the endothe-

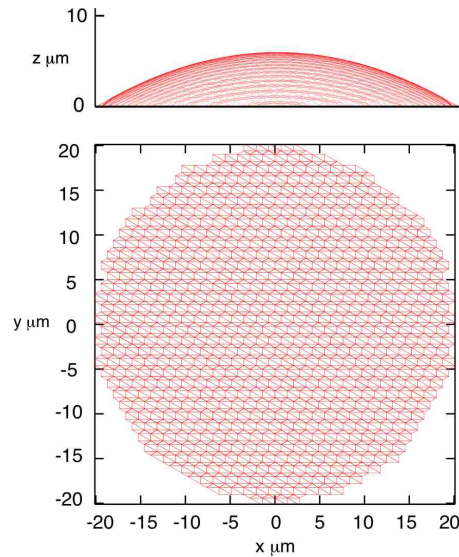


Figure 1.1: A computer representation of an EC. Typical ECs are $40 \mu\text{m}$ in length and width and about $5 \mu\text{m}$ in height.

lium. For example, trans-endothelial flux of low-density lipoproteins (LDLs) which is followed by their retention and modification (lipolysis, proteolysis and aggregation, Sima *et al.* (2009)). The passive diffusive flux of LDLs across the endothelium is believed to be the initial stage in the pathogenesis of the disease atherosclerosis (Berliner *et al.*, 1995). The build up of modified LDLs leads to an inflammatory response from the ECs including recruitment of leukocytes, which can ultimately lead to aggregation of foam cells (macrophages rich with a modified form of low density lipoprotein) beneath the endothelium (Lusis, 2000).

Continued deposition beneath the endothelium, combined with the inflammatory response, leads to formation of plaques associated with atherosclerosis. The plaque consists of a fibrous cap to the lesion below, containing leukocytes, lipid, and debris (Ross, 1999). The cap itself is made up of extra-cellular matrix secreted by smooth muscle cells which are recruited to the lesion by cytokines and growth factors. Degradation of the cap by proteolysis can lead to thrombosis (rupture of the lesion into the blood stream) Lusis (2000).

Such lesions can partially or totally occlude the blood flow. Rupture of the lesion into an artery can resulting in serious clinical complications (figure 1.2).

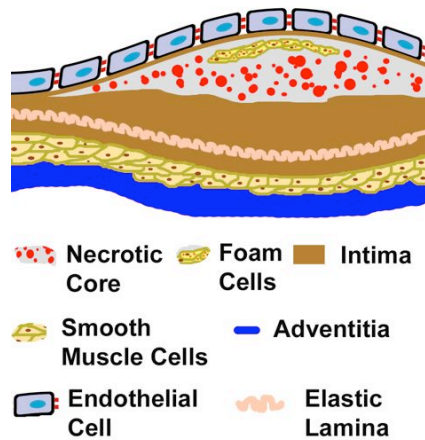


Figure 1.2: Formation of atherosclerotic plaques in response to signals from ECs, macrophages accumulate in the vessel wall and take up a modified form of the cholesterol-transporting low density lipo-proteins (LDLs), leading to the formation of ‘foam cells’. Once these foam cells die they deposit their lipid-rich contents within the vessel wall. Heart disease and stroke can occur if a lesion ruptures into the artery.

Shear stress on the endothelium due to fluid flow has been shown to be athero-protective (Davies *et al.*, 1997). Regions of uni-directional laminar flow appear less prone to atherosclerosis. It is believed that altered gene expression in regions of reduced shear-stress up regulate adhesion to the endothelium by monocytes and T cells (Ross, 1999), leading to aggravation of the inflammatory response outlined above. As a consequence the location of atherosclerotic plaques are correlated with regions of complex blood flow (for example regions of flow reversal due to arterial branching, Davies (2008)). In these regions the ECs take on a rounded morphology, in contrast with an ellipsoidal shape in regions of smooth flow (Weinbaum *et al.*, 1985). Furthermore permeability through the endothelium is increased in turbulent flow regions (Ross, 1999). Hence alignment and elongation of ECs in response to fluid flow may have important physiological consequences for reducing permeability through the endothelium.

1.1 Endothelial Cell Polarisation and Alignment

The process of EC polarisation and alignment can be thought of as being composed of six modules (figure 1.3). The flow over the cell exerts a force, which the cell interprets by transforming the mechanical force into a biochemical one. This mechano-

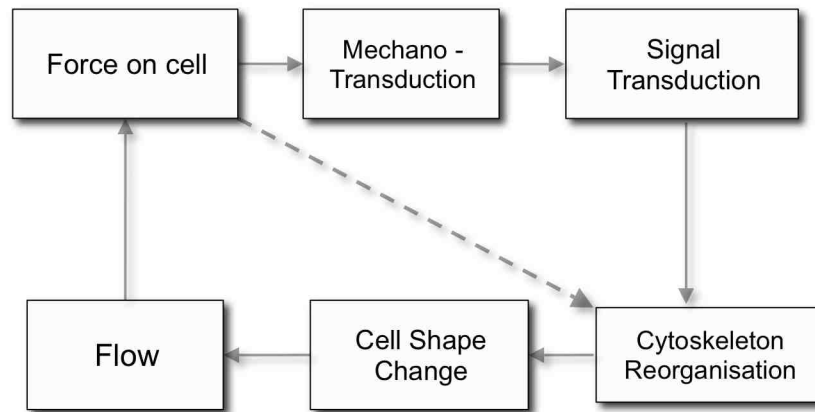


Figure 1.3: Overview of the process of EC polarisation in response to fluid flow. The fluid exerts a force on the cell. This mechanical signal is transduced into a biochemical one, which initiates a signalling network. This network reorganises the cytoskeleton, leading to cell shape change. In principle the force on the cell could alter the cytoskeleton and cell shape directly. A change in cell shape necessarily alters the fluid flow.

transduction initiates a signalling network that mediates the cellular response, most noticeably a change of cell shape via cytoskeleton reorganisation. In principle the cytoskeleton could be affected by the force on the cell directly, without signal transduction.

In this project each of these components is modelled. The force on the cell due to fluid flow is linked to a model of mechano-transduction, the output of which is coupled to a model of Rho GTPase activation and interaction. The Rho GTPases are some of the most studied components of the signalling network and mediate cytoskeleton organisation. Modelling of cytoskeleton reorganisation is explored (chapter 2 and 3), however these models are not coupled to the others. The primary reason for this is the practical and theoretical challenge of linking models of different time and length scales.

1.1.1 Spatial Heterogeneity

The components in figure 1.3 that interact and lead to EC elongation share characteristics with corresponding processes that govern the migration of cells. The most marked similarity is cytoskeleton reorganisation and its corresponding mediation by Rho GTPases. Cells migrating on surfaces move by establishing polarity and forming distinct

signalling regions in the front and back of the cell. The front signalling pathway orchestrates cell protrusion, so the cell grows into the migration direction. The rear pathway mediates cell contraction. The case of EC elongation is similar: an area of local signalling is established in the downstream region of the cell. It is an open question how this local signalling is activated and maintained, this work aims to address this point. It will transpire that comparison of similarities and differences in EC elongation and cell migration signalling leads to some interesting conclusions.

To generate local downstream signalling there must necessarily be a spatial heterogeneity in some of the prior components in figure 1.3. In particular there must be heterogeneity in conversion of a mechanical signal into a biochemical one. If a mechanotransducer is to be activated heterogeneously the component must be located non-uniformly or become activated non-uniformly. Here it will be argued that the second case is likely and is a result of spatial asymmetry of force on the cell in the up and downstream regions.

1.2 Project Goals

This project is an attempt to elucidate each of the components in figure 1.3 and how they interact and lead to the response of the cell. There are reasonable, and often multiple, hypotheses for each of these modules. Coupling models of these components (where feasible) in a biologically meaningful manner provides a method of testing hypotheses about the process as a whole and the individual components. The main questions that this project aims to address are:

- Which cell component interprets physical force?
- How does this component initiate signalling?
- How is polarity established and maintained?
- How is cytoskeleton reorganisation mediated?
- How is the signalling network shut off?

With varying confidence and, where possible, supported by experimental evidence, modelling will provide evidence indicating possible answers to these questions.

1.3 Thesis Structure

The following chapters deal with each component of the process (figure 1.3) starting at the bottom right corner and proceeding sequentially clockwise. Cytoskeleton reorganisation is the obvious starting point because it is this component of the cell that confers structure, hence if the cell is to elongate the cytoskeleton must be reorganised. The results of each chapter (to differing extents) motivate the research of the following chapter.

The other reason for reporting the chapters in this order is it allows the relevant biology to be introduced at the beginning of each chapter that it pertains too, it is anticipated that this makes the chapters more readable and the modelling that follows more relevant. However this does mean that the introduction to the biological concepts and terms is spread across the report, for this reason an index has been constructed for ease of reference.

An electronic version of this report is available on the attached CD along with source code.

The next chapter is an introduction to previous modelling in this area, which has generally focused on cytoskeleton reorganisation. This leads to the author's own extension to one such model.

2 Prior Cytoskeleton Modelling

This chapter introduces the cytoskeleton and reviews previous modelling of the actin cytoskeleton. Firstly an introduction into the biology of the eukaryote cytoskeleton is given. This is followed by an introduction to models of the cytoskeleton in the context of the EC response to fluid flow.

A previous model by the author is discussed. This is followed by an introduction to models of actin alignment, including integro-differential model of spontaneous filament alignment.

The novel contribution of the author in this chapter is this extension to an existing integro-differential model of filament alignment, section 2.4. It is shown analytically that this modification, in the context of the model, can not mediate alignment of filaments.

All the models discussed (in this chapter) deal with modelling the mechanical structure of the cell, whether that be through treating the cell as a continuum or modelling the dynamics of components of the cytoskeleton.

2.1 Cytoskeleton Biology

The cytoskeleton plays an important role in the process of endothelial elongation because it is the component of the cell that defines its structure and form. A good, though of course not perfect, analogy is that of a tent; it is the poles of a tent that define its shape rather than the outer canvas. The cellular ‘canvas’ is the plasma membrane, essentially a two dimensional fluid which is held in place by the cell cytoskeleton and nucleus (the ‘poles’).

The cytoskeleton is complex and dynamic, composed of three main components; microtubules, intermediate filaments and actin filaments. It is regulated by many different signals, including Rho GTPases (which will be explored in more detail in chapter 6), which play a crucial role in EC polarisation.

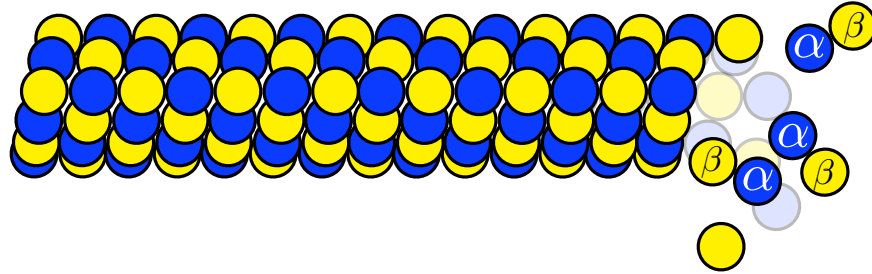


Figure 2.1: Microtubules form by addition of α and β tubulin dimers. Protofilaments (straight chains left to right) attach laterally to form a hollow cylinder.

2.1.1 Microtubules

Microtubules are polymers formed by globular protein sub-units, α - and β -tubulin, and play a crucial role in many cellular processes, notably cell division, cell motility and organelle localisation (Alberts *et al.*, 2008).

Microtubules form initially by γ -tubulin - nucleated polymerisation of $\alpha\beta$ -tubulin heterodimers, although the exact mechanism is unclear. The polymer grows through addition of $\alpha\beta$ -tubulin dimers, and hence is orientated, with a so called plus end structurally distinct from the opposite, minus, end. Nascent tubulin filaments make lateral connections to form a mature microtubule, which has the structure of a hollow cylinder (figure 2.1). The nascent filaments form in such a manner that lateral helices of $\alpha\beta$ -tubulin dimers can be traced around the microtubule, hence polymerisation and de-polymerisation of the microtubule filament occurs by an ‘un-peeling’ and ‘splaying’ of the cylinder structure (Wade & Hyman, 1997).

Generally nucleation occurs at a microtubule organising centre (MTOC) due to targeting of γ -tubulin to these centres. The best described example of a MTOC is the centrosome, from which most cytoplasmic microtubules grow in eukaryotic cells (Üders & Stearns, 2007). *In vitro* microtubules polymerise and depolymerise from either end, however *in vivo* the minus end is generally anchored (and capped) at the MTOC, (Wade & Hyman, 1997).

2.1.2 Intermediate Filaments

Of the three main cytoskeletal elements, intermediate filaments are the broadest in terms of composition and function. However, differing classes of intermediate filaments share a common secondary structure; the central component of which is an α -helical rod domain, parts of which are highly conserved between filament types (Chang & Goldman, 2004).

Intermediate filaments have been suggested to act as a mechanical stress absorbers and even as mechano-transducers (Herrmann *et al.*, 2007). They also play an important role in linking together the other components of the cytoskeleton, both structurally and via crosstalk mechanisms. Interestingly, both intermediate filaments and microtubules are thought to be a downstream target for the Rho GTPases Rho, Rac and Cdc42 as well as tyrosine kinases (Chang & Goldman, 2004).

2.1.3 Actin Filaments

Actin is ubiquitously expressed in eukaryotic cells and plays a role in a wide variety of cellular functions including, motility, division and secretion. Actin filaments can also form cell protrusions (filopodia and lamellipodia, section 3.1) as well as being crucial (along with the myosin II complex) in cellular contraction.

Actin filament structure and formation are introduced in more detail in chapter 3. Briefly, actin filaments are formed from polymerisation of G-actin (globular actin) subunits. Like microtubules they also form a plus (or barbed) or minus (pointed) end.

Individual actin filaments can be structurally organised at a higher level by actin binding proteins, thus conferring distinct properties to the actin filaments. Actin binding proteins have many biochemical activities, including: capping and severing; branching bundling or crosslinking of actin filaments; anchoring filaments to the membrane or linking filaments to other cytoskeleton elements. Section 3.1 describes a model of a particular actin network.

Bundling of actin filaments is the mechanism for formation of stress fibres (the component of the cytoskeleton that governs contraction.) Binding of α -actinin organises actin filaments (typically tens of individual filaments) into parallel bundles. Myosin II is a motor protein that hydrolyses ATP to generate force and walk along actin filaments. Stimulation of myosin activity leads to contraction of stress fibres by binding

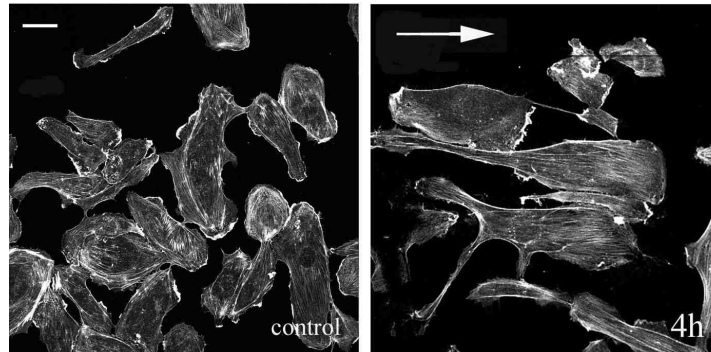


Figure 2.2: Actin filaments in endothelial cells before (control) and after exposure to shear stress for 4 hours (4 h), (Wojciak-Stothard & Ridley, 2003)

to separate filaments and forcing them to slide over each other (Clark *et al.*, 2007). Crosslinking proteins such as filamin, spectrin or transgelin bind on to two separate filaments, but with distinct binding regions so that the filaments are orientated at non-parallel (often perpendicular) angles, (Winder & Ayscough, 2005). The membrane anchors, vinculin and talin, are important because they bind to integrins (transmembrane heterodimers which bind to the extracellular matrix, ECM) and hence link the cell's actin cytoskeleton to the external surroundings.

In this project the modelling is focused exclusively on actin's role in EC alignment. This is chosen for two reasons. Firstly in response to fluid flow the actin stress fibres are observed to align in the direction of EC polarisation (figure 2.2), and secondly they confer more structure to the cell than the other elements. That this is the case was confirmed by Wang (1998), in an illuminating series of experiments. By applying magnetic twisting cytometry¹ Wang (1998) showed that if the actin filament network was disrupted (with Cytochalasin D) then permanent deformation was decreased by 50-70% and stiffness was reduced by 50%. Disruption of the intermediated filaments or microtubules (by Acrylamide and Nocodazole respectively) had little effect on stiffness and permanent deformation.

¹Ferromagnetic beads are added to the cell surface and magnetised in one direction by a strong magnetic field, then a weaker field is applied perpendicular to the original one resulting in a twisting force on the cell from which the angular strain can be deduced.

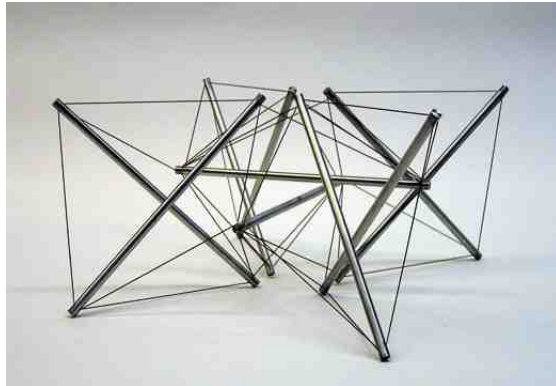


Figure 2.3: Tension-Integrity Sculpture by Kenneth Snelson Snelson (2008)

2.1.4 The Mechanics of the Cytoskeleton

Tension-integrity (tensegrity) is a term first coined by Buckminster Fuller (Fuller, 1961), and is an idea visualised by the sculptor Kenneth Snelson (figure 2.3). It is the idea that structures can be in a stable equilibrium through a balance of tension in some elements and compression in others. One example of a structure that can be built using this principle is shown in figure 2.3. The choice of this particular sculpture is deliberate: it does resemble a simple model of the cell cytoskeleton (although, unlike cells, this structure is not robust to removal of components)

Another example of a tensegrity structure is a tent, which recall was the analogy of cell structure in section 2.1. However the analogy falls down because the structural element of a tent under tension is the canvas, which represents the cell membrane in the analogy: although the membrane is under tension, it is not this tension that balances out the compression in the cellular structure. In the tension-integrity model of the cell the tensile elements are the actin filaments and the compressible elements are the microtubules (Ingber, 2006). Hence in principle to wholly understand cell structure the components of the cell cytoskeleton need to be modelled as separate entities. In particular this is necessary if the tensegrity model is pursued; struts and cables need to be identified.

The tensegrity model has been studied in more depth (Stamenovic *et al.*, 1996; Ingber, 2006; Wang *et al.*, 1993). For example, Stamenovic *et al.* (1996) applied a tensegrity model to a discrete system of struts (microtubules) and cables (actin filaments). They demonstrated that stiffness of the ‘cell’ increased with pre-stress (acto-myosin

generated tension). If a cell is to be considered a tensegrity structure then it has a huge number of constitutive elements, more than are computationally or analytically accessible. Furthermore these elements are dynamically evolving.

Here a different modelling approach is sought so that it is possible to treat the cell structure as a dynamic entity. For simplicity, focus is maintained on either modelling the cytoskeleton as a viscous-elastic medium or only considering actin modelling (in light of the twisting cytometry experiments by Wang (1998)).

Accordingly in the following section two models treating the cell as a visco-elastic medium are discussed. However, it will be noted that ECs are apparently too stiff to be deformed directly by fluid flow (Civelekoglu-Scholey *et al.*, 2005). Hence, mediated re-organisation of the cytoskeleton is a necessary component of the EC response to fluid flow. One such re-organisation is alignment of actin filaments in the flow direction. A discussion of modelling this process (using integro-differential equations) forms the remainder of this chapter.

There are however other notable approaches to modelling cellular structure and dynamics. Some of these will be discussed in chapter 3 in the context of lamellipodia formation.

Dembo & Harlow (1985) modelled the cytoplasm as a reactive interpenetrating flow field (meaning a mix of fluids that have very different velocity fields), with two phases corresponding to the cytoskeleton and an aqueous mixture. Dembo (1986) applied this model to modelling the mechanics of motility and Herant *et al.* (2003) apply this formalism to neutrophil mechanics. Sandersius & Newman (2008) model cell rheology using a ‘sub-cellular element model’ which captures single cell visco-elastic properties in response to strain over time-scales of several seconds. Keren *et al.* (2008) generate keratocyte morphology by modelling the biophysical and biochemical interplay between actin dynamics and membrane tension. Marè *et al.* (2006) also model keratocyte morphology (and cell motility) by using a cellular Potts model (the methodology of cellular Potts, CPM, modelling will be introduced briefly in chapter 8).

2.2 The Cytoskeleton as a Continuum

2.2.1 Fluid Mechanics Approach

This Ph.D. project grew out of the thesis component of the CoMPLEX² MRes course (Allen, 2005). Without wishing to repeat that work here, it is worthwhile recalling it briefly as it provided a first approach to the modelling of the EC response to fluid flow.

In Allen (2005) the problem was reduced to two dimensions. However it will be argued later that meaningful models of the process must necessarily incorporate three dimensions in some manner.

The cell was modelled as a two-dimensional visco-elastic medium, with the initial shape of an ellipse. The blood flow in a large artery can be roughly approximated (treating the flow as quasi-steady Hazel & Pedley (2000)) as a Poiseuille flow, that is to say that the velocity profile of the flow assumes a parabolic shape (figure 2.4, for a justification of this see section 4.1). The shear stress on the cell results from the drag the cell surface exerts on the fluid. The 2D-ellipse was taken to be a slice of the cell

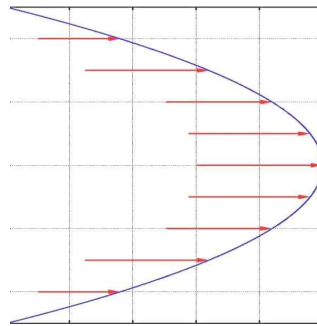


Figure 2.4: Poiseuille Flow. Here the velocity of the flow is proportional to the square of the distance from nearest vessel wall.

1 μm above the vessel wall (figure 2.5), because if the ellipse was taken as the basal surface of the cell then the flow around it would be zero (flow on the vessel wall is taken to be zero). The flow was modelled using the Stokes equation

$$\nabla \cdot \mathbf{y} = 0 \quad (2.1)$$

²Centre for Mathematics and Physics in the Life Sciences and Experimental Biology, UCL

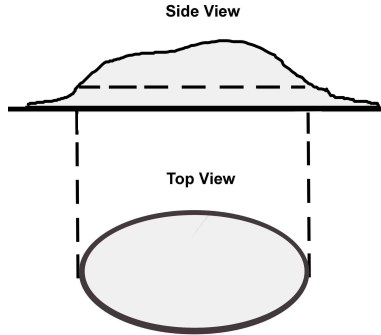


Figure 2.5: Cartoon illustrating how the 2D cell relates to the 3D cell.

where

$$y_{ij} = -P\delta_{ij} + \mu \left(\frac{\partial u_i}{\partial x_j} + \frac{\partial u_j}{\partial x_i} \right) \quad (2.2)$$

is the stress tensor of the fluid. P is the pressure and u_i is one component of the 2-D flow. In this problem it is desirable to reformulate this using the boundary integral representation (Pozrikidis, 1992). Section 4.3 deals with the boundary integral representation (BIR) in more detail. Here the BIR representation for a 2D flow is

$$u_j(\mathbf{x}_0) = u^\infty(\mathbf{x}_0) - \frac{1}{4\pi} \int_c \Delta f_i G_{ij}(\mathbf{x}, \mathbf{x}_0) dl(\mathbf{x}) \quad (2.3)$$

where: $u^\infty(\mathbf{x}_0)$ is the unperturbed flow, the integral is around the boundary of the cell, Δf_i is the discontinuity in the surface force at the interface between the fluid and the cell and $G_{ij}(\mathbf{x}, \mathbf{x}_0)$ is the free-space Green's function. Solution of this equation is not entirely straight forward (numerically or otherwise); the details are presented in Allen (2005).

2.2.2 Results and Criticism

The results of this model were qualitatively similar to experimental results for ECs responding to fluid flow (figure 2.6). The model cell did elongate and align with the flow (figure 2.6), and in a comparable time period (about 20 minutes, compared to about an hour for an EC *in vitro*, although a change in morphology would probably be noted before this time).

The project presented here is an attempt to model EC alignment in more detail, both

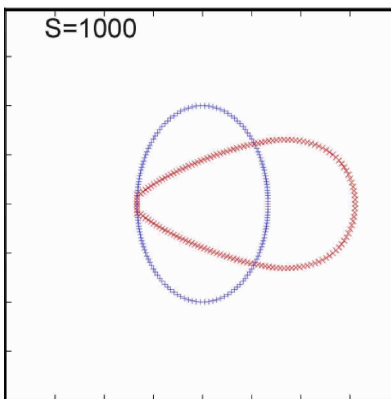


Figure 2.6: Continuum model of the cell. The flow is left to right and the initial cell shape is the blue ellipse. The final shape, after $S=1000$ time steps (corresponding to about 20 minutes) is the red tear drop shape aligned with the flow.

quantitatively and qualitatively. Such a model should improve biological understanding of the process and vice versa. To this end it is important to identify the limitations of the continuum model, equation 2.3.

The model has four major failings:

- To derive the BIR it is necessary to assume the viscosity of the cell is equal to that of the fluid flowing around the cell. In reality the cell is stiffer than accounted for in the model.
- The actin cytoskeleton is thought to be too stiff to be deformed by physiological flows (Civelekoglu-Scholey *et al.*, 2005).
- The local internal structure of the cell is ignored: the cytoskeleton is implicitly assumed to be homogeneous and isotropic.
- The cell does have a biochemical response to shear stress, it is not a passive object in this process, (Tzima *et al.*, 2001, 2002).

The assumptions that give rise to these failings, although questionable, are often made in modelling aspects of the EC response to fluid flow and indeed in other contexts. The viscosity assumption has previously (and perhaps more validly) been made in the context of red blood cells (Zhou & Pozrikidis, 1995), and necessarily assumes the cell to be a homogeneous material. This assumption is also made by Sherratt & Lewis (1993)

(discussed in the next section) and ignoring cell regulation of structure is commonly made in tensegrity models (section 2.1.4).

It is clear from these points that it may prove necessary to model at three or more time and length scales in this project, in particular the scales of the biochemical interactions, the cytoskeletal re-organisation and the cell itself. Furthermore it may be the case that there are synergistic effects of being in contact with other cells. This ‘contact’ is more significant than just the cells touching. In between ECs selectively permeable junctions (tight junctions) are formed from transmembrane proteins such as claudin and occludin that only allow passage of small molecules and ions. Adherens junctions and desmosomes also contribute to the mechanical integrity of the cell-cell junctions because they are anchored to actin filaments and intermediate filaments respectively and attach cell to cell via cadherin proteins. In chapter 5 a hypothesis of mechano-transduction (of the fluid flow signal) at cell-cell adhesions is discussed.

2.2.3 Stress-Induced Alignment

The unifying feature of the models discussed in this chapter (with the exception of the author’s extension to one of these models, section 2.4) is that they are mechanical in nature; the cytoskeleton is simplified to a passive (i.e. not chemically active) structural component of the cell.

A good introduction to this manner of describing the cytoskeleton is given by Sherratt & Lewis (1993). Their model describes a possible mechanism for how alignment of actin filaments could be induced by stress on the ‘cytogel’ (the continuum of actin, intermediate filaments, microtubules and cytoplasm in the cell). They assume that alignment occurs as a response to the ratio of the principal components of stress. This may well be the case, however how the cell interprets the direction of stress and mediates the alignment is unclear. A mechanism for flow sensing will be argued for in chapters 4 and 5, it will transpire that responding to shear stress is not the simplest, nor (in the author’s view) the best, hypothesis for flow sensing.

Nevertheless the starting point for their investigation is the 2-D stress tensor:

$$\begin{pmatrix} y_{xx} & y_{xy} \\ y_{yx} & y_{yy} \end{pmatrix} \quad (2.4)$$

where y_{xx} and y_{yy} are tensions in the x and y directions respectively, the remaining

two components are shear forces. The principal components of this stress tensor are the orthogonal eigenvectors of this (symmetric) matrix, so for example if these eigenvectors are taken as the co-ordinate system³ then the stress tensor is diagonalised and represents only tensions and not shear forces. So the ratio, ρ , of the eigenvalues of the principal components (y_1 and y_2) characterises the stress field. If $\rho = 0$ or ∞ then the stress field is 1-D, i.e. unidirectional, or if $\rho = 1$ then the stress is the same in all directions ($\rho = 1$ implies that the eigenvalues are equal, which in turn implies a 2-D eigenspace spanned by any two vectors: i.e. any direction is an eigenvector). Note that ρ is a function of position in the cell.

Sherratt & Lewis (1993) then proceed by denoting the density of actin filaments by $F(\phi; \rho)$. Hence $F(\phi; \rho)\delta\phi$ is the average proportion of filaments in the range $(\phi, \phi + \delta\phi)$, with symmetries: $F(\phi; \rho) = F(-\phi; \rho) = F(\phi + \pi; \rho)$. The authors demand that this function satisfies the following conditions

- $F(\phi; \rho) \rightarrow \delta(\pi/2 - \phi)$ as $\rho \rightarrow 0$ and $F(\phi; \rho) \rightarrow \delta(\phi)$ as $\rho \rightarrow \infty$
- $\int_0^{\pi/2} F(\phi; \rho) d\phi = 1$
- $F(\phi; 1)$ is a constant
- $F(\phi; \rho) = F(\pi/2 - \phi; 1/\rho)$

where $\delta(\phi)$ is the dirac delta function defined by $\delta(0) = 1$ and 0 otherwise.

These restrictions lead to a functional expression for the filament density at a given angle, they also restrict the emergent properties of this formulation - these criteria demand that stress causes filament alignment. In particular the first point ensures that for a unidirectional shear field all the filaments align in that direction. Nonetheless, a functional expression is given that is claimed to satisfy (at least to a good approximation) these conditions. Each actin filament is assumed to exert a stress (through acto-myosin contraction) and Sherratt & Lewis (1993) take the stress exerted by the network of actin filaments as a whole to be given by the density of actin filaments along the principal axes of the stress tensor:

$$\begin{aligned} G_1(\mathbf{r}) &= G_0(\mathbf{r}) \int_0^{\pi/2} F(\phi; \rho) \cos(\phi) d\phi \\ G_2(\mathbf{r}) &= G_0(\mathbf{r}) \int_0^{\pi/2} F(\phi; \rho) \sin(\phi) d\phi \end{aligned} \quad (2.5)$$

³Due to tensor properties it does not matter what system you choose.

where $G_0(\mathbf{r})$ is the total filament concentration at position \mathbf{r} .

One expression that satisfies the bulleted points is

$$G_1(\mathbf{r}) = \frac{(\pi/2)y_1^P G_0(\mathbf{r})}{y_1^P + (\pi/2 - 1)y_2^P}$$

$$G_2(\mathbf{r}) = \frac{(\pi/2)y_2^P G_0(\mathbf{r})}{y_2^P + (\pi/2 - 1)y_1^P}$$

where P is some parameter ($P > 0$) which represents the sensitivity of the response to the anisotropy of the stress field. It is clear that these expressions result in alignment of the filaments in the direction of the largest component of stress. However this alignment could be due to ‘auto-alignment’ from stress in the actin filaments themselves or due to an externally applied stress. Furthermore, critical values of P determine whether a perturbation of an aligned network of filaments realigns with the external stress field (i.e. whether internal stresses due to myosin induced contraction or external stresses dominate).

In the context of this project this model does not address the nature of the biological response - it is hard to see how this model could be applied to test some of the questions raised in section 1.2. This model describes stress fibre alignment but does not illuminate how it occurs. In principal the alignment could arise due to filament turning to a given direction or by directed polymerisation leading to anisotropy in the alignment direction. Clearly this prescriptive formulation is not a good tool for addressing these points. A more promising modelling approach is introduced in the next section.

2.3 Integro-Differential Modelling

There are a whole group of models that take a different approach to describing the dynamics of the angular distribution of filaments $f(\theta, t)$, (Geigent *et al.*, 1998; Civelekoglu *et al.*, 1998; Suci *et al.*, 1997; Civelekoglu & Edelstein-Keshet, 1994; Mogilner & Edelstein-Keshet, 1996). In all these models integro-differential equations describe how the filaments rearrange dynamically. The crucial idea is that filaments interact and turn due the influence of an actin bundling protein, for example myosin II. However, in these models it is not necessary to specify a binding protein but the characteristics (for example, the angle at which the binding protein binds filaments) of the protein are required.

This is modelled by describing the change in $f(\theta, t)$, due to angular turning, as a balance between filaments that turn to θ and filaments that turn away from θ . To quantify these a weighted integral is formed over the angular space, for example:

$$\int_{-\pi}^{\pi} K(\theta - \theta') f(\theta', t) d\theta' = (K \otimes f) \quad (2.6)$$

where $K(\theta - \theta')$ is a weighting function, or kernel, that determines how filaments at angles θ and θ' interact (for example maybe if $\theta - \theta'$ is large then the filaments do not interact). $(K \otimes f)$ is shorthand for this expression.

For suitable choices of the kernel all these models have the property of instantaneous alignment from an isotropic state (with a small amount of noise), i.e. the equilibrium point of $f(\theta, t) = \text{const.}$ is an unstable state. Generally these models are spatial only in the angular direction, effectively describing interaction of filament densities at a point dependent on a parameter θ which is the alignment direction of the filament.

The models cited above apply expressions like this in different ways:

- Modelling alignment of filaments with cyclic stretch: by applying this model at two points of separation x , with the interaction of two filaments dependent on their separation x (varying cyclically) and the angle between them (Civelekoglu *et al.*, 1998).
- Modelling actin filaments as being either in a bound or free state: this requires a pair of coupled integro-differential equations such as $B.(K \otimes f)$ representing the rate at which free filaments at an arbitrary angle bind to bound filaments at θ (Civelekoglu & Edelstein-Keshet, 1994)
- Modelling the filaments as rotating due to being anchored by a transmembrane protein on the apical side that is moving due to the fluid flow (Suciu *et al.*, 1997)

The last of these examples is interesting because it agrees with a paper proposing a model of actin filament alignment being due to force on the glycocalyx (a thin layer of proteins attached to the cell surface) which attaches to an ‘actin cortical web’ just below the cell membrane. This idea is explored in more detail in section 5.1.2 . It is proposed that this induces a net torque acting on the dense peripheral actin band (DPAB), and that once this exceeds a threshold the adherens junctions between cells rupture, which

induces the signalling network and actin filament formation and alignment (Thi *et al.*, 2004).

The model that I have studied in more depth is proposed by Geigent *et al.* (1998). In this model only one population of filaments is considered. Where this model differs from the previous examples is that it provides a more physically realistic mechanism for turning of filaments. In this case two filaments interacting at angles θ and θ' both turn (with high probability) to an angle θ_n . The probability of a filament at θ turning to this direction as a result of interacting with a filament at θ' is defined by:

$$\omega(\theta - \theta_n, \theta - \theta'). \quad (2.7)$$

The second argument of this function determines the probability of two filaments interacting, and the first argument the probability, if the interaction occurs, of turning to angle θ_n . The rate of interaction between filaments at angles θ and θ' is determined by $\eta(\theta - \theta')$. Since ω is a probability function, and every interaction must result in turning to some angle:

$$\int_{-\pi}^{\pi} \omega(\theta - \theta_n, \theta - \theta') d\theta_n = 1. \quad (2.8)$$

η is normalised by demanding

$$\int_{-\pi}^{\pi} \eta(\theta - \theta_i) d\theta_i = 1. \quad (2.9)$$

This is equivalent to scaling the time units. To quantify the rate of turning of filaments at angle θ_0 to an angle θ_n it is necessary to consider the interactions at all the angles that could result in a filament turning to θ_n

$$W[f](\theta_0, \theta_n) = \int_{-\pi}^{\pi} \eta(\theta_0 - \theta_i) \omega(\theta_0 - \theta_n, \theta_0 - \theta_i) f(\theta_i, t) d\theta_i. \quad (2.10)$$

Geigent *et al.* describe the F-actin network as evolving purely due to turning induced by other filaments. So $f(\theta, t + \Delta t) - f(\theta, t) \approx$ Elements that turn to θ - Elements that turn away, which leads to

$$\frac{\partial f(\theta, t)}{\partial t} = -f(\theta, t) \int_{-\pi}^{\pi} W[f](\theta, \theta_n) d\theta_n + \int_{-\pi}^{\pi} W[f](\theta_0, \theta) f(\theta_0, t) d\theta_0. \quad (2.11)$$

Rewriting this yields

$$\frac{\partial f(\theta, t)}{\partial t} = -f(\theta, t) \int_{-\pi}^{\pi} \eta(\theta - \theta_i) f(\theta_i, t) d\theta_i$$

$$+ \int_{-\pi}^{\pi} \int_{-\pi}^{\pi} \omega(\theta_0 - \theta, \theta_0 - \theta_i) \eta(\theta_0 - \theta_i) f(\theta_0, t) f(\theta_i, t) d\theta_i d\theta_0. \quad (2.12)$$

It is straightforward to show that the total mass of filaments is conserved. It only remains to define η and ω . An example of standard choices for these functions and the corresponding result can be seen in section 2.4.1, where a description of an extension to this model is given. As will be shown, filaments in this model do align instantaneously, primarily because small anisotropies in the angular distribution attract other filaments (as long as the filaments are within the range of interaction, which defines the type of distribution that evolves).

2.4 Extending the Integro-Differential Model

The ‘alignment’ models discussed in the previous section are essentially mechanical in nature, in that they do not really incorporate much -if any- of the biochemistry that orchestrates the cellular reorganisation. Although it may be the case that filament alignment occurs independently of the biochemical network (as in the Sherratt & Lewis (1993) model, equation 2.5) it is likely that the alignment process itself is regulated (Wojciak-Stothard & Ridley, 2003). One possibility is that the cell does this by up-regulating polymerisation, and this provides a small local anisotropy - yet sufficient to initiate spontaneous alignment globally.

2.4.1 Extended Model

The initial novel contribution of this thesis begins with an extension to an existing integro-differential model. To find how filament alignment could be biochemically induced equation 2.12 (Geigent *et al.*, 1998) is extended to include polymerisation (and depolymerisation) of the filaments from a limited supply of actin monomers.

$$\begin{aligned} \frac{\partial f(\theta, t)}{\partial t} &= -\gamma f(\theta, t) + \alpha f(\theta, t) A(t) \\ &+ \int_{-\pi}^{\pi} W[f](\theta_0, \theta) f(\theta_0, t) d\theta_0 \\ &- f(\theta, t) \int_{-\pi}^{\pi} W[f](\theta_0, \theta_n) f(\theta_0, t) d\theta_n \\ \frac{dA}{dt} &= (\gamma - \alpha A(t)) F(t) \end{aligned}$$

$$+ r_0(A + F(t)) \left(1 - \frac{A + F(t)}{K} \right) \quad (2.13)$$

where

$$F(t) = \int_{-\pi}^{\pi} f(\theta, t) d\theta \quad (2.14)$$

is the total amount of actin bound in filaments at any given time. The integral terms are as in equation 2.12 (Geigent *et al.*, 1998) and represent the angular interaction of filaments. Note that both η and ω should be chosen as symmetric so that turning anti-clockwise is not preferred over clockwise or vice versa. The first integral represents the density of actin filaments that turn to θ (hence it is positive) and the second the filament density that turns away from θ . A is the concentration of unbound actin monomers, γ is the rate of depolymerisation of F-actin, α the rate of polymerisation. Hence $\alpha f(\theta, t)A(t)$ is the rate of the increase in filament density at the angle θ (polymerisation is dependent on the concentration of A and f).

The last term of the equation for A is a logistic term which ensures that if $A + F(t) \gg K$ then $dA/dt < 0$ and so the monomer concentration (and in turn the filament concentration) reduces. This is a simple way to model cellular regulation of the total actin level, K represents a cell's internal measure of actin levels - if total actin concentration is low it gets up-regulated to K and if it is high it gets down regulated to K .

Note however that with this term the total amount of actin is not conserved because there is a logistically growing population of actin limited by the 'carrying capacity' K . Biologically this corresponds to a background rate of actin synthesis regulated in some manner to give a typical level of total actin (in either F-actin or G-actin forms) in the cell. The parameter K represents this level.

This system is not entirely straightforward to solve numerically, mainly because it is necessary to discretise the θ variable. The approach taken here is to form a discrete system of $n + 1$ equations each describing the evolution of a variable θ_i , representing a discretised interval of the θ variable

$$f(\theta, t) \longrightarrow \left\{ f_i(t) \mid f_i(t) = f\left(\frac{2\pi i}{n}, t\right); i = 0, 1, \dots, n \right\} \quad (2.15)$$

Applying this discretisation (and the expression for A) results in $n + 1$ coupled ordinary

differential equations:

$$\begin{aligned}
\frac{df_i(t)}{dt} &= -(\gamma - \alpha A)f_i(t) - \frac{4\pi^2}{n^2} \left(f_i(t) \sum_{j=0}^{n-1} \sum_{k=0}^{n-1} \omega \left(\frac{2\pi k}{n}, \frac{2\pi(i-j)}{n} \right) \eta \left(\frac{2\pi(i-j)}{n} \right) f_j(t) \right. \\
&\quad \left. - \sum_{j=0}^{n-1} \sum_{k=0}^{n-1} \omega \left(\frac{2\pi(j-i)}{n}, \frac{2\pi(j-k)}{n} \right) \eta \left(\frac{2\pi(j-k)}{n} \right) f_j(t) f_k(t) \right) \\
\frac{dA(t)}{dt} &= (\gamma - \alpha A)F(t) + r_0(A + F(t)) \left(1 - \frac{1}{K}(A + F(t)) \right)
\end{aligned} \tag{2.16}$$

where now $F(t) = \sum_i f_i(t)$. The temporal co-ordinate is discretised using a Runge-Kutta order 4 (RK4) scheme (a standard numerical method), define

$$\frac{df_i}{dt} = g_i(f_0, \dots, f_i, \dots, f_n, t) \tag{2.17}$$

where the A variable as been rewritten as f_n for compactness. Then the RK4 scheme is

$$f_i^{j+1} = f_i^j + \frac{\delta t}{6} (k_i^0 + 2k_i^1 + 2k_i^2 + k_i^3) + O(\delta t^3) \tag{2.18}$$

where

$$\begin{aligned}
k_i^0 &= g_i \left(f_0^j, \dots, f_i^j, \dots, f_n^j, t^j \right) \\
k_i^1 &= g_i \left(f_0^j + \frac{1}{2}k_0^0, \dots, f_i^j + \frac{1}{2}k_i^0, \dots, f_n^j + \frac{1}{2}k_n^0, t^j \right) \\
k_i^2 &= g_i \left(f_0^j + \frac{1}{2}k_0^1, \dots, f_i^j + \frac{1}{2}k_i^1, \dots, f_n^j + \frac{1}{2}k_n^1, t^j \right) \\
k_i^3 &= g_i \left(f_0^j + k_0^2, \dots, f_i^j + k_i^2, \dots, f_n^j + k_n^2, t^j \right)
\end{aligned}$$

An example of the results from this model, with arbitrary parameters, is shown in figure 2.7. This system was analysed by local stability analysis, which gives analytical results for arbitrary parameters.

2.4.2 Stability Analysis

Consider a small perturbation away from the isotropic equilibrium point,

$$(\bar{f}, \bar{A}) = \left(\frac{K - \gamma}{2\pi}, \frac{\gamma}{\alpha} \right):$$

$$\tilde{f}(\theta, t) = \bar{f} + \hat{f}(\theta, t), \quad \tilde{A}(t) = \bar{A} + \hat{A}(t) \tag{2.19}$$

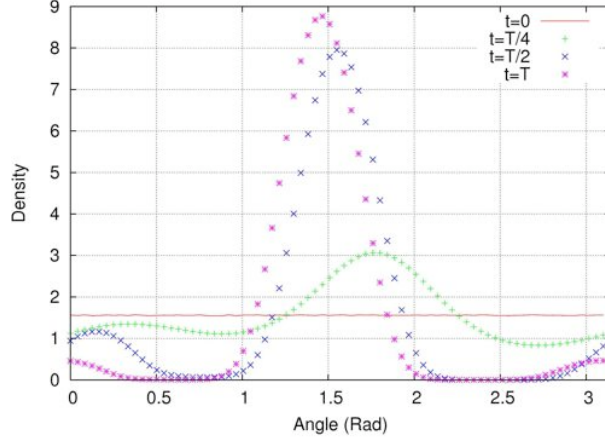


Figure 2.7: Spontaneous alignment of actin filaments, governed by equation (2.13) up to time $T = 3000$ time steps. Here the peak filament density is at $\pi/2$, indicating alignment at this angle. Arbitrary units were used in this simulation $\delta t = 0.1$, $n = 70$, $K = 10$, $r_0 = 0.2$, $\gamma = 0.1$ and $\alpha = 0.1$.

so that \hat{A}^2 and \hat{f}^2 (and higher orders) are negligible and $\tilde{f}(\theta, t)$ and $\tilde{A}(t)$ satisfy the differential equations. The goal here is to linearise the system around the equilibrium. For a non-spatial linear system, perturbations of the form $\xi(t)$ are considered but here due to the periodicity (in θ), the steady state solution for $f(\theta, t)$ is subjected to a spatial perturbation of the form $e^{il\theta}$, (where l is an integer), hence perturbations are sought of the form

$$\hat{f}(\theta, t) = e^{il\theta} \xi_1^l(t), \quad \hat{A}(t) = \xi_2^l(t) \quad (2.20)$$

where ξ_1^l and ξ_2^l are small enough so that on substituting these expressions into equations 2.13 only terms linear in the $\hat{f}(\theta, t)$ and $\hat{A}(t)$ perturbations need to be considered. Firstly consider the equation for $\tilde{f}(\theta, t)$, substituting the expansion around the equilibrium point gives:

$$\begin{aligned} \frac{\partial \tilde{f}(\theta, t)}{\partial t} &= -\gamma \bar{f} - \gamma \hat{f}(\theta, t) + \alpha \bar{f} \hat{A}(t) + \alpha \bar{f} \bar{A}(t) + \alpha \hat{f}(\theta, t) \bar{A}(t) + \alpha \hat{f}(\theta, t) \hat{A}(t) \\ &+ \int_{-\pi}^{\pi} \int_{-\pi}^{\pi} \eta(\theta_0 - \theta_i) \omega(\theta_0 - \theta, \theta_0 - \theta_i) (\bar{f} + \hat{f}(\theta_i, t)) (\bar{f} + \hat{f}(\theta_0, t)) d\theta_i d\theta_0 \\ &- (\bar{f} + \hat{f}(\theta, t)) \int_{-\pi}^{\pi} \eta(\theta - \theta_i) (\bar{f} + \hat{f}(\theta_i, t)) d\theta_i \end{aligned}$$

where \bar{f} and \bar{A} are the steady state solution. Cancelling out the equilibrium terms (at an isotropic steady state $-\gamma \bar{f} + \alpha \bar{f} \bar{A} = 0$, equation 2.13) and expanding the integrals

(neglecting order two terms) gives:

$$\begin{aligned}
\frac{\partial \widehat{f}(\theta, t)}{\partial t} &= -\gamma \widehat{f}(\theta, t) + \alpha \bar{f} \widehat{A}(t) + \alpha \widehat{f}(\theta, t) \bar{A}(t) \\
&+ \bar{f}^2 \int_{-\pi}^{\pi} \int_{-\pi}^{\pi} \eta(\theta_0 - \theta_i) \omega(\theta_0 - \theta, \theta_0 - \theta_i) d\theta_i d\theta_0 \\
&+ \bar{f} \int_{-\pi}^{\pi} \int_{-\pi}^{\pi} \eta(\theta_0 - \theta_i) \omega(\theta_0 - \theta, \theta_0 - \theta_i) \widehat{f}(\theta_0, t) d\theta_i d\theta_0 \\
&+ \bar{f} \int_{-\pi}^{\pi} \int_{-\pi}^{\pi} \eta(\theta_0 - \theta_i) \omega(\theta_0 - \theta, \theta_0 - \theta_i) \widehat{f}(\theta_i, t) d\theta_i d\theta_0 \\
&- \bar{f} \int_{-\pi}^{\pi} \eta(\theta - \theta_i) \widehat{f}(\theta_i, t) d\theta_i \\
&- \bar{f}^2 \int_{-\pi}^{\pi} \eta(\theta - \theta_i) d\theta_i \\
&- \bar{f} \widehat{f}(\theta_i, t) \int_{-\pi}^{\pi} \eta(\theta - \theta_i) d\theta_i
\end{aligned} \tag{2.21}$$

Note that the first and last two integral terms in this expression are equal to 1, using expressions 2.8 and 2.9.⁴

The remaining integrals can be simplified:

$$\begin{aligned}
&\bar{f} \int_{-\pi}^{\pi} \int_{-\pi}^{\pi} \eta(\theta_0 - \theta_i) \omega(\theta_0 - \theta, \theta_0 - \theta_i) \widehat{f}(\theta_0, t) d\theta_i d\theta_0 \\
&= \bar{f} \int_{-\pi}^{\pi} \int_{-\pi}^{\pi} \eta(y) \omega(\theta + y - \theta_i, y) \widehat{f}(\theta_i - y, t) d\theta_i dy \\
&= \bar{f} \int_{-\pi}^{\pi} \int_{-\pi}^{\pi} \eta(y) \omega(\theta - \theta'_i, y) \widehat{f}(\theta'_i, t) d\theta'_i dy
\end{aligned} \tag{2.22}$$

Here the substitutions $\theta_i - \theta_0 = y$ and $\theta'_i = \theta_i - y$ are made. Also it is exploited that η and ω are even functions (the latter in both arguments) and that the integrals are over complete periods. Similarly,

$$\begin{aligned}
&\bar{f} \int_{-\pi}^{\pi} \int_{-\pi}^{\pi} \eta(\theta_0 - \theta_i) \omega(\theta_0 - \theta, \theta_0 - \theta_i) \widehat{f}(\theta_i, t) d\theta_i d\theta_0 \\
&= \bar{f} \int_{-\pi}^{\pi} \int_{-\pi}^{\pi} \eta(y) \omega(\theta - \theta_i + y, y) \widehat{f}(\theta_i, t) d\theta_i dy
\end{aligned} \tag{2.23}$$

⁴Equation 2.9 applies directly to the latter two integrals. To apply both 2.8 and 2.9 to the first double integral term note that because the integrals are over complete periods:

$$\int_{-\pi}^{\pi} \int_{-\pi}^{\pi} \eta(\theta_0 - \theta_i) \omega(\theta_0 - \theta, \theta_0 - \theta_i) d\theta_i d\theta_0 = \int_{-\pi}^{\pi} \int_{-\pi}^{\pi} \eta(y) \omega(\theta_0 - \theta, y) dy d\theta_0$$

now applying expressions 2.8 and 2.9 (and using that ω is symmetric in θ_0) gives that the integrals are equal to one.

Substitution of expressions 2.20 into equation 2.21 (with the integrals simplified as described above) and denoting differentiation with respect to time with a dot, leaves the linearisation as:

$$\dot{\xi}_1^l = \alpha \bar{f} \xi_2^l + \bar{f}(\hat{I} - \hat{\eta} - 1)\xi_1^l \quad (2.24)$$

where:

$$\begin{aligned} \hat{I} &= \int_{-\pi}^{\pi} \int_{-\pi}^{\pi} \eta(y)((\omega(\theta, y) + \omega(\theta + y, y))e^{-il\theta}) d\theta dy \\ \hat{\eta} &= \int_{-\pi}^{\pi} \eta(\theta)e^{-il\theta} d\theta \end{aligned} \quad (2.25)$$

The expression governing A , equation 2.13, linearises more simply as:

$$\dot{\xi}_2^l = (-2\pi\gamma\bar{f} + r_0)\xi_2^l \quad (2.26)$$

So the linearisation of the system around the equilibrium points leads to the system:

$$\begin{pmatrix} \dot{\xi}_1^l \\ \dot{\xi}_2^l \end{pmatrix} = \begin{pmatrix} \bar{f}(\hat{I} - \hat{\eta} - 1) & \gamma\bar{f} \\ 0 & -2\pi\bar{f} - r_0 \end{pmatrix} \begin{pmatrix} \xi_1^l \\ \xi_2^l \end{pmatrix} \quad (2.27)$$

Denote the 2×2 matrix above as J . Stability of the system is determined from the eigenvalues of J . The Routh-Hurwitz criteria gives that if $\text{Det } J > 0$ and $\text{Tr } J < 0$ then the state is stable (figure 2.8) (Britton, 2003).

Stability of this system has to be checked for all modes, l . Hence each mode has a corresponding eigenvalue and for stability all these eigenvalues have to have negative real part.

If alignment of filaments is to occur spontaneously this isotropic equilibrium needs to be in an unstable state. It may be imagined that the system is initially in a stable state and then the system becomes unstable in response to some stimulus leading to filament alignment. To investigate this it is worth examining the properties of J in order to examine how such a switch could occur. To do this analytically it is necessary to choose the functions η and ω , the choice is restricted to simple functions so the integrals \hat{I} and $\hat{\eta}$ can be solved analytically. However the analysis in Geigent *et al.* (1998) indicates that this can be done without loss of generality so long as the choices are of a certain form. In this case this is taken to be of a form that describes attractive interaction between filaments leading to parallel alignment. Clearly a choice that leads to per-

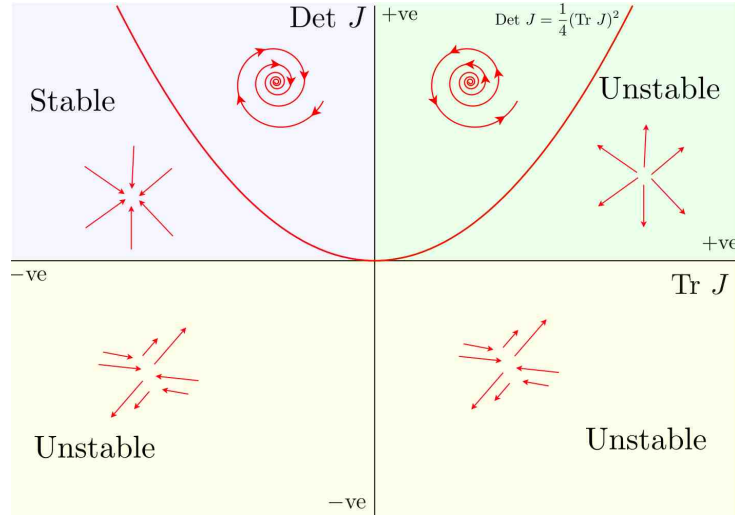


Figure 2.8: Standard linear stability analysis (Britton, 2003). For a linear (or linearised) system the stability of the equilibrium points is defined by the signs of $\text{Det } J$ and $\text{Tr } J$. If $\text{Det } J < 0$ the system is unstable, if $\text{Det } J > 0$ then stability depends on $\text{Tr } J < 0$. The type of stability (or indeed instability) depends on whether $4\text{Det } J > (\text{Tr } J)^2$

pendicular alignment makes a significant difference, however as long as the qualitative form of the function remains the same conclusions should hold for different expressions, (Geigent *et al.*, 1998). For example the uniform function taken here (figure 2.9) leads to the same conclusions as a Gaussian distribution.

Here $S(\theta)$ (figure 2.9) is used to define η and ω , parameterised by ρ and σ (as in figure 2.9) respectively: $\eta = S(\theta)$ with $\rho = \pi/4$ and $\omega(\theta, \theta') = S(\theta - \theta'/2)$ with $\sigma = 0.25$.

With these choices, \hat{I} and $\hat{\eta}$ are easily integrated and the determinant and trace of the matrix can be determined as:

$$\begin{aligned} \text{Det } J &= \frac{K - \gamma/\alpha}{2\pi} \left(\frac{4 \sin(l\sigma) \sin(l\rho/2)}{l^2 \sigma \rho} - \frac{\sin(l\rho)}{l\rho} - 1 \right) (-K\alpha + \gamma - r_0) \\ \text{Tr } J &= \frac{K - \gamma/\alpha}{2\pi} \left(\frac{4 \sin(l\sigma) \sin(l\rho/2)}{l^2 \sigma \rho} - \frac{\sin(l\rho)}{l\rho} - 1 \right) - K\alpha + \gamma - r_0 \end{aligned} \quad (2.28)$$

The trigonometric term in the main parenthesis can be bound regardless of the choice of the parameters, for (treating l as a variable) it is of the form:

$$T(x) = \frac{2 \sin(ax) \sin(bx)}{ax \cdot bx} - \frac{\sin(cx)}{cx} - 1. \quad (2.29)$$

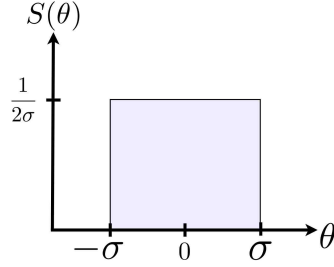


Figure 2.9: Uniform block function $S(\theta)$ parameterised by σ , used to define $\omega(\theta, \theta') = S(\theta - \theta'/2)$ with $\sigma = 0.25$, so that filaments aligned at an angle θ have uniform probability of turning into the range $(\theta'/2) \pm 0.25$. $S(\theta)$, now parameterised by ρ , is also used as the choice for $\eta(\theta)$ with $\rho = \pi/4$, so the rate of interaction between filaments is constant as long as they are aligned within $\pi/4$.

Clearly $-1 \leq \sin(ax)/ax \leq 1$, but actually the lower bound can be tightened. The stationary points satisfy $ax = \tan(ax)$, which solves (numerically) to give $ax \approx 4.49$ as the first non trivial positive solution. This was found by solving $y + \pi = \tan(y)$ using the expansion for $\tan(y)$:

$$\tan(y) = y + \frac{y^3}{3} + \frac{2y^5}{15} + \frac{17y^7}{315} + \dots \quad (2.30)$$

this was necessary because this expansion is only valid for $|y| \leq \pi/2$, however note that $y + \pi = \tan(y) = \tan(y + \pi)$. So a solution for $ax = \tan(ax)$ is found by taking $ax = y + \pi$. This solution corresponds to the first minimum for $x > 0$, and (with its reflection in $x = 0$) this is a global minimum as the value of $\sin(ax)/ax$ at stationary points tend to zero as $x \rightarrow \infty$ or $x \rightarrow -\infty$. Hence $-0.22 \leq \sin(ax)/ax \leq 1$ and the bounds on equation 2.29 becomes

$$-3.44 \leq \frac{2 \sin(ax) \sin(bx)}{ax \cdot bx} - \frac{\sin(cx)}{cx} - 1 \leq 1.22. \quad (2.31)$$

The only way any system can bifurcate from a stable state into an unstable state (leading to spontaneous alignment) is by altering the sign of either $\text{Tr } J$ or $\text{Det } J$ (figure 2.8). However since the $-K\alpha + \gamma - r_0$ term must be less than zero⁵, the stability of the equilibrium state (an isotropic distribution of filaments) is dependent on σ and ρ . Therefore, in the context of this model, regulation of polymerisation alone (represented

⁵ $r_0 \geq 0$, as this represents the background rate of actin synthesis, and $K > \gamma/\alpha$ because otherwise the equilibrium point is un-physical. Note this also means the leading term in equation 2.28 is positive.

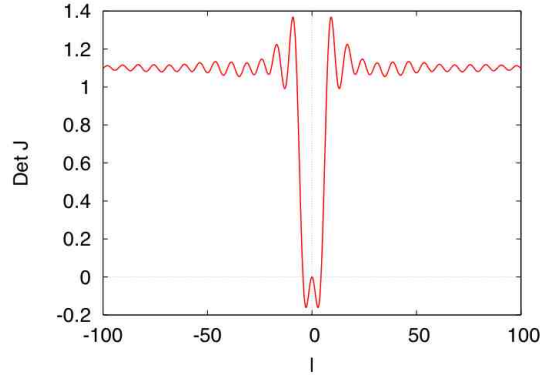


Figure 2.10: Det J plotted using the values for σ and ρ defined in figure 2.9 and treating l as a continuous variable. Parameters are as in figure 2.7. Since for some values of l , Det $J < 0$ the system is unstable, hence the filaments align spontaneously (figure 2.7). Recall that l defines the perturbation modes of the analysis.

here by α and γ) can not lead to alignment of the filaments. However, alignment could be initiated by altering σ or ρ -or indeed ω and η . Biologically this could correspond to up-regulation of binding proteins, for example activation of myosin II, which changes the probability that two adjacent filaments interact and the rate in which they do so.

These analytical results were validated by comparison of equations 2.28 with numerical simulations (figure 2.11). Taking σ as an example, the Routh-Hurwitz criteria is broken for $\sigma \leq 0.389$ (3 s.f) which, up to the numerical accuracy, matches the numerical results (figure 2.11). Note that θ is discretised as $\theta_{i+1} - \theta_i = 2\pi/n$ (equation 4.50) and that the numerical simulations in figure 2.11 are implemented with $n = 200$, so $\theta_{i+1} - \theta_i \approx 0.03$. This limits the accuracy of the numerical analysis to ± 0.015 , (this is the rationale for varying σ in intervals of 0.03, figure 2.11). Hence from figure 2.11 it can be deduced that the bifurcation occurs in the interval (0.37:0.4). Greater accuracy could be achieved by increasing n , however computational cost begins to become prohibitive (there are n equations each with $\approx 2n^2$ terms, equations 2.16). In accordance with the analytical results above, varying α or γ did not alter the stability properties of the system.

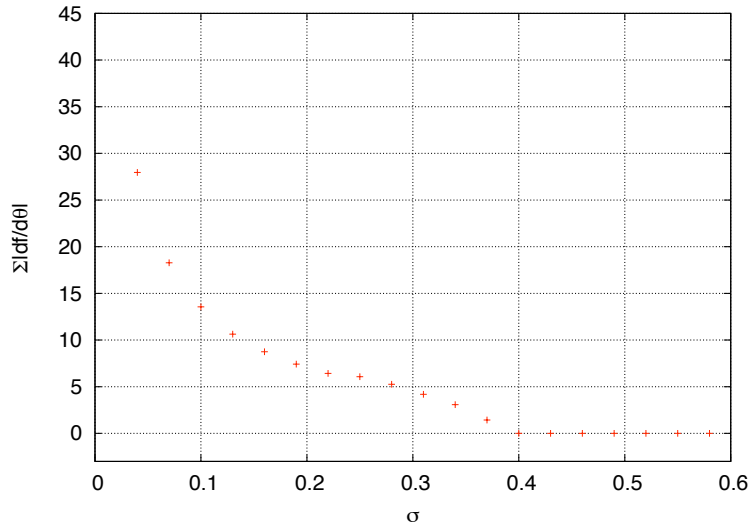


Figure 2.11: Spontaneous alignment of $f(\theta, t)$, quantified as $\Sigma|df(\theta)/d\theta|$ (concentration/radian), where $f(\theta)$ is the steady state distribution. So for isotropic states this measure is zero. This measure is plotted against σ (radians), which recall defines the range of angles that filaments can turn to following interaction (figure 2.9). The numerical simulations indicate that the isotropic state is stable for $\sigma \geq 0.4$. For these simulations $n=200$, other parameters as figure 2.7.

2.4.3 Discussion of Integro-differential Model

Some important insights are provided by this model. Firstly from simple realistic considerations a model of how filaments spontaneously align can be constructed. Although this is a coarse-grained model and the physical binding of actin bundling proteins is not considered, it is still nevertheless of interest because it describes the net effect of actin bundling.

In this model the alignment direction was dependent on the initial random noise, and hence random itself. From this it is tempting to conclude that relatively small signals can be amplified into the global filament alignment by bifurcation into an unstable state. It is important to point out there is no *a priori* reason, other than an aesthetic one, why alignment should be due to such a bifurcation.

The model suggests that increased polymerisation of actin filaments can not lead to filament alignment, however the effect of introducing a spatial component and allowing heterogeneous actin polymerisation across the cell remains unexplored. The stability

analysis suggests that alignment must occur due to bundling of existing filaments rather than *de novo* polymerisation. In this model, equation 2.13, polymerisation is isotropic (depolymerisation is only isotropic for an isotropic distribution of filaments), however *in vivo* it may be the case that anisotropy could be introduced into the distribution of filament orientation by directed polymerisation. Yeast homologues, Bni1 and Bnr1, of formins (proteins that can act as nucleators of actin polymerisation) have been shown to direct actin polymerisation and polarise cell growth (Evangelista *et al.*, 2002); actin binds to formins (locally activated by Rho GTPases) which promotes polymerisation at the barbed end of the actin filament, leading to growth of the filament away from the zone of local activation. The barbed end of the actin filament is fixed to the formin. The mechanism of monomer addition at this point may involve a 'leaky capping' of the filament, section 5.1.3. In ECs there is a region of signalling in the downstream region, activation of formins in this region could initiate filament alignment either directly or by introducing a small bias in the distribution of filament orientation, which (according to this modelling) could cause spontaneous alignment of filaments.

There is a different, or complementary, possibility for the cause of filament alignment. In the downstream signalling region of ECs responding to fluid flow a flat protrusive structure called a lamellipodia is formed (Mott & Helmke, 2007). In keratocytes and fibroblasts lamellipodia consist of a branched network of actin, with the barbed ends of branches orientated approximately to the edge of the cell (Svitkana & Borisy, 1999). This network gets pulled out of this region by acto-myosin contraction (there is a retrograde flow of actin away from the cell periphery Ponti *et al.* (2004)). Hence near this region proteins that bundle filaments into parallel fibres, for example myosin II, do not act on an isotropic distribution of filaments but a pre-orientated distribution. This may introduce enough bias (possibly with additional bias from formins induced polymerisation) in the filament distribution to cause alignment in the flow direction.

Formation of lamellipodia by ECs (in non-confluent layers) responding to fluid flow also plays a role in changing the morphology of ECs, which is crucial in aligning the cell with the flow (Mott & Helmke, 2007). *De novo* actin polymerisation, nucleated by the protein complex Arp2/3, is thought to exert a force on the cell membrane causing the membrane to extend in this region, and formation of the lamellipodia (Mogilner & Oster, 1996; Goley & Welch, 2006). The details of this mechanism and a model that supports this hypothesis are the subject of the next chapter.

3 Brownian Dynamic Modelling of Arp2/3 complex nucleated Actin Polymerisation

To change shape endothelial cells regulate polymerisation of actin. The topic of this chapter is how this polymerisation leads to generation of force and extension of the cell membrane. This polymerisation is known to occur in the downstream edge of ECs in response to fluid flow.

To study force generation by polymerisation of actin in the downstream regions of ECs a Brownian dynamic (BD) model is implemented. A BD approach is a stochastic model (that implicitly encapsulates random motion) that determines the equation of motion of a collection of discrete objects. In this model the objects are actin dimers, an actin binding complex (Arp2/3) and connected objects representing the plasma membrane. If a certain pair of proteins are within a specific distance they are prescribed a finite, if small, chance of binding. Hence BD modelling is an attractive approach to modelling actin polymerisation. A simple model of the membrane is implemented to test if polymerisation can exert a force on the membrane. Firstly there is an introduction to the biology that governs actin polymerisation and nucleation by the Arp2/3 complex *in vivo*.

This work was carried out in the Kamm Laboratory at the Massachusetts Institute of Technology in collaboration with Tae Yoon Kim. Tae Yoon Kim and I modified an existing BD model of actin polymerisation to investigate Arp2/3 nucleated polymerisation and the hypothesised subsequent membrane protrusion. We contributed equally to this modification.

3.1 Lamellipodia

Eukaryotic cell migration and morphological change both rely, initially, on a similar mechanism of structural re-organisation: regulated *de novo* polymerisation of actin filaments. This polymerisation forces the membrane to extend, and hence the cell changes shape in the region of polymerisation leading eventually to the altered shape of the whole cell.

Extension of the plasma membrane can take several forms, the most common being filopodia or lamellipodia. In contrast to thin and flat lamellipodia, filopodia are ‘finger-

shaped' protrusions. Cdc42 and/or Rif mediates this process by activating diaphanous related formins (Peng *et al.*, 2003), which gives rise to aligned parallel bundles of actin filaments. Polymerisation of these bundles drive the filopodium extension (Ridley, 2006).

3.1.1 Regulation of Lamellipodia

The focus of this chapter is modelling the formation of the actin structures that give rise to lamellipodia. In both migration and EC polarisation, formation of lamellipodia is crucial in altering cell morphology. Lamellipodia are very thin but broad (typically about 250 nm in depth, Abraham *et al.* (1999)) portions of the cell that push forward into a region ahead of the rest of the cell (figure 3.1). In lamellipodia actin filaments are organised into a distinctive branched network (Svitkana & Borisy, 1999). Continuous polymerisation of actin into a 'tree-like' structure is believed to be crucial in generating the force required to drive a lamellipodium forward.

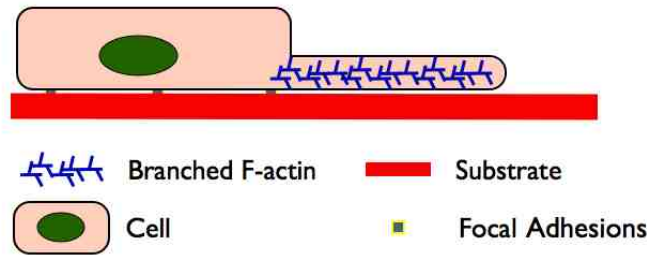


Figure 3.1: A cartoon of lamellipodium extension. In the hidden dimension the extension is typically as wide or wider than the cell.

Actin filaments are polymerised from the 43 *kd* G-actin protein. The structure of the filament is a helix (figure 3.2), with adjacent pairs of G-actin wrapping around each other (Holmes *et al.*, 1990). The barbed (or plus) end of the filament has distinct binding properties to the pointed (or minus) end, which results from asymmetry in the G-actin sub-units. Kinetic rate constants are larger at the barbed end for both polymerisation and depolymerisation (Cooper & Schafer, 2000).

Actin is an ATPase - it binds and hydrolyses⁶ ATP, and in both the monomeric or filamentous forms can be either ADP or ATP bound. At the barbed end of the filament

⁶ATP + H₂O → ADP + inorganic phosphate (Pi)

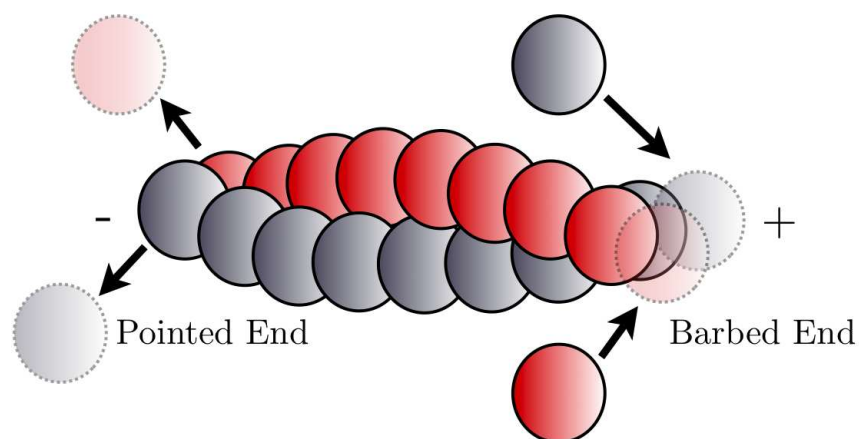


Figure 3.2: Actin filaments are helices composed of G-actin monomers, here represented by spheres.

polymerisation of ATP-actin is faster, whereas de-polymerisation from the filament is slower if the actin unit is ATP-bound, (Schafer & Cooper, 1995). However, in filaments ATP-actin has a half life of 2 s (Zheng *et al.*, 2007). Because polymerisation is more likely at the barbed end this leads to a ‘time-signature’ for the filament: newer ATP-bound units at the barbed end and older ADP-bound units at the pointed end. This signature allows preferential binding of agents to near the barbed or pointed ends depending on whether the species has a higher affinity for binding to ATP or ADP-bound actin (Sablin *et al.*, 2002).

Polymerisation and depolymerisation can be inhibited by capping of the barbed or pointed ends (i.e. the G-actin binding site is blocked by binding of a different protein). Known capping proteins for the barbed end include CapZ and Gelsolin (Cooper & Schafer, 2000). For the pointed end Arp2/3 is an important cap; in lamellipodia this is particularly relevant (Mullins *et al.*, 1998). Capping proteins for the barbed end, such as Gelsolin, bind and inhibit polymerisation, ensuring that the competition for G-actin monomers between mature and nascent branches is in favour of the latter. This gives rise to a structure of short and regular branches. However capping of the pointed end by Arp2/3 inhibits depolymerisation, ensuring there is a bias towards polymerisation and growth of the actin network. Depolymerisation is up-regulated by Actin Depolymerisation Factor (ADF)/Cofilin which acts to sever existing filaments providing both free barbed and pointed ends of filaments (Cooper & Schafer, 2000).

Actin polymerisation initially requires nucleation with two or three actin monomers coming together to form a dimer or trimer. It is widely known that this is the rate-limiting step in actin polymerisation (Mullins *et al.*, 1998; Welch *et al.*, 1998). If the plasma membrane is to be driven forward by actin polymerisation then it is this step which has to be locally upregulated in lamellipodia.

Regulation of actin polymerisation is crucial to correct cellular function. Key mediators of this process are the GTPases Cdc42, RhoA and Rac1. In the case of lamellipodium extension it is Rac1 (and possibly Cdc42) that is implicated as being one of the main mediators of this process. Rac1 activates WAVE proteins, which act as a link in the signalling network between Rac1 and the Arp2/3 complex (Ridley, 2006). Rho GTPase biology and how they get activated in the process of EC alignment is discussed in chapter 6.

Arp2/3 has been shown to be required for lamellipodium extensions (Svitkana & Borisy, 1999; Craig & Chen, 2003; Pollard *et al.*, 2000; Zuo *et al.*, 2006), and is a seven-unit complex named after two of its components: actin related protein 2 and actin related protein 3 (Arp2 and Arp3). Both of these share homology to actin (Robertson *et al.*, 2001). Once Arp2/3 is activated by WASP/WAVE, and bound to an actin filament⁷, it can nucleate the growth of a side branch. It is highly effective in achieving this because in this configuration Arp2 and Arp3 form a binding site homologous to the barbed end of an actin filament (Rouiller *et al.*, 2008).

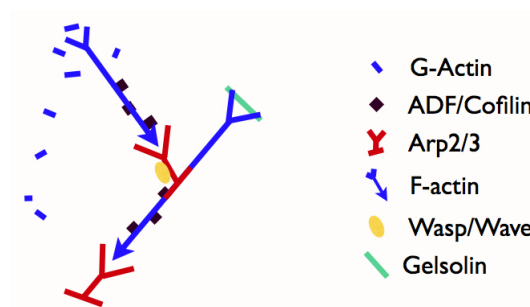


Figure 3.3: Arp2/3 nucleated actin branching and regulation. The arrow represents the pointed end of the filament.

Activation of Arp2/3 occurs locally near the cell membrane (Svitkana & Borisy, 1999). The spatial localisation of active Arp2/3 near the membrane is due to activated Rac

⁷Binding is widely thought to occur to the side of a filament, however it could be the case that it binds to the tip of the filament (Amann & Pollard, 2001).

being localised to the cell membrane due to prenylation followed by methylation of the C-terminus (Seabra, 1998). Whether Rac gets targeted to the leading edge of the lamellipodium, or whether it only gets activated in this region is unclear. One possible mechanism for this is explored in chapter 6.

Arp2/3 nucleates new polymerisation of actin by creating more barbed ends available for monomers to bind to. The new branches of F-actin occur at a highly distinctive angle, reported as $70 \pm 7^\circ$, (Mullins *et al.*, 1998) (figure 3.3). If a tread-milling case of polymerisation is to be achieved (for sustained lamellipodium extension) then the network has to be regulated so there is sufficient Arp2/3 and actin monomers to nucleate and polymerise respectively. Crucial to this regulation is capping of the pointed and barbed ends and severing of the filaments (figure 3.3). In lamellipodia Arp2/3 is at a high enough concentration to cap almost all of the pointed filaments (Mullins *et al.*, 1998). During lamellipodium extension these competing factors must act synergistically so that polymerisation, branching and force generation on the membrane all occur.

3.1.2 Force Induced by Actin Polymerisation

In order for a cell to move or change shape a force is required to extend the membrane in a given direction. It is well documented that actin polymerisation can provide a protrusive force *in vitro* (Footer *et al.*, 2007). Most of the well known *in vivo* examples occur in bacteria motility such as *Listeria Monocytogenes* (Welch *et al.*, 1997). In this example it is a bacterial surface protein, ActA, that interacts with Arp2/3 resulting in actin polymerisation.

A model for how actin polymerisation generates a force that can lead to sustained membrane extension has been proposed (Peskin *et al.*, 1993; Mogilner & Oster, 1996). In this so-called ‘Brownian Ratchet’ model the actin filament tip pushes on the membrane. Sustained membrane protrusion is hypothesised to occur due to Brownian fluctuations in the membrane and filament allowing sufficient time and space for polymerisation at the tip. Hence the membrane is ‘ratcheted forward’ (figure 3.4).

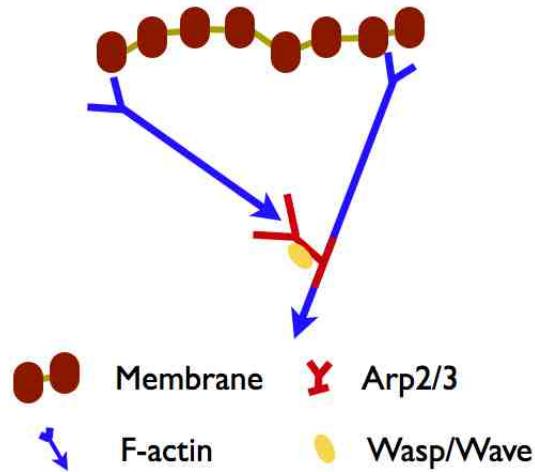


Figure 3.4: Brownian ratchet force generation due to actin polymerisation at the membrane. Polymerisation occurs at the barbed ends of actin filaments orientated towards the membrane. Force on the membrane is supposed to be generated from sustained polymerisation. The space for new polymerisation between the barbed end and the membrane is generated by Brownian motion of the membrane and the filaments.

3.2 Modelling of lamellipodium extension

The modelling in this section was carried out at the Massachusetts Institute of Technology funded by a Bogue Fellowship from UCL. It was carried out in collaboration with Taeyoon Kim in the Kamm Laboratory.

Despite the Brownian ratchet model being widely accepted it is clearly problematic to test *in vivo*. The goal of this modelling work was to develop an explicit model of Brownian ratchet motion due to Arp2/3-nucleated polymerisation. The theoretical statistical mechanics of the Brownian ratchet model was established by Peskin *et al.* (1993).

To model the actin filament network in lamellipodia an existing Brownian Dynamic (BD) model originally by Kim (2007), was modified to include Arp2/3 and a simple model of a membrane.

Computational modelling of membrane protrusions and cell motility arising from actin polymerisation is a rich vein of research and is underpinned by the statistical mechanics (initially applied in the context of a thermally fluctuating load, which in the lamellipo-

dia is the membrane) derived by Peskin *et al.* (1993). This was furthered by Mogilner & Oster (1996) who showed that a thermally fluctuating growing polymer can itself generate force.

Previous modelling in this area has included describing an equation of motion for the filament orientation distribution (Carlsson, 2003), which is similar in concept to the model presented in section 2.4. Using this model Carlsson (2003) investigate a growing and branching network. Interestingly, the dynamics of the simulated network are notably distinct for networks generated either by branching at the very tip of filaments or by branching from the side of filaments. However, it is now widely believed that Arp2/3 binds to the side of filaments (Rouiller *et al.*, 2008; Goley & Welch, 2006).

Dawes *et al.* (2006) presented a 1D model of actin filament branching in a motile cell. In this model the authors derived partial differential equations for the density of actin filaments, the density of barbed ends and the concentration of Arp2/3. Interestingly Dawes *et al.* (2006) show that these equations have travelling wave solutions, from the speed of this wave they predict how the cell velocity depends on the rates of capping, nucleation, and polymerisation. Schaub *et al.* (2006) also estimate the parameters of the actin network, their approach is to generate simulated images from a stochastic 2D model of branching at the leading edge, in this model the leading edge moves independently of the growing filaments. Unfortunately the parameters found by these studies can not be used in the following model (section 3.2.1), which is discrete and stochastic (as oppose to the model by Dawes *et al.* (2006) which is continuous and deterministic). Furthermore, the time scaling of the following model (section 3.2.1) is unrealistic for reasons which will be discussed. Marèe *et al.* (2006) derive a force on the cell membrane at the leading edge of a migrating cell. This force is dependent on the number of barbed ends at the leading edge, however is specifically for application in the context of a cellular Potts model.

The model here is closest in similarity to the 3D brownian dynamic models presented by Carlsson (2001). In this paper several models are presented and Carlsson (2001) demonstrates that branched structures orientated to the membrane are obtained in the cases where branching occurs preferentially in this direction or if there is uncapping of barbed ends in this region. A similar assumption will be made in the following model.

The model presented in the following section is a 3D stochastic model of actin polymerisation and is the work of this author and Tae Yoon Kim, MIT. Polymerisation is modelled explicitly by addition and loss of sub-units and polymers have elastic and

bending stiffnesses. The Arp2/3 complex and its subsequent nucleation of *de novo* polymerisation is considered explicitly. Furthermore ATP-ADP hydrolysis, capping and severing are implicitly implemented. Hence this model represents a novel contribution in this area.

3.2.1 Brownian Dynamics

Brownian dynamics (BD) is a modelling approach where individual agents are modelled as spheres. Here due to the helix-like structure of actin filaments (figure 3.2), a sphere represents a pair of actin monomers. Hence actin filaments are represented as a chain of bound spheres, and the bond between spheres is modelled by a spring-like force. Forces imparted by solvent molecules are modelled by a stochastic force. To evolve the positions of the spheres $F = ma$ is applied. However, in this case the force on the sphere, F , is a summation of drag forces, stochastic forces and forces due to other spheres (either from bonds or Van der Waals forces). Applying $F = ma$ with these forces gives what is referred to as a Langevin equation, which in this case is:

$$m \frac{d^2 \mathbf{r}}{dt^2} = \sum_{i \neq j} \mathbf{f}_{ij} - \zeta \frac{d\mathbf{r}}{dt} + \bar{\eta}(t) \quad (3.1)$$

where m is the mass of the sphere, $\mathbf{r}(x, y, z)$ its position, ζ is the drag coefficient for a sphere, $\eta(t)$ is a stochastic force representing the Brownian motion of the spheres and \mathbf{f}_{ij} is the force on the i th monomer due to the j th (in the computation of the model only nearby pairs are considered). For any given sphere there are several possible constituents of this force term: a repulsive potential, bending stiffness, spring force and torsional stiffness. The latter three result from sharing a bond with other spheres.

The stochastic force is chosen from a distribution such that $\langle \eta(t) \rangle = 0$ and

$$\langle \bar{\eta}_i(t) \bar{\eta}_j(t) \rangle = \frac{2k_B T \zeta \delta_{ij}}{\Delta t} \mathbf{I}$$

where subscripts are labels for each sphere, \mathbf{I} is the unit second order tensor, k_B is the Boltzmann constant, ζ is the drag on the sphere (taken to be Stokesian), T the temperature and δt the time step (Underhill & Doyle, 2004).

The acceleration term in equation 3.1 is considered to be negligible; consider that the spheres are very small particles moving in a continuous viscous fluid, hence any accelerated sphere will reach its terminal velocity quickly. Therefore the acceleration term

only has a negligible contribution to the equation of motion for a sphere. Applying this and non-dimensionalising by $k_B T$, ζ and the diameter of an actin filament A ⁸ equation 3.1, can be recast as

$$\frac{d\mathbf{r}'}{dt} = \sum_{i \neq j} \mathbf{f}'_{ij} + \bar{\eta}'(t) \quad (3.2)$$

The potential between two spheres is modelled as a truncated Lennard-Jones (L-J) potential (Lennard-Jones, 1931) so that only repulsive forces are considered, ensuring that two spheres do not occupy the same physical space. The L-J potential has the form

$$V(r) = \begin{cases} 4\epsilon \left[\left(\frac{\sigma}{r^{12}} \right) - \left(\frac{\sigma}{r^6} \right) \right] & r \leq 2^{1/6}\sigma \\ 0 & r > 2^{1/6}\sigma \end{cases} \quad (3.3)$$

where r is the distance between the spheres, ϵ represents the depth of the potential well and σ is the point where the potential is zero and is taken as the average diameter of the interacting spheres⁹.

Once an actin monomer comes within a certain radius (1.2 units) of a barbed end (or Arp2/3) binding occurs. Similar binding occurs for Arp2/3 and the side of a filament. In this model, the binding sites for Arp2/3 on the filament have an orientation that has the same periodicity as the actin helix (approximately 70 nm). A torsional stiffness is applied to the relative orientation of simulated binding sites on subsequent spheres in the polymer.

The distance between adjacent bound spheres, the curvature of the filament and the relative orientation of binding sites are maintained by the spring-like potentials:

$$U_1(W_1) = \frac{1}{2}k_1W_1^2, U_2(W_2) = \frac{1}{2}k_2W_2^2, U_3(W_3) = \frac{1}{2}k_3W_3^2 \quad (3.4)$$

where W_1 is the distance from the equilibrium separation of bound spheres (A), W_2 is the angular distance away from the equilibrium dihedral angle between binding sites on adjacent spheres ($\pi/5$ - the actin filament is periodic in about every 10 sub-units - figure 3.2) and W_3 is the angle that three consecutive actin spheres make relative to the orientation of the other two (so in this case the equilibrium angle is zero). k_1, k_2

⁸To non-dimensionalise write 3.1 (in the absence of acceleration) as $\mathbf{F} = \zeta\dot{\mathbf{r}}$, where \mathbf{F} is the total force on a particular sphere. Write $\mathbf{F} = \alpha\mathbf{F}'$, $\mathbf{r} = \beta\mathbf{r}'$ and $t = \lambda t'$, where the primed variables are non-dimensional and α, β and λ are constants defining the non-dimensionalisation, then the non-dimensionalisation is performed by taking $\alpha = k_B T/A$, $\beta = A$ and $\lambda = \beta\zeta/\alpha$.

⁹In this context all the interacting species have a diameter normalised to 1 unit from a real diameter of 7 nm, approximately the diameter of an actin filament.

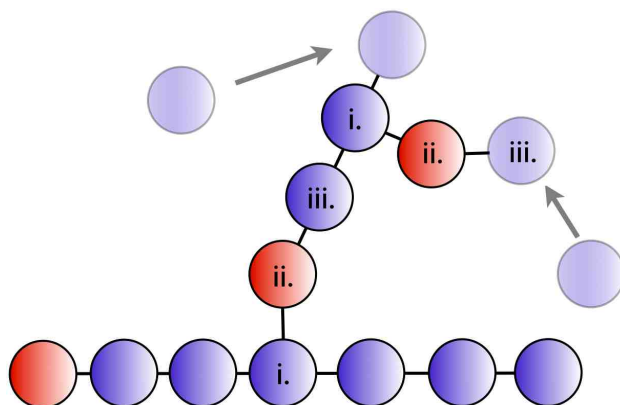


Figure 3.5: Schematic of binding in the BD model. Arp2/3 in red, actin in blue. Arp2/3 binds orthogonally to the side of existing filaments (i. - ii.). New branches are nucleated, orientated at approx 70° to the parent filament (ii. - iii.). The angles are maintained by applying a bending stiffness to the binding angle. Filaments are assumed to be pre-capped by Arp2/3 at the pointed end.

and k_3 are constants - refer to table 3.1 for the parameters that are not varied in these simulations, other parameters are reported where appropriate.

Bending stiffnesses are also applied (with the same spring constant, k_2) so that the chain Arp2/3-actin-actin is at 70° to the filament and so that Arp2/3 binds orthogonally onto the filament (figure 3.5).

Parameter	Value	Units
Actin Monomer Diameter - A	7×10^{-9}	m
Boltzmann Energy - $k_B T$	4.142×10^{-21}	J
Friction Coefficient of Actin Monomer - ζ	5.673×10^{-11}	Kg s^{-1}
Time Step Δt	20.13×10^{-12} (3×10^{-5})	s
Spring Constant of filaments - k_1	0.1691 (2,000)	N/m
Bending stiffness of filaments - k_2	1.243×10^{-17} (3,000)	N m
Torsional stiffness of filaments - k_3	4.142×10^{-17} (1,000)	N m
Cutting length - l	2.1 (0.3)	nm

Table 3.1: Parameter values used in the Brownian dynamic model, dimensionless values in parentheses.

A limitation of this model of actin polymerisation is that polymers form several orders of magnitude faster than *in vivo*, although this is computationally advantageous. The reader is referred to Kim (2007) for further details of the actin polymerisation model; here the focus is on the alterations to this model to include Arp2/3-nucleated polymeri-

sation near the cell membrane; the weaknesses of the actin model will be discussed in this context.

Capping of the filaments is modelled by assuming that all the pointed ends are capped by Arp2/3, and barbed end capping is modelled by the probability of the binding of a sphere to a filament F being proportional to the length of the filament

$$P(\text{Bind to F}) = e^{-(n-1)} \quad (3.5)$$

where n is the number of spheres in the filament. The justification for this is that the length of the filament is correlated to its age and the probability of being capped increases with the age of the filament (assuming a constant probability of being capped in any time interval). This assumption avoids the complication and additional computational cost of introducing a different species to cap the filaments. It is further assumed that Arp2/3 can only nucleate polymerisation once bound to the filament. In the initial simulations there is no severing of filaments and no depolymerisation. Hence the network is permanent once formed.

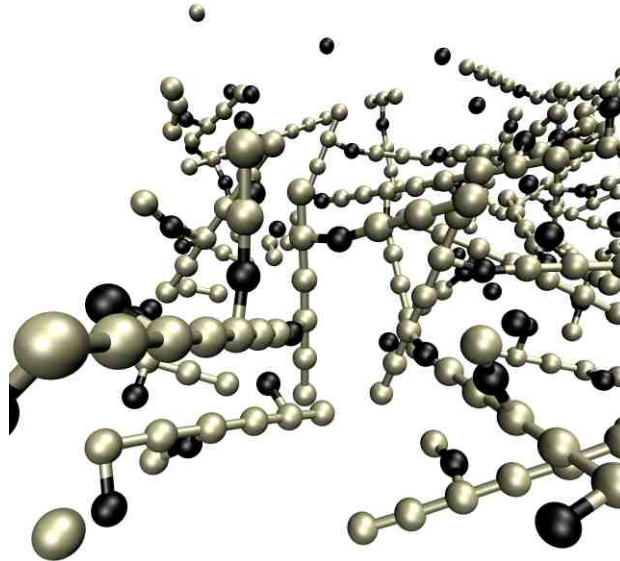


Figure 3.6: Arp2/3-nucleated branching and regulation in the simulated actin network. Light spheres represent actin dimers and dark spheres Arp2/3

With these assumptions a branched network of regularly branching actin is generated

(figure 3.6). However in the *in vivo* case the orientation of the actin filaments is towards the membrane. It is suggested that it is the physical confinement of the filaments in the thin lamellipodium that provide this directionality (Shao *et al.*, 2006), however it may be due to Arp2/3 being activated only at the membrane.

In order to test the theoretical Brownian ratchet model computationally a simple model of the membrane is introduced into this model. Since a renewable population of monomers is required for sustained polymerisation, severing of the filaments is also considered in this new scenario. The additional computational cost of introducing a separate species to bind to and then sever the filaments is circumvented by assuming that filaments of a certain age will be severed. The system introduced to sever the filaments is outlined in figure 3.7. In this process the rear of the network is severed. The biological justification for this is that severing proteins such as ADF/Cofilin bind preferentially to ADP-bound actin (Kovar, 2006) which will be more prevalent in the rear of the network (which in principle is more mature).

This severing and cutting method is reminiscent of the *in vivo* case; due to acto-myosin contraction (refer to chapter 6 for how the Rho GTPase Rho mediates this contraction) there is a retrograde flow of actin of about 400 nms^{-1} , (Ponti *et al.*, 2004). However in these simulations, this corresponds to a negligible 2 pm per 5×10^7 time steps and hence is ignored. Retrograde flow, may play a role *in vivo* as the typical time-scale of lamellipodium extension is much longer than these simulations.

The lipid bilayer is initially coarsely modelled by 6 x 6 spheres, which define a surface mesh of triangles. These points are constrained to move only in the z -direction, although in reality the membrane is 2D fluid structure.

This surface exerts an L-J force on nearby filaments and monomers. An equal and opposite force is exerted by filaments on the surface. The force from monomers on the surface is assumed negligible.

The restoring force (which resists the force from filaments) is modelled as a stiffness acting on the dihedral angle, θ_m , between two - triangular -planar surfaces, each comprised of 3 spheres. The equilibrium state of the membrane is assumed to be a flat surface, so that at equilibrium $\theta_m = \pi$. Hence the potential modelling this force is taken as:

$$U_m(\theta_m) = \frac{1}{2}k_2(\theta_m - \pi)^2 \quad (3.6)$$

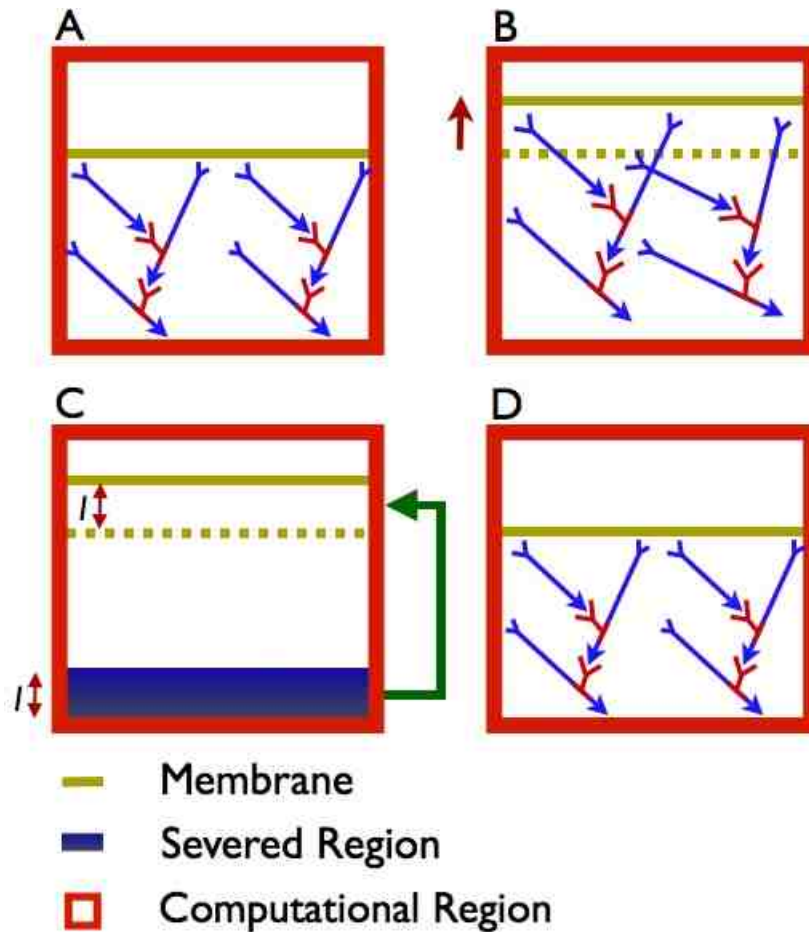


Figure 3.7: Method of severing the actin network. A: The initial configuration. B: The membrane advances due to polymerisation behind it. C: Once the membrane has moved a pre-defined distance, l , the bottom of the network is cut to a length l . The spheres are replaced from the sides of the computational region near the membrane. D: The distance l is subtracted from the position of every sphere, the system is put back to the original configuration.

The surface is free to move,¹⁰ hence the force that the actin spheres exert on the membrane due to random buffeting pushes the membrane forward. In reality, if the system is in equilibrium, the pressure on the membrane is balanced by the tension in the membrane. To avoid this effect the force on the membrane from the free spheres (and indeed solvent molecules) is assumed to be exactly balanced by a restoring force normal to the membrane due to tension. However, it should be noted that an alternative suggestion to the Brownian ratchet model is that hydrostatic pressure is increased due to acto-myosin contraction and this results in membrane protrusion (Dembo & Harlow, 1985).

The computational region is a cuboid, the top face being the ‘membrane’. The boundary condition on the faces perpendicular to this face are periodic, on the parallel face there is a solid boundary modelled by a repulsive force (justified biologically as a ‘fixed’ mass of polymerised actin).

3.3 Results of the BD model of membrane extension

Here the goal is to test the Brownian ratchet model: can polymerisation lead to motion of the membrane? To quantify the motion of the membrane the average distance of the membrane points is recorded for every time step, then the average velocity of the membrane is simply the gradient of the graph of average distance vs time steps (figure 3.8).

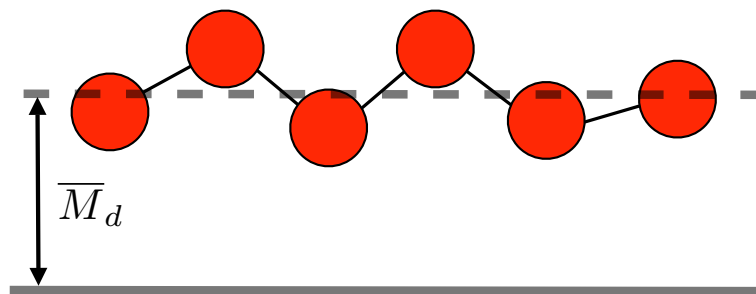


Figure 3.8: 2D schematic of average membrane position. The BD model tracks the average distance (\overline{M}_d) of the membrane (circles) from a reference position (solid grey line).

The initial conditions for the simulation are shown in figure 3.9, where the actin spheres

¹⁰Periodic boundary conditions on the side and the relatively small computational region mean that is awkward to model tension in the membrane by fixing it at the sides.

are arranged in a cubic lattice with Arp2/3 placed in the centre of some of the cubes defined by eight spheres. The polymerisation is seeded by ten bound pairs of monomers. The rate of nucleation (i.e. formation of pairs of spheres) in all these simulations is taken to be zero; this ensures that polymerisation is only induced by Arp2/3 binding to the side of existing filaments.

In each simulation the polymerisation is started from this condition. In principle the simulation could be run from a pre-polymerised network, but - as will be shown - large variation in the results (due to the stochastic nature of the model) mean that running from a pre-polymerised network would introduce a bias to the results.

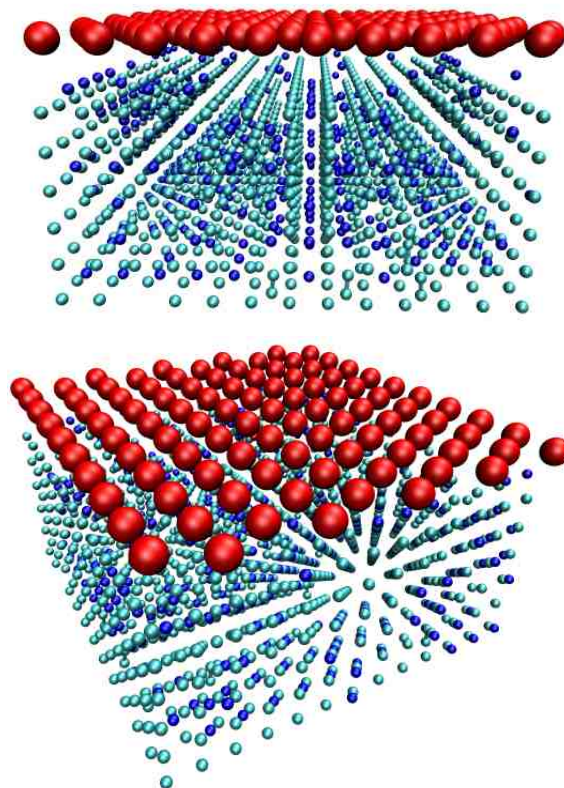


Figure 3.9: Initial conditions in the BD model of membrane extension. Membrane in red, Arp2/3 in blue and actin in Cyan. Note the bound actin on the bottom row - this nucleates the polymerisation. Spheres not to scale. 10×10 spheres define the membrane

Initially a qualitatively similar network was sought to show that the binding of and

branching with Arp2/3 was ‘topologically’ similar to what is observed experimentally. A typical example of the kind of network generated is shown in figure 3.6. Note that the spheres are not to scale (for clarity so the structure can be seen). The ‘tree’ like structure is evident, but clearly the global orientation of the structure is relatively random compared to the orientated branching found in lamellipodia.

To test the model preliminary simulations were carried out. It was found that, in some circumstances, the algorithm for severing the actin network (figure 3.7) could lead to a ‘stalling’ of the system: the membrane does not move the requisite distance because filaments were severed too quickly, and hence no persistent motion of the membrane occurs (figure 3.10). To counteract this the bottom of the computational region is severed if the system has not moved within a certain amount of time steps (initially 10^6 steps). In this scenario the depth to which the severing has occurred is not subtracted from the particle positions. This is so as to avoid compacting the region; if the region is severed (without the membrane having advanced) and this distance subtracted from the positions of all the particles then the concentration of particles is superficially increased.

With this mechanism the overall concentration of actin was kept roughly constant over the simulation time (the concentration is slightly reduced as the volume increases, until the cut occurs, figure 3.7). The concentration was varied by changing the initial separation of monomers in the lattice (it is this that gives rise to choices for concentration of actin, e.g. 0.51 mM in figure 3.10). The range of concentrations chosen are of a similar magnitude as taken in Carlsson (2001), of the order of about 1 mM. This is also comparable to the concentration reported in (Abraham *et al.*, 1999), which is given as 40 mg/mL (1 Molar of 43 kDa G-actin corresponds to 43×10^3 mg/mL). So 40 mg/mL is approximately 1 mM. Here concentrations less than this are taken, the model was found to be slightly unstable with closer packing. The concentration of free actin monomers is typically 10 – 50 μ M (Mogilner & Oster, 1996). 5×10^7 steps corresponds to about 5 μ s.

In all the following results (figures 3.11 - 3.13) there are 36 points defining the surface, 1014 actin monomers (13 by 13 by 6 initially¹¹) and 400 Arp2/3 complexes. Concentration is calculated inclusive of both. Each separate colour represents an independent execution of the model. All the graphs show the average distance (in actin monomer units, 1 unit = 7 nm) of the membrane points from the bottom face (figure 3.8) versus

¹¹Since the number of monomers remains the same a higher concentration results in a smaller computational region, but as an example: 0.51 mM corresponds to a region of 182 nm \times 182 nm \times 98 nm.

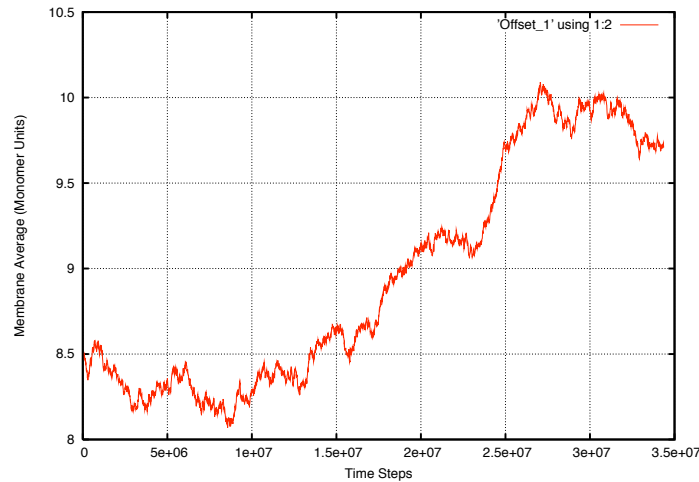


Figure 3.10: Average position of the membrane (figure 3.8) in actin monomer units. Initial simulation at 0.51mM total (polymerised and un-polymerised) concentration. Note the stalling of the system, both in the early stages and after the peak distance has been reached. However, an extension of the membrane of 1.2 monomer units (≈ 10 nm) is achieved.

the number of time steps into the simulation.

It is clear from figures 3.11, 3.12 and 3.13 that sustained motion of the membrane is not being generated. The only promising result is the ‘green’ run (figure 3.12) where there is a steady linear trend.

Figure 3.11 is interesting because the membrane in the ‘green’ simulation has collapsed down rather than being ratcheted forward. This is essentially a ‘random’ walk; recall there is no network of actin initially so nothing to support the membrane. The ‘blue’ simulation (figure 3.11) illustrates a different sort of collapse - the trend is downward after a time in which the network would be significantly polymerised - once this has happened the regular severing starts. It appears that by regularly cutting the bottom of the computational region, the network has no support and the membrane (if the random fluctuation should be in that direction) forces the network down. There is not enough force on the membrane because the filaments do not have anything to push against in the newly severed region. Something similar to this may actually be happening physically: lamellipodia do fluctuate in and out even in steadily migrating cells, though on a different time scale to these simulations (Raucher & Sheetz, 2000). Figure 3.13 emphasises the variability of these results.

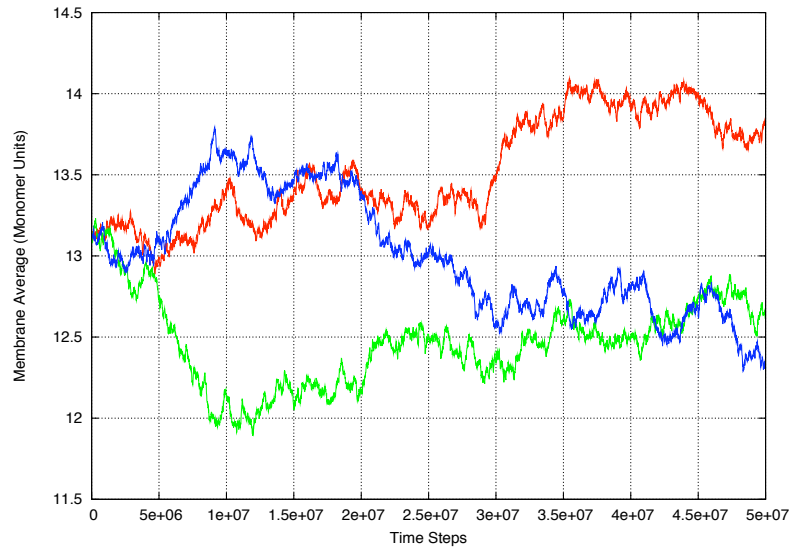


Figure 3.11: BD simulation of lamellipodia. Severing every 10^6 steps. Combined concentration of Actin and Arp2/3, 0.70 mM.

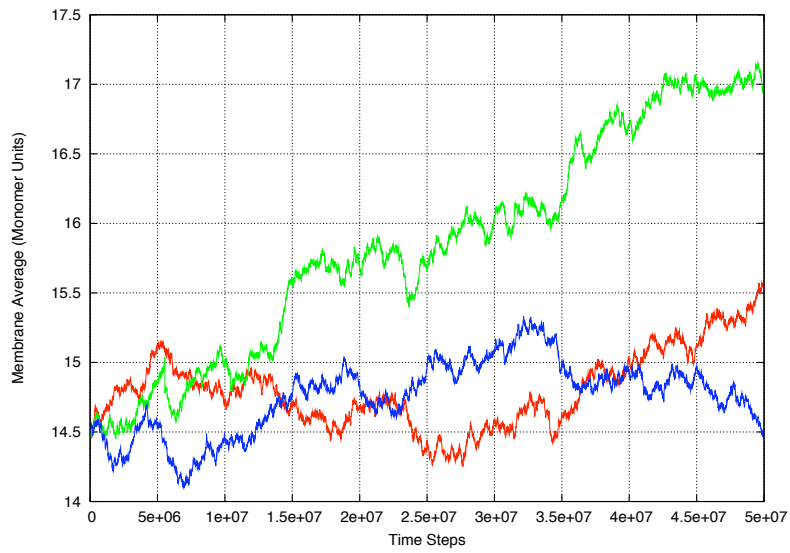


Figure 3.12: BD simulation of lamellipodia. Severing every 10^6 steps. Combined concentration of Actin and Arp2/3, 0.51 mM.

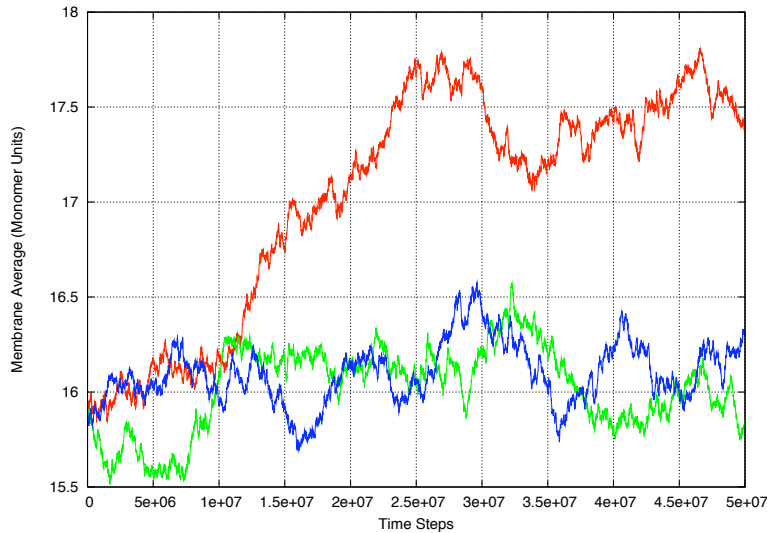


Figure 3.13: BD simulation of lamellipodia. Severing every 10^6 steps. Combined concentration of Actin and Arp2/3, 0.38 mM

To reduce the variability and minimise the random motion of the membrane more membrane points are introduced. Each of these points executes a random walk, however they are not independent due to the restoring force from the neighbouring points. Hence more points will reduce the variation in the average position of the membrane. Note that although this increases the mass of the membrane the dynamics of the simulation, equation 3.1, is independent of mass if acceleration is negligible. In figures 3.14 - 3.16 there are 100 points in the surface. Secondly, on account of the observed collapse of the membrane (figure 3.11), the maximum time between severing events was increased by a factor of 10.

In the previous simulations a concentration of 0.51mM for actin and Arp2/3 was the most promising simulation. Four further simulations were run at this concentration, and two at a slightly higher concentration, 0.59 mM. Three simulations were run at a significantly lower concentration, 0.12 mM, to determine if the membrane moved slower or not at all at this level (figures 3.14, 3.15 and 3.16).

In figure 3.14 a steady linear trend is evident in the 'red' case. In the 'green' case the membrane appears to have 'randomly walked' ahead of the polymerising network, but once it collapses, presumably to the point of polymerised actin, a similar linear trend is recovered - obviously this could still be an essentially random motion, though the

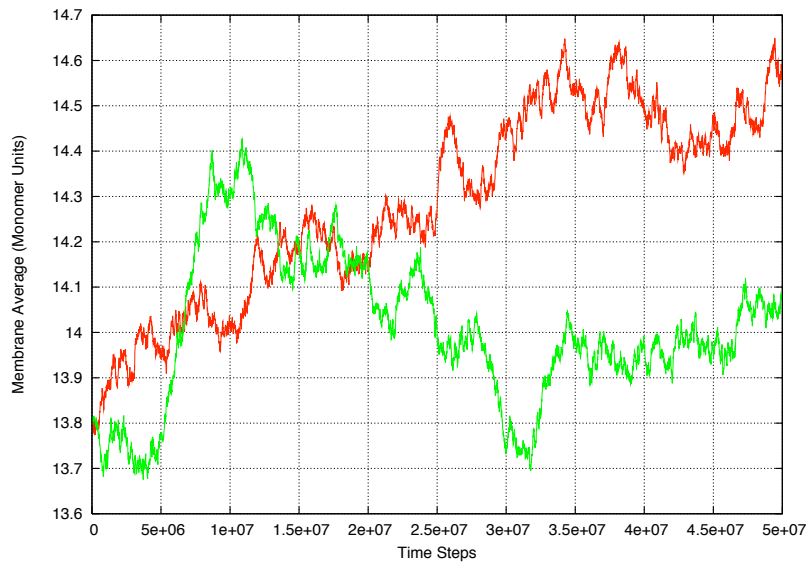


Figure 3.14: BD simulation of lamellipodia. Severing every 10^7 steps. Combined concentration of Actin and Arp2/3, 0.59 mM

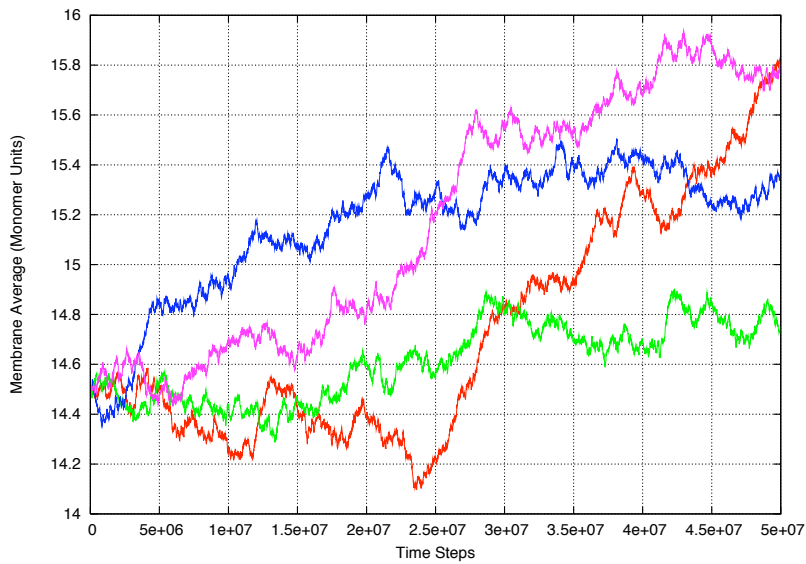


Figure 3.15: BD simulation of lamellipodia. Severing every 10^7 steps. Combined concentration of Actin and Arp2/3, 0.51 mM

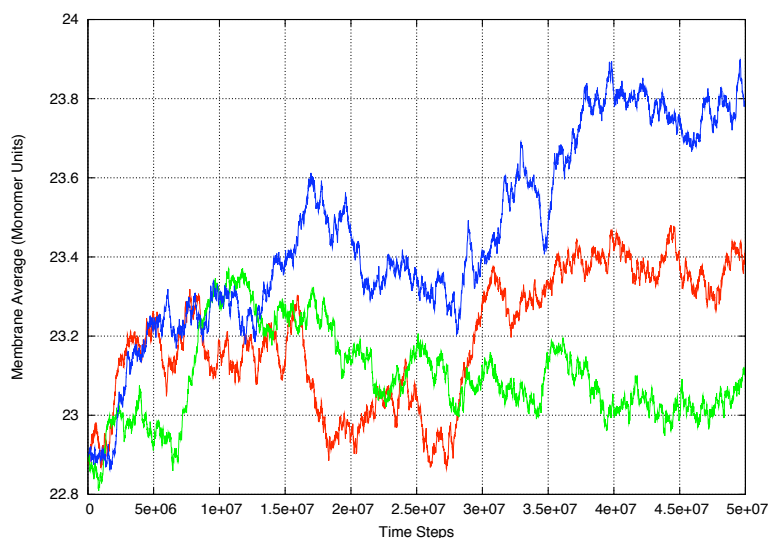


Figure 3.16: BD simulation of lamellipodia. Severing every 10^7 steps. Combined concentration of Actin and Arp2/3, 0.12 mM.

fact that the velocity is similar to the red case is suggestive that the same mechanism of membrane extension is in operation in both cases.

Figure 3.15 again illustrates large variation between the results, but a correlation between the simulations is apparent (at least the average gradients of each run are of a similar order of magnitude). The variation of the results precludes comparing the velocities of the membrane in figures 3.14 and 3.15. However it may be the case that the higher concentration simulation (figure 3.14), exhibits a slower velocity due to a ‘space filling’ effect - at high concentrations unbound spheres struggle to locate to the membrane.

The overall motion seems slower on average in the three runs at a concentration of 0.12mM (figure 3.16).

The final batch of simulations carried out was with a large number of points (in the following results 1296 points were used) in the surface. This should, in principle, reduce the variation in the average membrane position. It should also, if the Brownian ratchet model is correct, reduce the velocity of the membrane because the chance of a sphere finding room between the membrane and a barbed end of a filament is reduced dramatically and hence membrane velocity is reduced.

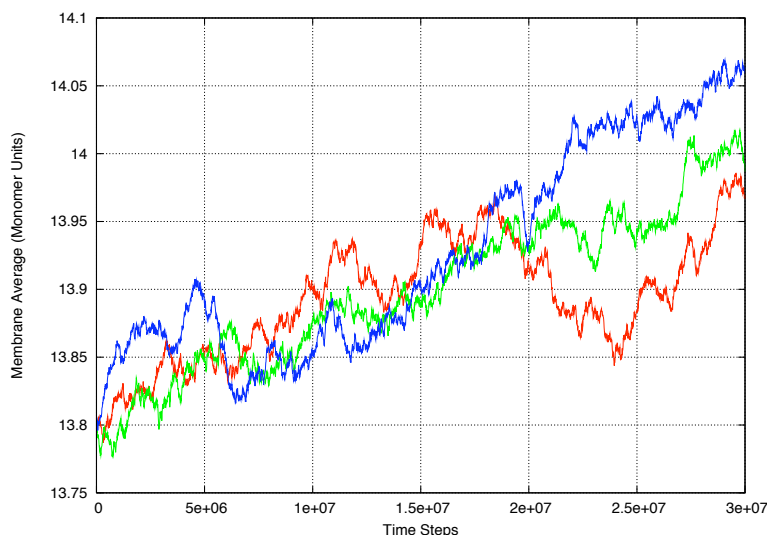


Figure 3.17: BD simulation of lamellipodia. Severing every 10^7 steps and with 1296 surface points. Combined concentration of Actin and Arp2/3, 0.59 mM

Due to increased computational costs these runs are shorter and the concentrations spaced out (figures 3.17, 3.18, and 3.19).

Figure 3.17 shows exactly what was predicted. A steady trend is obtained in all three cases, yet the evident slow velocity of the membrane seems to be good evidence for the Brownian ratchet model.

The concentrations of actin and Arp2/3 used in figures 3.18 and 3.19 appear too low to achieve any sustained extension of the membrane, however over longer time periods polymerisation may still provide a sustained force on the membrane. This is further evidence in favour of the Brownian ratchet model - low actin concentrations reduce the probability of a sphere inter-locating between a barbed end and the surface.

3.4 BD Model of Membrane Extension - Discussion

From these results there are three primary conclusions that can be drawn. Firstly the Brownian ratchet model is strongly supported: the results presented in section 3.3 suggest that, despite the high level of variation, the Brownian ratchet model is certainly a valid hypothesis. Secondly the membrane velocity is strongly influenced by actin

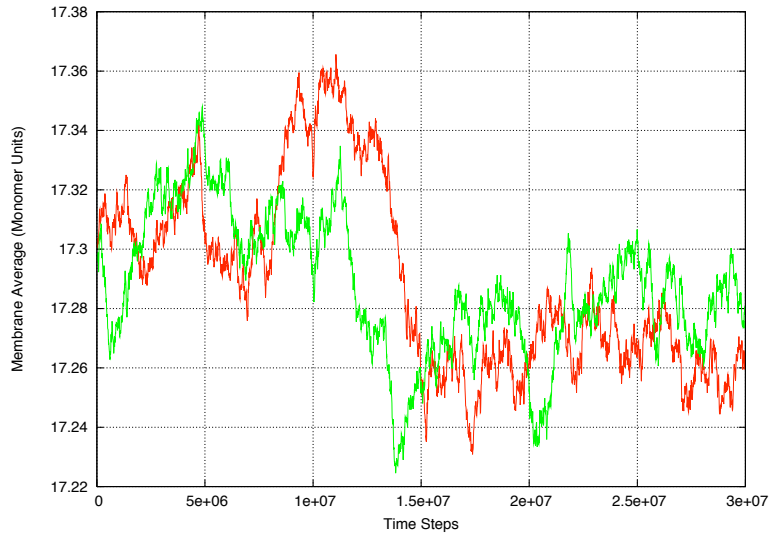


Figure 3.18: BD simulation of lamellipodia. Severing every 10^7 steps and 1296 surface points. Combined concentration of Actin and Arp2/3, 0.29 mM

concentration, primarily due to an increase in polymerisation rate. Lastly severing is important to provide a free pool of actin monomers to maintain polymerisation. The irregular nature of the results may have biological relevance; the simulations show that membrane velocity is highly dependent on free monomer concentration and thus mechanisms to maintain this concentration *in vivo* could provide a method to regulate lamellipodium extension. However the results of this model have to be tempered; only a small region of the total parameter space has been investigated.

At this stage the ratchet model is yet to be verified experimentally, and to do this is clearly technically challenging. This model represents a step towards verifying the theoretical principles of the ratchet model computationally.

In cells the actin filaments are aligned with their barbed ends presented towards the membrane. This model does not reflect this. There are two possibilities for altering the model to reproduce this. Firstly the sides could be constrained by removing the periodic boundary condition and replacing it by a repulsive force representing a solid wall. The scale of the model is well suited to this as its width in the x and y directions (recall the membrane is, approximately, in the x - y plane) is comparable (approximately 200 nm) to the thickness of lamellipodia. Altering the boundary condition on either the z - y or z - x face could provide the spatial confinement thought to give rise to the

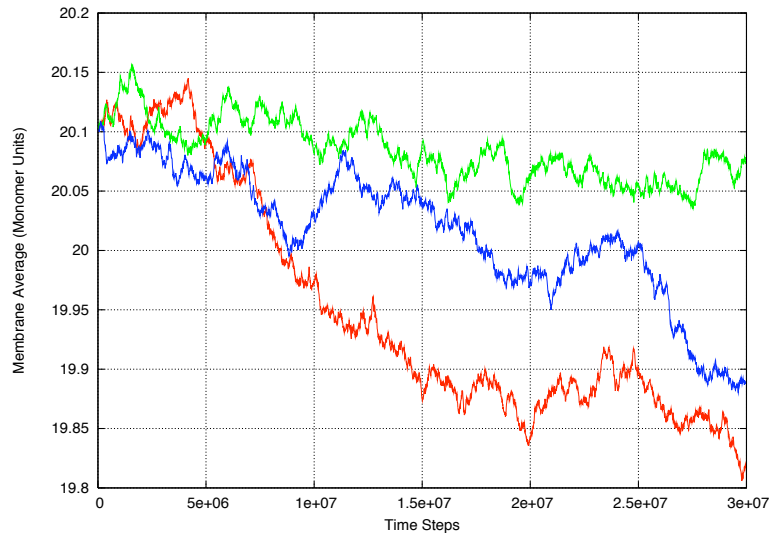


Figure 3.19: BD simulation of lamellipodia. Severing every 10^7 steps and 1296 surface points. Combined concentration of Actin and Arp2/3, 0.019 mM.

orientation. The second possibility is to change the way that Arp2/3 is reintroduced after severing so that it is directly placed back under the membrane rather than from the side, or demand that the spheres representing Arp2/3 only become activated at the virtual membrane.

One method to validate the model is a comparison of velocity of the simulated membrane with the *in vivo* or *in vitro* cases. However, it is evidently too fast. The maximum protrusion of the membrane is reported as being of the order of 20-30 $nm s^{-1}$ (Takahashi *et al.*, 2003), however this is very different to cell migration speed. For example Keratocytes, which move relatively fast...maximum cell migration velocity (approximately 20 μmin^{-1}).

In these results the membrane typically travels on the order of tens of nm in 5×10^7 steps, corresponding to $5 \mu m s^{-1}$. That the velocity is so much faster in these simulations is advantageous for computational reasons, and allows shorter simulations to capture the essence of the process. In fact in the original actin polymerisation model the polymerisation rate of the actin filaments is artificially faster for the same reason (Kim, 2007). The spheres represent actin dimers, rather than monomers - this of course greatly increases the rate of polymerisation.

To construct a model of similar complexity that could reproduce this membrane velocity would be hugely computationally intensive: simulations of the length of a second would be necessary, approximately 200,000 times longer than those presented here (an intractable length of time without alteration to the model). This length of simulation would be necessary to observe a significant displacement of the membrane at this velocity. However the advantages of performing longer simulations are unclear, although it is possible that richer dynamic behaviour would be observed over longer time scales. Lamellipodia are often observed to extend out and then retract back into the cell repeatedly, which could be due growth and collapse regulated by the cell, but it also may result from the network becoming starved of monomers and hence severing dominates (leading to a collapse of the lamellipodium). This leads to a monomer rich environment and resurgence of lamellipodium extension. It could be speculated that some of the simulations here show this sort of behaviour, however the biological relevance of these observations could only be confirmed by longer simulations.

This work was carried out during a limited time period at MIT. Given more time the next stage would be to investigate, computationally, the parameter space. The simulations reported here are only representative of a small region of this space, hence further computations are necessary to support (or contradict) the conclusions made here. Correspondingly these conclusions are tempered by their limited computational support.

To fully investigate of the parameter space it would be hugely advantageous to be able to reduce the computational cost of simulation. Either the code could be further optimized, or the system size reduced. The latter case would require some careful study to allow robust conclusions to hold in corresponding larger systems. Nevertheless, of particular interest to investigate would be:

- Ratio of Arp2/3 to actin
- Severing rates
- Membrane properties
- Branch length

It would be interesting to couple this work to models of different time and length scales, this technical and computational challenges involved in doing so is discussed in chapter 8.

Modelling components of EC polarisation and elongation (figure 1.3) over longer time scales is the subject of the remainder of this project. Specifically; mechano-transduction of force due to fluid flow and Rho GTPase activation, which mediates lamellipodium formation. The subject of the next chapter is modelling the fluid flow over a 3D cell, the solution of which naturally gives the force on the cell surface.

4 Modelling the Flow over a Single 3D Cell

The goal of this chapter is modelling the force that fluid flow exerts on the cell surface. This is achieved by assuming the cell is rigid and solving the Stokes equation over a 3D model of a single cell. Justification for choosing Stokes flow as a model for the flow and derivation of the representation used to solve the Stokes flow, which follows the logic given by Pozrikidis (1992).

Flow over an endothelial cell is modelled as Stokes flow over a bump attached to a wall. This problem has been extensively analysed previously. The following contributions are particularly relevant to this thesis: Hazel & Pedley (2000) studied this problem in the context of ECs and showed that EC alignment minimised the total force on their nuclei, Price (1985) analytically approximated the solution for the total force on a hemispherical bump, Higdon (1985) studied this problem in arbitrary 2D geometries, Pozrikidis (1997) analysed shear flow over axially symmetric protuberances and Wang & Dimitrakopoulos (2006*a,b*) studied flow past a bump attached to a cylinder (representing an artery).

The methodology for solving the Stokes equation is given followed by the results of the model and the biological implications. The novel aspect of the approach presented in this chapter is the solution of the problem using a discretisation which facilitates coupling of a mechano-transduction model (chapter 5) and reaction-diffusion equations (chapter 6), although here the later case is coupled to the model of the flow via the mechano-transduction model.

4.1 Stokes Flow

Blood is a heterogeneous fluid due to the red and white blood cells and platelets that are suspended in plasma (a fluid composed of water, proteins and electrolytes). However, it is thought that there is a thin layer near the edge of the flow that is cell free, hence the fluid (near the endothelium at least) can be modelled as homogenous (Hazel & Pedley, 2000). Furthermore it also approaches a Newtonian fluid at this edge (a Newtonian fluid has a constant viscosity, regardless of the shear forces that act within it), and in large arteries, at least, blood is well approximated by an incompressible fluid (Pedley, 1980).

Here it is assumed blood is a simple, homogeneous, incompressible Newtonian fluid.

This is a simplifying assumption that has the benefit that the best characterised fluids, in terms of mathematical analysis, are incompressible and Newtonian. For such a fluid, conservation of momentum applied to a small fluid element gives the Navier-Stokes equations

$$\rho \left(\frac{\partial \mathbf{u}}{\partial t} + \mathbf{u} \cdot \nabla \mathbf{u} \right) = -\nabla P + \mu \nabla^2 \mathbf{u} + \rho \mathbf{b} \quad (4.1)$$

where the constants ρ and μ are the density and viscosity of the fluid respectively, $P(\mathbf{x}, t)$ is the pressure, $\mathbf{u}(\mathbf{x}, t)$ is the velocity of the fluid and \mathbf{b} is an external force applied to the body, gravity for example. The continuity equation, which arises from demanding mass conservation is

$$\nabla \cdot \mathbf{u} = 0 \quad (4.2)$$

Equation 4.1 is justifiable near the endothelium layer, and this is the point of interest. The equations are non-dimensionalised, in order to estimate a parameter, the Reynolds number, that characterises the flow. The non-dimensionalisation proceeds using the following expressions

$$\mathbf{u}' = \frac{\mathbf{u}}{U} \quad (4.3)$$

$$\mathbf{x}' = \frac{\mathbf{x}}{L} \quad (4.4)$$

$$t' = \frac{t}{T} \quad (4.5)$$

$$P' = \frac{PL}{\mu U} \quad (4.6)$$

where U , L and T are the characteristic velocity, length and time of the flow, here T is taken to be L/U . These constants define the scale and nature of the problem, and hence must be chosen according to this particular case. Making this transformation (and re-labelling by dropping the primes) gives the Navier-Stokes equations in a non-dimensional form

$$Re \left(\frac{\partial \mathbf{u}}{\partial t} + \mathbf{u} \cdot \nabla \mathbf{u} \right) = -\nabla P + \nabla^2 \mathbf{u} + \frac{Re \cdot \mathbf{b}}{Fr |\mathbf{b}|} \quad (4.7)$$

where Re is the Reynolds number of the flow and is defined as:

$$Re = \frac{UL}{\nu} \quad (4.8)$$

where $\nu = \mu/\rho$ is the kinematic viscosity. Fr is Froude number of the flow and defined

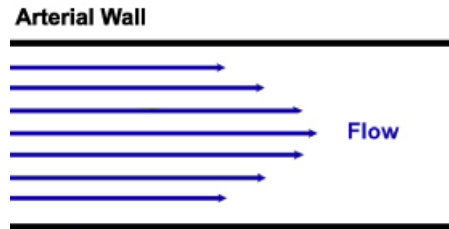


Figure 4.1: Poiseuille flow through an artery. The length of the arrows represent the magnitude of the velocity

as

$$Fr = \frac{U^2}{|\mathbf{b}|L} \quad (4.9)$$

The Reynolds number represents the ratio of convective forces to the viscous forces whereas the Froude number represents the magnitude of convective forces relative to the body forces. In this situation the model is to be constructed in the absence of any external body forces, so $\mathbf{b} = 0$. Notice that in the case where $Re \ll 1$ the equations simplify, to leave only a steady flow (as $Re \rightarrow 0$ the dynamic part of the model has a vanishing contribution). To find the Reynolds number in this specific case (at least to an order of magnitude) it is necessary to consider the nature of the flow in an artery.

4.2 Flow in an Artery

To estimate the Reynolds number U and L are required. L can be taken as the typical size of an EC. To estimate U the flow is modelled in a large artery using a very simple approach. Establishing the cylindrical coordinate system in figure 4.2 (with the z - axis in the direction of flow) leads to the deduction that the velocity of the flow must be a solution of the (dimensional) Navier-Stokes equation of the form:

$$\mathbf{u}(r) = V(r)\hat{\mathbf{z}} \quad (4.10)$$

where V is an arbitrary function of r satisfying $\mathbf{u} = \mathbf{0}$ on $r = a$, i.e. on the arterial walls. Note that \mathbf{u} satisfies the continuity equation. Substituting this into the Navier-Stokes

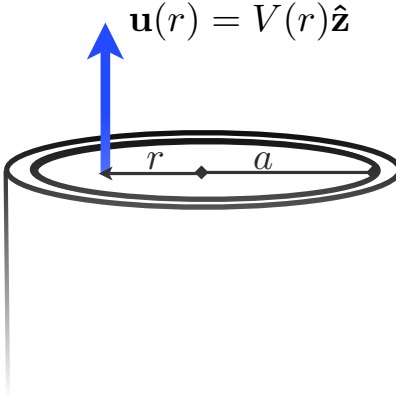


Figure 4.2: The flow through an artery represented as a cylinder. The large arrow represents the axially symmetric flow $\mathbf{u}(r)$ through a cylinder of radius a . The boundary condition is that $\mathbf{u} = 0$ on $r = a$.

equations (4.1), yields:

$$-\frac{\partial p}{\partial r} + \mu \frac{1}{r} \frac{\partial}{\partial r} \left(r \frac{\partial V}{\partial r} \right) = 0 \quad (4.11)$$

$$\frac{\partial p}{\partial y} = \frac{\partial p}{\partial z} = 0. \quad (4.12)$$

The second of these equations implies that $p = p(x)$, so equation (4.11) gives:

$$\frac{\partial p(x)}{\partial x} = \mu \frac{1}{r} \frac{\partial}{\partial r} \left(r \frac{\partial V}{\partial r} \right) \quad (4.13)$$

This has to hold for all r and z , and so implies that both sides are constant, which here is denoted by $-A$. Hence solving for the pressure and $V(r)$:

$$p = p_0 - Ar \quad (4.14)$$

$$V(r) = -\frac{A}{4\mu} r^2 + C \ln(r) + B. \quad (4.15)$$

Imposing the boundary condition that the solution is finite for all r and that V must vanish on the arterial wall gives $C = 0$ and $B = Aa^2/4\mu$, so that:

$$V(r) = \frac{A}{4\mu} (a^2 - r^2). \quad (4.16)$$

This expression defines what is usually known as Poiseuille flow, and is the solution to the flow in the cylinder, it has been widely used to model the flow in large arteries (Reese & Thompson, 1998; Bengtsson & Eden, 2003).

To estimate the characteristic flow U (in order to calculate the Reynolds number), it is necessary to determine the constant A . The most readily available experimental data in *in vivo* studies is the volumetric flow rate, Q , which is defined as the volume of fluid that passes through a particular area. The volume of fluid that travels through a small annulus perpendicular to the flow of width δr is $2\pi ur\delta r$. Integrating this expression between $r = 0$ and $r = a$ gives the volumetric flow rate through the cylinder:

$$Q = \frac{\pi A}{8\mu} a^4 \quad (4.17)$$

If the radius, a , is reduced by 5% then the volumetric flow rate is reduced by nearly 20%, because of the order four dependence on the radius, a . Hence this has physiological relevance in this case; an atherosclerotic plaque can have a large impact on the flow rate even if it only protrudes a little way into the artery, although in actuality this effect is reduced by distension of the artery (Arbel *et al.*, 2007).

The common carotid artery¹² (CCA) is taken as a physiological case in order to estimate U - although only an order of magnitude estimation is sought. The mean volumetric flow rate through the CCA has been estimated to be on average 6 ml s^{-1} (Marshall *et al.*, 2004) and the inner radius of the artery is estimated to be approximately 3 mm (Polak *et al.*, 1996). In large arteries blood is estimated to have a dynamic viscosity of 3.5 cP, (Kamm, 2002).¹³ If the density of blood is comparable to that of water then the kinematic viscosity is of the order of magnitude of $1 \text{ cm}^2 \text{ s}^{-1}$, or $10^8 \mu\text{m}^2 \text{ s}^{-1}$.

These values in equation (4.17) give A as $1900 \text{ dynes cm}^{-1}$, or 0.019 N cm^{-1} . Applying equation (4.16) with these parameters at a height characteristic of (to an order of magnitude) the height of an EC ($\approx 5 \mu\text{m}$), gives the magnitude of the velocity at $a - r = 1 \mu\text{m}$ as $280 \mu\text{m s}^{-1}$. This velocity defines the characteristic velocity, U , of the flow. The characteristic length, L , is defined by the size of the cell, here tens of μm . So $L.U$ is of the order of $3000 \mu\text{m}^2 \text{ s}^{-1}$. So the dimensionless Reynolds number is of the order of 10^{-5} .

Given that the Reynolds number is small the Navier-Stokes equations reduce to the

¹²The carotid arteries are responsible for the supply of blood to the brain and to the face. The onset of atherosclerosis in these arteries can limit supply of blood to the brain resulting in a stroke.

¹³a centi-poise, cP, has units dyne s cm^{-2} . One dyne is equal to 10^{-5} Newtons.

Stokes equation:

$$-\nabla P = \nabla^2 \mathbf{u} \quad (4.18)$$

This can be rewritten as:

$$\nabla \cdot \boldsymbol{\sigma} = 0 \quad (4.19)$$

where

$$\sigma_{ij} = -P\delta_{ij} + \mu \left(\frac{\partial u_i}{\partial x_j} + \frac{\partial u_j}{\partial x_i} \right) \quad (4.20)$$

is the stress tensor. Then $\mathbf{f} = \boldsymbol{\sigma} \cdot \mathbf{n}$ is the surface force where \mathbf{n} is the normal to the surface. The surface force \mathbf{f} has units of force per area, the total force, \mathbf{F} , on a closed surface S is

$$\mathbf{F} = \int_S \mathbf{f} \cdot d\mathbf{S} \quad (4.21)$$

4.3 The Boundary Integral Representation

In this chapter flow over a single cell attached to a planar surface is modelled. The previous section has justified the use of applying the Stokes, equation 4.19, to describe the flow over the cell. Of particular interest is the force on the cell surface because it is this that the cell somehow interprets and responds to.

The solution of equation 4.19 is restrained by the shape of the boundary of the problem (which is the cell and the planar surfaces), and specifically the value of the fluid on this boundary. A convenient way of incorporating the boundary value into the problem is by transforming equation 4.19 into an integral around over boundary. This transformation leads to the boundary integral representation (BIR).

Here equation 4.19 is applied in three dimensions. There are several motivations for this. In chapters 5 and 6 this model is coupled to models of diffusing proteins within the cell. Published observations of polarisation in ECs in response to fluid report distributions of proteins in 2D (for example the Rho GTPase Rac is activated in the downstream region). Hence it is advantageous to model these two dimensions. Additionally there is the third dimension (z -axis) which, although ECs are very thin, is important because it is in this dimension that the fluid flows over the cell. In the previous modelling of ECs as a viscous blob (section 2.2.1) it had to be assumed that the fluid flowed around the cell because the model was two dimensional. By modelling in 3D it is possible to calculate all three components of the force on the cell, and hence determine which of these the cell is likely to be responding to.

In physical terms the BIR expresses the total velocity as resulting from a distribution of point forces. These forces are weighted in such a manner as to ‘push’ the fluid in just the right way so that the Stokes equation (as well as its corresponding boundary conditions) are satisfied. To understand the method employed to solve the (BIR) it is instructive to see how it is derived. For a complete and excellent introduction to representing Stokes flow in this manner see Pozrikidis (1992); the derivation here follows similar logic.

The starting point is the Stokes equation for a point force

$$-\nabla P + \nabla^2 \mathbf{u} + \mathbf{g}\delta(\mathbf{x} - \mathbf{x}_0) = 0 \quad (4.22)$$

where \mathbf{g} is a constant, \mathbf{x}_0 is some point in the space, δ is the three dimensional delta function.

A delta function has the property that $\delta(\mathbf{x} - \mathbf{x}_0) = 0$ if $\mathbf{x} \neq \mathbf{x}_0$. If $\mathbf{x} = \mathbf{x}_0$ there is a singularity. Usefully, if $\phi(x)$ is any function (a test function) then

$$\int \phi(\mathbf{x}_0)\delta(\mathbf{x} - \mathbf{x}_0)d\mathbf{x}_0 = \phi(\mathbf{x}). \quad (4.23)$$

The standard approach for solving equations of this form (equation 4.22) is by introducing a Green’s function. A Green’s function is any function, \mathbf{G} , that is the solution to an equation of the form

$$L\mathbf{G}(\mathbf{x} - \mathbf{x}_0) = \delta(\mathbf{x} - \mathbf{x}_0) \quad (4.24)$$

where L is a linear operator acting on \mathbf{x} . Multiplying by a function $\phi(\mathbf{x}_0)$ and integrating on both sides gives

$$\int L\mathbf{G}(\mathbf{x} - \mathbf{x}_0)\phi(\mathbf{x}_0)d\mathbf{x}_0 = \int \delta(\mathbf{x} - \mathbf{x}_0)\phi(\mathbf{x}_0)d\mathbf{x}_0 \quad (4.25)$$

Applying equation 4.23 gives that the right hand side is equal to $\phi(\mathbf{x})$. Since L is linear and does not act on the integration variable, the expression can be rewritten as

$$Lf(\mathbf{x}) = \phi(\mathbf{x}) \quad (4.26)$$

where

$$f(\mathbf{x}) = \int \mathbf{G}(\mathbf{x} - \mathbf{x}_0)\phi(\mathbf{x}_0)d\mathbf{x}_0 \quad (4.27)$$

This expression is now an integral representation of the solution to $Lf(\mathbf{x}) = \phi(\mathbf{x})$, provided that \mathbf{G} is a solution for equation 4.24. A similar, although necessarily more

complicated approach, is followed to find the BIR of Stokes flow. To do so the solution of equation 4.22 is written as

$$u_i = \frac{1}{8\pi\mu} G_{ij}(\mathbf{x}, \mathbf{x}_0) g_j \quad (4.28)$$

Also the pressure and stress tensor can be represented similarly:

$$P(\mathbf{x}) = \frac{1}{8\pi} p_j(\mathbf{x}, \mathbf{x}_0) g_j \quad (4.29)$$

$$\sigma_{ik}(\mathbf{x}) = \frac{1}{8\pi} T_{ijk}(\mathbf{x}, \mathbf{x}_0) g_j \quad (4.30)$$

If \mathbf{u} and \mathbf{u}' are both solutions to (4.18) with associated stress tensors σ and σ' then the reciprocal identity is easily demonstrated

$$\nabla \cdot (\mathbf{u}' \cdot \sigma - \mathbf{u} \cdot \sigma') = 0 \quad (4.31)$$

Associating the flow \mathbf{u}' with a point force of strength \mathbf{g} at \mathbf{x}_0 , gives an analogous expression to (4.28), substitution (and rewriting in index notation) of this into (4.31) yields

$$\frac{\partial}{\partial x_k} [G_{ij}(\mathbf{x}, \mathbf{x}_0) \sigma_{ik}(\mathbf{x}) - \mu u_i(\mathbf{x}) T_{ijk}(\mathbf{x}, \mathbf{x}_0)] = 0 \quad (4.32)$$

Next this expression is integrated over a test volume V . Due to the singular nature of G_{ij} at $\mathbf{x} = \mathbf{x}_0$ it is important initially that \mathbf{x}_0 is outside V . Applying the divergence theorem¹⁴ over the volume V gives

$$\int_S [G_{ij}(\mathbf{x}, \mathbf{x}_0) \sigma_{ik}(\mathbf{x}) - \mu u_i(\mathbf{x}) T_{ijk}(\mathbf{x}, \mathbf{x}_0)] n_k(\mathbf{x}) dS(\mathbf{x}) = 0 \quad (4.34)$$

However if the flow inside V is to be found the integration has to be calculated with \mathbf{x}_0 in V . Proceed by selecting \mathbf{x}_0 as the centre of a small sphere V_ϵ , where V_ϵ is in the interior of the volume V (bounded by S). The integration is carried out over the volume V but excluding V_ϵ , hence the singularity at $\mathbf{x} = \mathbf{x}_0$ is avoided. The integral over the whole volume V is calculated as the integral over $V - V_\epsilon$ in the limit $\epsilon \rightarrow 0$, it will be demonstrated that this integral converges, despite the singularity.

¹⁴

$$\int_V \nabla \cdot \mathbf{F} dV = \int_S \mathbf{F} \cdot \mathbf{n} dS \quad (4.33)$$

where \mathbf{F} is any function, S is the surface that encloses the volume V and \mathbf{n} is the normal to this surface.

Integrating (4.32) over $V - V_\epsilon$ gives:

$$\begin{aligned} & \int_V [G_{ij}(\mathbf{x}, \mathbf{x}_0)\sigma_{ik}(\mathbf{x}) - \mu u_i(\mathbf{x})T_{ijk}(\mathbf{x}, \mathbf{x}_0)]n_k(\mathbf{x})dS(\mathbf{x}) = \\ & - \int_{V_\epsilon} [G_{ij}(\mathbf{x}, \mathbf{x}_0)\sigma_{ik}(\mathbf{x}) - \mu u_i(\mathbf{x})T_{ijk}(\mathbf{x}, \mathbf{x}_0)]n_k(\mathbf{x})dS(\mathbf{x}) \end{aligned} \quad (4.35)$$

As $\mathbf{x} \rightarrow \mathbf{x}_0$

$$G_{ij}(\mathbf{x} - \mathbf{x}_0) \rightarrow \frac{\delta_{ij}}{\epsilon} + \frac{\hat{x}_i\hat{x}_j}{\epsilon^3} \quad (4.36)$$

where $\hat{\mathbf{x}} = \mathbf{x} - \mathbf{x}_0$ and $\epsilon = |\mathbf{x} - \mathbf{x}_0|$ (Pozrikidis, 1992). This is the free space Green's function. Its associated stress tensor is given by

$$T_{ijk} = -6\frac{\hat{x}_i\hat{x}_j\hat{x}_k}{\epsilon^5} \quad (4.37)$$

On the boundary S_ϵ , $\hat{\mathbf{n}} = \hat{\mathbf{x}}/\epsilon$ and the surface element $dS = \epsilon^2 d\Omega$ where $d\Omega$ is the solid angle. Substituting all these expression into the right hand side of (4.35) gives

$$\begin{aligned} & \int_S [G_{ij}(\mathbf{x}, \mathbf{x}_0)\sigma_{ik}(\mathbf{x}) - \mu u_i(\mathbf{x})T_{ijk}(\mathbf{x}, \mathbf{x}_0)]n_k(\mathbf{x})dS(\mathbf{x}) = \\ & - \int_{S_\epsilon} \left[\left(\delta_{ij} + \frac{\hat{x}_i\hat{x}_j}{\epsilon^2} \right) \sigma_{ik}(\mathbf{x}) + 6\mu u_i(\mathbf{x}) \frac{\hat{x}_i\hat{x}_j\hat{x}_k}{\epsilon^4} \right] \hat{x}_k d\Omega \end{aligned} \quad (4.38)$$

In the limit $\epsilon \rightarrow 0$ the stress term vanishes because

$$\left(\delta_{ij} + \frac{\hat{x}_i\hat{x}_j}{\epsilon^2} \right) \hat{x}_k \quad (4.39)$$

is $O(\epsilon)$, but the velocity term tends to a constant value. So the integral on the right hand side becomes

$$-\frac{6u_i(\mathbf{x}_0)\mu}{\epsilon^4} \int_{S_\epsilon} \hat{x}_i\hat{x}_j dS(\mathbf{x}) \quad (4.40)$$

The integral is then:

$$\begin{aligned} \int_{S_\epsilon} \hat{x}_i\hat{x}_j dS(\mathbf{x}) &= \epsilon \int_{S_\epsilon} \hat{x}_i n_j dS(\mathbf{x}) \\ &= \epsilon \int_{V_\epsilon} \frac{\partial \hat{x}_i}{\partial \hat{x}_i} dV = \delta_{ij} \frac{4}{3} \pi \epsilon^4 \end{aligned} \quad (4.41)$$

Substituting this, and $\mathbf{f} = \boldsymbol{\sigma} \cdot \mathbf{n}$, into (4.38) gives the BIR¹⁵

$$\begin{aligned} u_j(\mathbf{x}_0) &= -\frac{1}{8\pi\mu} \int_S f_i(\mathbf{x}) G_{ij}(\mathbf{x}, \mathbf{x}_0) dS(\mathbf{x}) \\ &+ \frac{1}{8\pi} \int_S u_i(\mathbf{x}) T_{ijk}(\mathbf{x}, \mathbf{x}_0) n_k(\mathbf{x}) dS(\mathbf{x}) \end{aligned} \quad (4.42)$$

This equation is valid for \mathbf{x}_0 contained within V . Outside of V equation 4.34 holds. The limiting case of \mathbf{x}_0 being on the surface S is

$$\begin{aligned} u_j(\mathbf{x}_0) &= -\frac{1}{4\pi\mu} \int_S f_i(\mathbf{x}) G_{ij}(\mathbf{x}, \mathbf{x}_0) dS(\mathbf{x}) \\ &+ \frac{1}{4\pi} \int_S u_i(\mathbf{x}) T_{ijk}(\mathbf{x}, \mathbf{x}_0) n_k(\mathbf{x}) dS(\mathbf{x}) \end{aligned} \quad (4.43)$$

where the second integral is improper, so the principle value is taken (Pozrikidis, 1992).

Here the flow over a single cell is modelled. This cell is assumed attached to a planar surface S (which physically might represent the extra-cellular matrix, ECM). As noted above, Stokes flow over a planar wall with protuberances has been extensively studied, and the representation that will be derived (equation 4.48) is widely applied (Higdon, 1985; Pozrikidis, 1992; Zhou & Pozrikidis, 1995; Wang & Dimitrakopoulos, 2006a,b; Hazel & Pedley, 2000). However it is still useful to illustrate the derivation of the representation (equation 4.48). It is hoped this shall elucidate the solution method, section 4.4.

The perturbation in the flow due to a cell, \mathbf{u}^P , is defined as $\mathbf{u} - \mathbf{u}^\infty$. In this context equation 4.42 can be simplified by use of a Green's function that vanishes on the planar surface S . If the surface of the cell is denoted P then

$$\begin{aligned} u_j(\mathbf{x}_0) &= -\frac{1}{8\pi\mu} \int_{S,P} f_i(\mathbf{x}) G_{ij}(\mathbf{x}, \mathbf{x}_0) dS(\mathbf{x}) \\ &+ \frac{1}{8\pi} \int_{S,P} u_i(\mathbf{x}) T_{ijk}(\mathbf{x}, \mathbf{x}_0) n_k(\mathbf{x}) dS(\mathbf{x}) \end{aligned} \quad (4.44)$$

where \mathbf{x}_0 is in the interior of a volume V taken to be bounded by S and P and a surface closing V that can, for closure, be expanded to infinity, the integrals at infinity are then assumed not to contribute to the solution near P . The boundary condition is that $\mathbf{u} = 0$ on both S and P , which implies $\mathbf{u}^P = -\mathbf{u}^\infty$ on P and on S $\mathbf{u}^P = \mathbf{u}^\infty = 0$ substituting

¹⁵In these expressions \mathbf{n} is orientated into the flow.

these boundary conditions to equation 4.42 applied to the flow \mathbf{u}^P gives

$$\begin{aligned} u_j^P(\mathbf{x}_0) &= -\frac{1}{8\pi\mu} \int_{S,P} f_i^P(\mathbf{x}) G_{ij}(\mathbf{x}, \mathbf{x}_0) dS(\mathbf{x}) \\ &\quad - \frac{1}{8\pi} \int_P u_i^\infty(\mathbf{x}) T_{ijk}(\mathbf{x}, \mathbf{x}_0) n_k(\mathbf{x}) dS(\mathbf{x}) \end{aligned} \quad (4.45)$$

Next apply equation 4.34 for the unperturbed flow \mathbf{u}^∞ . However recall equation 4.34 is only valid for \mathbf{x}_0 situated outside a closed surface, so here it is applied over a volume enclosed by the surface P combined with the area C of the planar surface S covered by the cell, i.e. taking \mathbf{x}_0 as within the cell interior (recall this expression is being applied for \mathbf{u}^∞). \mathbf{x}_0 has to be outside this region to apply equation 4.34, hence it is consistent to take $\mathbf{x}_0 \in V$. Noting again that $\mathbf{u}^\infty = 0$ on S gives

$$\begin{aligned} &\mu \int_P u_i^\infty(\mathbf{x}) T_{ijk}(\mathbf{x}, \mathbf{x}_0) n_k(\mathbf{x}) dS(\mathbf{x}) \\ &= \int_{C,P} f_i^\infty(\mathbf{x}) G_{ij}(\mathbf{x}, \mathbf{x}_0) dS(\mathbf{x}). \end{aligned}$$

Using this expression to eliminate the second integral in expression 4.45, and adding \mathbf{u}^∞ gives

$$\begin{aligned} u_j(\mathbf{x}_0) &= u_j^\infty(\mathbf{x}_0) - \frac{1}{8\pi\mu} \int_S f_i^P(\mathbf{x}) G_{ij}(\mathbf{x}, \mathbf{x}_0) dS(\mathbf{x}) \\ &\quad - \frac{1}{8\pi\mu} \int_P f_i(\mathbf{x}) G_{ij}(\mathbf{x}, \mathbf{x}_0) dS(\mathbf{x}) \\ &\quad + \frac{1}{8\pi\mu} \int_C f_i^\infty(\mathbf{x}) G_{ij}(\mathbf{x}, \mathbf{x}_0) dS(\mathbf{x}) \end{aligned} \quad (4.46)$$

Now if a Green's function is chosen such that $G_{ij}(\mathbf{x}, \mathbf{x}_0) = 0$ if \mathbf{x} is on the planar wall S then all but the middle integral vanishes. Here the planar surface is taken as $z = 0$ then, such a choice for G_{ij} , Blake (1971), is

$$G_{ij}(\mathbf{x}, \mathbf{x}_0) = \xi_{ij}(\hat{\mathbf{x}}) - \xi_{ij}(\hat{\mathbf{X}}) + 2z_0^2 G_{ij}^D(\hat{\mathbf{X}}) - 2z_0 G_{ij}^{SD}(\hat{\mathbf{X}}) \quad (4.47)$$

where $\mathbf{x}_0 = (x_0, y_0, z_0)$, $\hat{\mathbf{x}} = \mathbf{x} - \mathbf{x}_0$, $\hat{\mathbf{X}} = \mathbf{x} - \mathbf{x}_0'$ and $\mathbf{x}_0' = (x_0, y_0, -z_0)$

$$\begin{aligned} \xi_{ij}(\hat{\mathbf{x}}) &= \frac{\delta_{ij}}{|\hat{\mathbf{x}}|} + \frac{\hat{x}_i \hat{x}_j}{|\hat{\mathbf{x}}|^3} \\ G_{ij}^D(\mathbf{x}) &= \pm \left(\frac{\delta_{ij}}{|\mathbf{x}|^3} - 3 \frac{x_i x_j}{|\mathbf{x}|^5} \right) \end{aligned}$$

$$G_{ij}^{SD}(\mathbf{x}) = x_2 G_{ij}^D(\mathbf{x}) \pm \frac{\delta_{j2} x_i - \delta_{i2}}{|\mathbf{x}|^3}$$

where x_2 is the z-component of $\mathbf{x} = (x_0, x_1, x_2)$.

Use of this Green's function in this context leaves the simplified representation of the flow as

$$u_j(\mathbf{x}_0) = u_j^\infty - \frac{1}{8\pi\mu} \int_P f_i(\mathbf{x}) G_{ij}(\mathbf{x}, \mathbf{x}_0) dS(\mathbf{x}). \quad (4.48)$$

In contrast to equation 4.42 this expression is valid for \mathbf{x}_0 on P as well as the whole region (Pozrikidis, 1992; Hazel & Pedley, 2000).

The interpretation of this representation is that $\mathbf{f}(\mathbf{x})$ is the force on the cell at \mathbf{x} , so that $-\mathbf{f}$ is the force that the surface at \mathbf{x} exerts on the fluid, hence a sum (the integral) over the surface gives the total force the surface exerts on the fluid. It is this force that pushes the fluid over the surface. Equation 4.42 completely determines the flow. The numerical solution of this equation is non-trivial and is the subject of the next section.

4.4 Solution Strategy

To calculate the flow at $\mathbf{u}(\mathbf{x}_0)$ it is necessary to find the force on the cell surface \mathbf{f} , which is of particular interest in the context of the EC response to fluid flow. To find \mathbf{f} in arbitrary geometries it is necessary to discretise the boundary integral representation, equation 4.48, although for simple geometries analytical solutions can be found (Hazel & Pedley, 2000). To proceed the surface P is discretised into surface elements. \mathbf{f} could be expressed on a surface element by linear or quadratic interpolation, however here - for expediency- a simpler option is chosen; namely that \mathbf{f} is taken to be constant over each surface element. To find \mathbf{f} equation 4.48 is discretised for \mathbf{x}_0 on P , because $\mathbf{u} = 0$ holds *a priori* on P . This leads to the discretised version of equation 4.48:

$$8\mu\pi u_j^\infty(\mathbf{x}_0) = \sum_{l=0}^n \int_l f_i^l(\mathbf{x}) G_{ij}(\mathbf{x}, \mathbf{x}_0) dS^l(\mathbf{x}) \quad (4.49)$$

where the surface is discretised into n surface elements. The integral, force and surface differential over the l th surface element are \int_l , \mathbf{f}^l and $dS^l(\mathbf{x})$ respectively. Since \mathbf{f}^l takes a constant value over each element the discretisation becomes

$$8\mu\pi u_j^\infty(\mathbf{x}_0) = \sum_{l=0}^{n-1} f_i^l(\mathbf{x}) \int_l G_{ij}(\mathbf{x}, \mathbf{x}_0) dS^l(\mathbf{x}) \quad (4.50)$$

Hence this equation (which is actually three equations for $j = 0, 1, 2$ corresponding to the x , y and z directions) is made of $3n$ unknown constants¹⁶: the $f_i^l(\mathbf{x})$. In order to solve for the f_i^l , equation 4.50 is applied with \mathbf{x}_0 taken at n different locations, called collocation points. This forms a $3n \times 3n$ linear system

$$8\mu\pi\bar{u} = \mathbf{G}\bar{f} \quad (4.51)$$

where

$$\bar{u} = \left[u_0^\infty(\mathbf{x}_0^0), \dots, u_0^\infty(\mathbf{x}_0^{n-1}), u_1^\infty(\mathbf{x}_0^0), \dots, u_1^\infty(\mathbf{x}_0^{n-1}), u_2^\infty(\mathbf{x}_0^0), \dots, u_2^\infty(\mathbf{x}_0^{n-1}) \right]^T \quad (4.52)$$

$u_j^\infty(\mathbf{x}_0^k)$ being the j th component of the velocity at \mathbf{x}_0^k , the k th collocation point. Similarly

$$\bar{f} = [f_0^0, \dots, f_0^{n-1}, f_1^0, \dots, f_1^{n-1}, f_2^0, \dots, f_2^{n-1}]^T \quad (4.53)$$

where f_j^m is the j th component of the force at the m th surface element. The last component, \mathbf{G} , is given as

$$\mathbf{G} = \begin{pmatrix} A_{0,0}^{0,0} & A_{0,0}^{1,0} & A_{0,0}^{2,0} & \dots & A_{2,0}^{n-3,0} & A_{2,0}^{n-2,0} & A_{2,0}^{n-1,0} \\ A_{0,0}^{0,1} & A_{0,0}^{1,1} & A_{0,0}^{2,1} & \dots & A_{2,0}^{n-3,1} & A_{2,0}^{n-2,1} & A_{2,0}^{n-1,1} \\ A_{0,0}^{0,2} & A_{1,0}^{1,2} & A_{2,0}^{2,2} & \dots & A_{2,0}^{n-3,2} & A_{2,0}^{n-2,2} & A_{2,0}^{n-1,2} \\ \vdots & \vdots & \vdots & \vdots & \vdots & \vdots & \vdots \\ A_{0,2}^{0,n-1} & A_{0,2}^{1,n-1} & A_{0,2}^{2,n-1} & \dots & A_{2,2}^{n-3,n-1} & A_{2,2}^{n-2,n-1} & A_{2,2}^{n-1,n-1} \end{pmatrix} \quad (4.54)$$

where

$$A_{i,j}^{k,m} = \int_k G_{ij}(\mathbf{x}, \mathbf{x}_0^m) dS^k(\mathbf{x}) \quad (4.55)$$

The indices are related by $i = k \bmod n$ and $j = m \bmod n$. Hence the problem of finding the force on the cell surface, \bar{f} , has been reduced to populating the matrix \mathbf{G} - which is known, and solving the linear system, equation 4.54. Once the vector \bar{f} is known the flow can be calculated at any point using equation 4.48.

¹⁶ i runs from one to three, and l from 0 to n .

4.5 Numerical Implementation of the Boundary Integral Representation

One of the difficulties in applying the BIR is approximating the integrals on the surface. The method of collocation points presents a difficulty because of the singular nature of the Green's functions. This section describes the numerical implementation applied to solve the BIR.

4.5.1 Discretising the surface

To implement the discrete version of the BIR, equation 4.50, it is necessary to split the cell surface into discrete elements. However, it will be reported (chapters 5 and 6) how this model is linked to reaction diffusion equations representing a - small - component of the signalling network that mediates EC polarisation and elongation. The equations in chapters 5 and 6 are implemented on a 2D projection (onto $z = 0$) of the cell surface. Hence to numerically solve these reaction diffusion equations the projection of the cell (onto $z = 0$) is discretised into regular hexagons. In chapter 5 this flow model is linked to these equations. Hence it is advantageous to have a mapping between the surface elements of the flow model and the discrete hexagons of the reaction diffusion model. To do so the following meshing algorithm (figure 4.3) is applied:

1. Discretise the planar surface with hexagons of side length L
2. Split each hexagon into four triangles, which will form the surface elements
3. Assign a height, H , to each hexagon according to $H = g(x_c, y_c)$, where (x_c, y_c) is at the centre of the hexagon.
4. Assign a height to each vertex as an average of the three surrounding hexagons' height.
5. The height of vertices at the periphery of the cell is then set to zero.

The last step ensures that the virtual cell touches the plane. Also note that, for the correct choices of g , this method also ensures that none of the surface elements lie entirely on $z = 0$, for if they do the integrals $A_{i,j}^{k,m}$ vanish when either k or m indexes to this element. This introduces degeneracy into the linear system which means \mathbf{G} is not invertible, and hence no solution would be found. It should be noted that this is not a

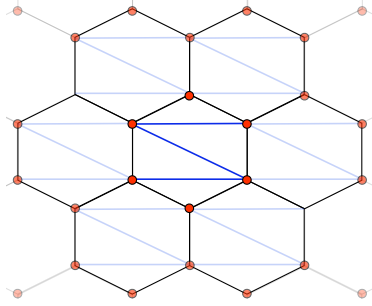


Figure 4.3: The plane is discretised into regular hexagons (for later solution of reaction diffusion equations) then each hexagon split into four triangles (these form the surface elements). The hexagons are then assigned a height, by mapping them to a predetermined surface. The height of the vertices, small circles, is taken as an average of the three surrounding hexagons.

numerically optimal meshing of the surface, however it has the advantage of allowing a simple mapping to the projection and expediency.

The function $g(x,y)$ is taken to be an ellipsoidal surface, defined by

$$g(x,y) = \frac{N(R^2 - (ax^2 + by^2))}{R^2}$$

where R is a radius of a typical roughly circular endothelial cell and N is the maximum height of the cell. Initially a and b are taken to be 1, this generates the surface as the cap of a sphere (figure 4.4). Note that the number of surface elements is not predetermined at the start of the algorithm. The size of the linear problem is essentially determined by the area of a hexagon, which is itself proportional to L^2 - then the number of surface elements, n , is determined by how many hexagons fit into the cell projection. In figure 4.4 $L = 0.8\mu\text{m}$, which (for that choice of R) leads to $n = 2977$, hence \mathbf{G} is of size $3n \times 3n = 79762791$. So clearly computational cost is already an issue in both populating this matrix, and, more critically, in solving the linear problem.

4.5.2 Integrating over a Surface Element

For the calculation of equation 4.55 the next stage of the numerical method is to integrate over a surface element. Since, after the mapping to $g(x,y)$, all of the triangles are different sizes and shapes it is convenient to apply a change of variables to expression 4.55 so that the surface integral is over the standard triangles (figure 4.5). The change

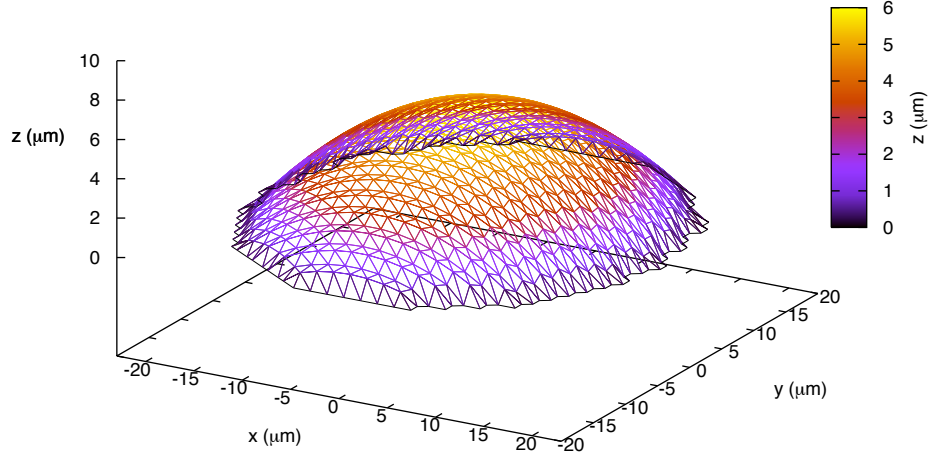


Figure 4.4: The virtual cell surface is discretised into triangles, according to the meshing algorithm. Maximum cell height, $N = 6 \mu\text{m}$. Cell radius, $R = 20 \mu\text{m}$. Hexagon side length $L = 0.8 \mu\text{m}$

of variables leads to

$$A_{i,j}^{k,m} = \iint \mathbf{J}^m G_{ij}^k(\eta, \xi) d\eta d\xi \quad (4.56)$$

where \mathbf{J}^m is the Jacobian of the transformation, which is dependent on which surface element has been transformed - indexed by m . The shift of the k index is to signify that the value of $G_{ij}^k(\eta, \xi)$ depends on the collocation point (indexed by k), however η and ξ are independent of the collocation point, \mathbf{x}_0 .

The variables η and ξ generate the original cartesian coordinates by

$$\underline{x}(\eta, \xi) = \underline{x}_1 + \eta(\underline{x}_2 - \underline{x}_1) + \xi(\underline{x}_3 - \underline{x}_1) \quad (4.57)$$

The Jacobian, \mathbf{J}^m of this transformation is given by

$$\begin{aligned} \mathbf{J}^m &= \left| \frac{d\mathbf{x}}{d\eta} \times \frac{d\mathbf{x}}{d\xi} \right| \\ &= |(\underline{x}_2 - \underline{x}_1) \times (\underline{x}_3 - \underline{x}_1)| \end{aligned} \quad (4.58)$$

Note that if the area of the surface element is A then $A = \mathbf{J}^m/2$.

To integrate over the triangle a numerical quadrature is used. Over a surface a quadra-

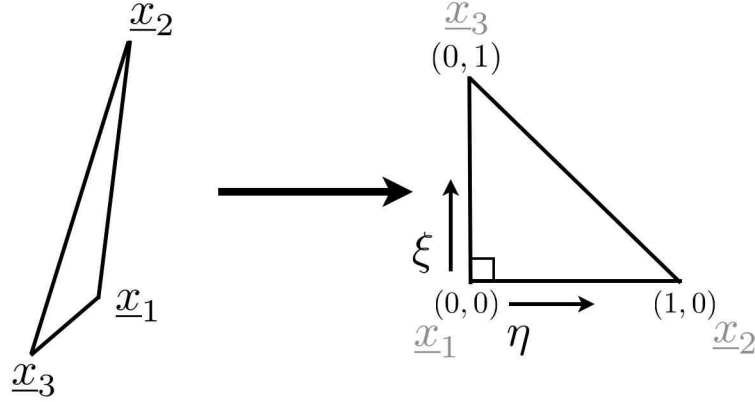


Figure 4.5: A surface element triangle (left) is mapped to the standard $(0,0)$, $(1,0)$, $(0,1)$ triangle (right) parametrised by η and ξ

ture is a set of points (q_η^i, q_ξ^i) and weights w^i that simplify the integral as

$$\int_m h(\eta, \xi) d\eta d\xi = \sum_i^N h(q_\eta^i, q_\xi^i) w_i \quad (4.59)$$

The weights are chosen so that the quadrature gives exact results for polynomials of a given order, generally more points mean the quadrature is precise for higher order polynomials and hence a better approximation to the integral. Here the quadrature taken is from Rathod *et al.* (2004), table 4.2.

q_η	q_ξ	w
0.112701665	0.100000000	0.068464377
0.112701665	0.443649167	0.109543004
0.112701665	0.787298334	0.068464377
0.500000000	0.056350832	0.061728395
0.500000000	0.250000000	0.098765432
0.500000000	0.443649167	0.061728395
0.887298334	0.012701665	0.008696116
0.887298334	0.056350832	0.013913785
0.887298334	0.100000000	0.008696116

Table 4.2: The quadrature used to integrate over non-singular triangles in the flow model.

The quadrature simplifies a surface integral into a sum of weighted function values. However, there is a complication. The singularity of $G_{ij}(\mathbf{x}, \mathbf{x}_0)$ occurs at $\mathbf{x} = \mathbf{x}_0$, so

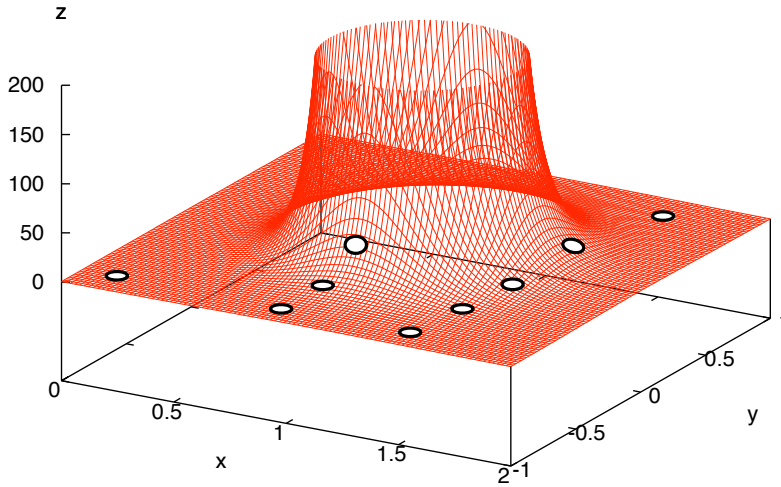


Figure 4.6: Plot of $1/r + x/r^3$, with $r^2 = (x - 1)^2 + y^2$ (this is one component of free-space Green's function for $\mathbf{x}_0 = (1, 0, 0)$). Note the singular behaviour when $\mathbf{x} \rightarrow \mathbf{x}_0$, similar behaviour occurs with this Green's function choice, equation 4.47. Note that for some choices of quadratures (white circles) the singular behaviour is not captured.

when the collocation point, \mathbf{x}_0 is on the same surface element as the integration in question there is a numerical problem, although the integral does converge as noted in the derivation of the BIR (section 4.3).

The difficulty comes in approximating this singularity. The quadrature is essentially a sampling of the function values over the surface element, which could either fail to capture the singularity or, if quadrature points fall on the singularity then no approximation to the integral can be given (figure 4.6). So an improvement to the quadrature method is needed. The obvious, and naïve, step to take to improve the integral over the singular triangle (meaning the triangle that contains the singular point) is to split it into smaller triangles, here six of them, then to map the smaller triangles onto the standard one and apply the quadrature over each of the smaller triangles. The integration over the surface element is then just the sum of the integrals over the smaller triangles (figure 4.7) and hence the integration accuracy is improved because the original triangle is being sampled by six times as many quadrature points.

This approach however still does not lead to the correct solution of equation 4.42 because the singularity is still not approximated correctly. The system of splitting the triangles could be continued, for example so the original triangle is split into 36 new

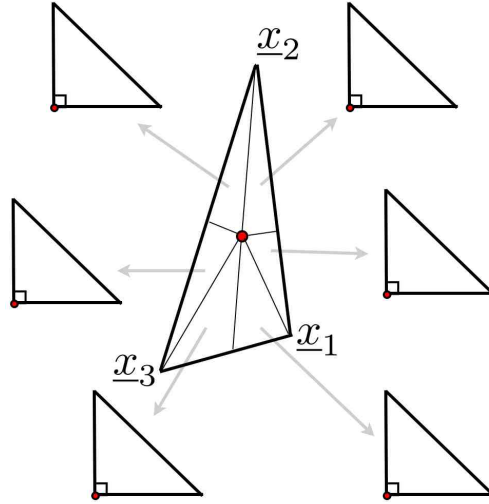


Figure 4.7: In the case of a singularity lying on the surface element (small dot) the triangle is split into six smaller ones, each of these mapped to a standard triangle. Note this mapping is done in such a manner to move the singularity to the right-angle point of the standard triangle.

triangles. Continuing this process would necessarily (slowly) converge to the true integral (the quadrature points never lie exactly on the singularity). However there is a more elegant suggestion by Pozrikidis (1992). Since the collocation points \mathbf{x}_0^k are taken to be the centre of the surface elements (in the notation of figure 4.5: $(\mathbf{x}_1 + \mathbf{x}_2 + \mathbf{x}_3)/3$ - this is a natural choice because as many collocation points as surface elements are required) the splitting of the triangle into six can always be arranged so the singularity is at the right angle point of the standard triangle, (figure 4.7). Because the singularity is at this point the following procedure regularises the integral.

If the integral

$$\int \int H(\eta, \xi) d\eta d\xi \quad (4.60)$$

is singular, then the change into polar variables

$$r = (\eta^2 + \xi^2)^{1/2}, \theta = \arccos(\eta/r) \quad (4.61)$$

has Jacobian r , so the integral becomes

$$\int \int rH(r, \theta) dr d\theta \quad (4.62)$$

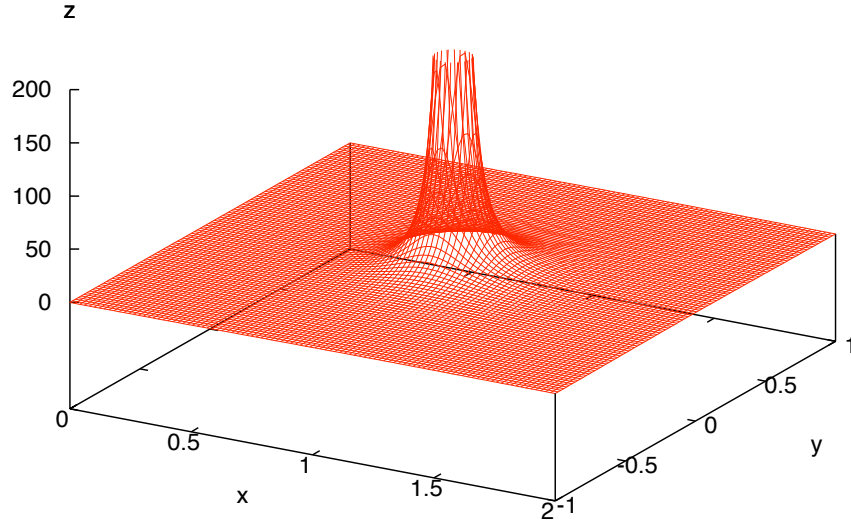


Figure 4.8: Plot of $1 + x/r^2$, with $r^2 = (x - 1)^2 + y^2$ - the regularised version of figure 4.6, note that the volume of the singularity is smaller in comparison to figure 4.6.

but since the singularity is at $r = 0$ the Jacobian has the effect of regularising the integral. This does not remove the singularity (figure 4.8) because the Green's function (equation 4.47) has poles of order greater than one, but it does reduce the order of the poles of the Green's function.

To calculate the regularised integral in the r and θ variables two line integrals are calculated. For these, quadratures on a line are needed (table 4.3). The values from table 4.3 are scaled by $\frac{\pi}{4}(1 + q)$ for integration in θ (so the range is scaled to $[0, \pi/2]$) and integration in r variable scaled by $(1 + q)/(2(\sin(\theta) + \cos(\theta)))$ (so the range is now $[0, 1/(\sin(\theta) + \cos(\theta))]$). The integral is calculated as

$$\int \int rH(r, \theta) dr d\theta = \sum_{q_r} \sum_{q_\theta} w_q w_r r H(q_r, q_\theta) \quad (4.63)$$

where q_θ and q_r are the scaled quadratures as above, with corresponding weights w_q and w_θ .

This approach successfully approximates the singularity to sufficient accuracy: the verification of this method (as a whole) is provided in section 4.6.

q	w
-0.989400934991650	0.027152459411754
-0.944575023073233	0.062253523938648
-0.865631202387832	0.095158511682493
-0.755404408355003	0.124628971255534
-0.617876244402644	0.149595988816577
-0.458016777657227	0.169156519395003
-0.281603550779259	0.182603415044924
-0.095012509837637	0.189450610455069
0.095012509837637	0.189450610455069
0.281603550779259	0.182603415044924
0.458016777657227	0.169156519395003
0.617876244402644	0.149595988816577
0.755404408355003	0.124628971255534
0.865631202387832	0.095158511682493
0.944575023073233	0.062253523938648
0.989400934991650	0.027152459411754

Table 4.3: The quadrature for integrating on the line $[-1,1]$, (Lowan *et al.*, 1942).

4.5.3 Solving the linear problem

Since the linear problem is so large an expedient solution method was sought. Iterative methods of inverting a matrix are much faster than direct methods, although fast methods designed for symmetric, or sparse systems will not apply here because the matrix is dense and not, in general, symmetric.

The method applied here is an iterative Krylov subspace method, the algorithm will be outlined briefly. For the details, the reader is referred to Saad (1981). The basic idea is to find a solution to a projection of the problem onto a Krylov subspace, which is defined as

$$K_m = \text{span}[r_0, Ar_0, \dots, A^{m-2}r_0, A^{m-1}r_0] \quad (4.64)$$

where the residue $r_0 = b - Ax^0$, x^0 is the initial guess to the linear problem $Ax = b$. Denote $V_m = [v_1, \dots, v_m]$ as the basis for K_m where the v_i are vectors - meaning that V_m is an $n \times m$ matrix.

Now if x^m is an approximate solution to the linear system such that $x^m \in K_m$ and $(Ax^m - b) \cdot v_j = 0$ for $j = 0, \dots, m$ then writing $x^m = V_m y^m$ implies that y^m satisfies the linear system

$$V_m^T A V_m y^m - V_m^T b = 0, \quad (4.65)$$

the advantage of this system is that it is of a reduced ($m \times m$) size. If the exact solution is related to the initial guess x_0 by $x = x^0 + z$, then $b - Az = r_0$ must hold. There are many different methods to generate the subspace V_m . Here the method of Arnoldi is taken, which creates an orthonormal basis of V_m by a Gram-Schmidt process, see (Saad, 1981):

- take $v_1 = r_0/|r_0|$
- then repeat until $k=m$:

$$v_{k+1,k} = (Av_k - \sum_{i=1}^k h_{ij}v_i)/h_{k+1,k} \quad (4.66)$$

where $h_{jk} = (Av_k, v_j)$ and $h_{k+1,k} = |v_{k+1,k}|$

Note that $V_m^T AV_m = H_m$ is a Hessenberg matrix¹⁷, with entries h_{ij} . The final solution is given by $x = x^0 + z$ where

$$z = |r_0|V_m H_m^{-1}(V_m^T v_1) \quad (4.67)$$

The advantage of this method is the computational gain coming from the Hessenberg matrix having a large number of zeros, making the matrix computationally cheap to invert - here by simple Gauss-Jordan elimination.

Further computational gain can be achieved using the method iteratively, essentially because m can be taken to be smaller and the equivalent accuracy gained by repeatedly running the algorithm. The iteration is simply that the solution x forms the new initial guess for the subsequent iteration, although if m is very much less than the size of the linear system then the iteration diverges. Figure 4.9 illustrates convergence in this case.

Using this method applied to the linear problem solves for the force on the cell at any point on the surface, $\mathbf{f}(x_0)$. This method is validated by ensuring it generates a sensible stream line pattern, checking that the shear stress on the cell is in the reported range and that as $\mu \rightarrow 0$ the solution also tends to zero.

¹⁷Meaning its only entries are the ones above the main diagonal, the ones in the main diagonal and the ones in the diagonal directly below the main diagonal

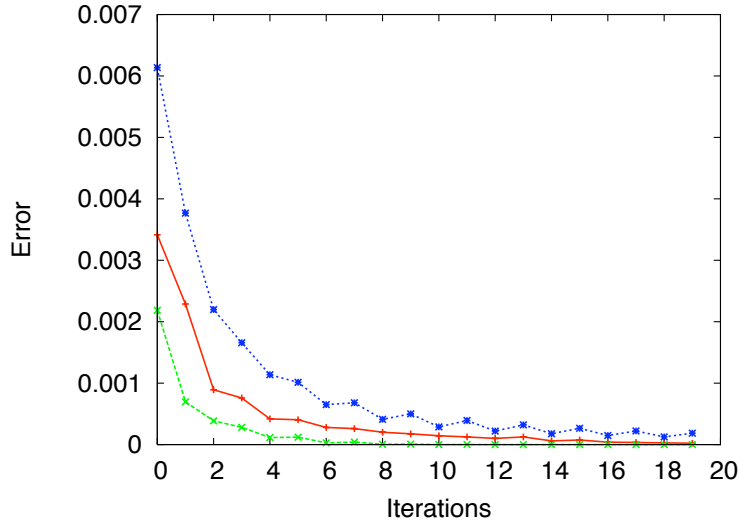


Figure 4.9: Examples of the iterative arnoldi process in terms of the error defined as $|Az - b|$, for a linear problem of size 300×300 . The solution is found by taking $m = 10$ (\times points), $m = 6$ ($+$ points) and $m = 4$ ($*$ points), with the 0th iteration being the first solution found from an initial guess of z having every entry as 1.

4.5.4 Flow Parameters

Near the endothelial cell wall the Poiseuille flow, equation 4.16, is well approximated by simple shear flow. To show this consider rewriting equation 4.16 in terms of the distance from the planar surface, z :

$$V(z) = \frac{A}{4\mu} (2a - z)z. \quad (4.68)$$

Differentiating 4.68 with respect to z gives

$$\frac{dV}{dz} = \frac{A}{2\mu} (a - z).$$

For the CCA, $a = 3000\mu\text{m}$ and at the EC z is of the order of $5\mu\text{m}$ so in this region equation 4.5.4 is well approximated by a constant value of $Aa/2\mu$, hence the far-flow field, \mathbf{u}^∞ , is taken as

$$\mathbf{u}^\infty(x, y, z) = (kz, 0, 0) \quad (4.69)$$

where $k = Aa/2\mu$ is the shear rate. The viscosity, μ , is taken as 1 cP. Evaluating k (with $A = 1900 \text{ dynes cm}^{-1}$ and $a = 0.3\text{cm}$) gives the shear rate as $k = 285\text{s}^{-1}$

4.6 Results - Flow over a single Cell

Equation 4.48 is solved for a single cell attached to the surface and in the process the force on the cell surface is found. The validity of the numerical method is verified by three methods. First by plotting both the maximum shear stress and the total shear stress against the value of μk , the viscosity μ times the shear rate k where the magnitude of shear stress, S , at \mathbf{x} is found by:

$$S = (f_i f_i - f_j n_j)^{1/2} \quad (4.70)$$

n_j is a vector normal to the surface orientated away from the cell, f_j is the surface force (or stress vector, recall $\mathbf{f} = \boldsymbol{\sigma} \cdot \mathbf{n}$).

If μk is constant then the solution will stay the same, even if μ and k vary. The linear system could be solved independently of μ and k and the final solution scaled by μk . Here the solution is solved including μ and k , hence there should be a linear relationship between μk and both the maximum shear stress and the total shear, the linear trend should of course pass through (0,0). This indeed is the case, as is evidenced in figures 4.10 and 4.11. In both these figures there are actually three trends for cells of different morphologies, which will be referred to in chapter 6. It will emerge that the similarity of these three trends has biological relevance.

The second, more visual, test of the solution method is checking that it correctly generates the streamline pattern expected. Streamlines are defined as a path \mathbf{x} parametrised by s such that

$$\frac{d\mathbf{x}}{ds} = \mathbf{u}(\mathbf{x}) \quad (4.71)$$

if $\mathbf{x} = (x_0, x_1, x_2)$ and $\mathbf{u} = (u_0, u_1, u_2)$ then

$$\frac{dx_0}{u_0} = \frac{dx_1}{u_1} = \frac{dx_2}{u_2} = ds \quad (4.72)$$

from which it is inferred that at any point the streamlines are parallel to the flow velocity.

As this is a steady flow the streamlines coincide with both the pathlines and streaklines.

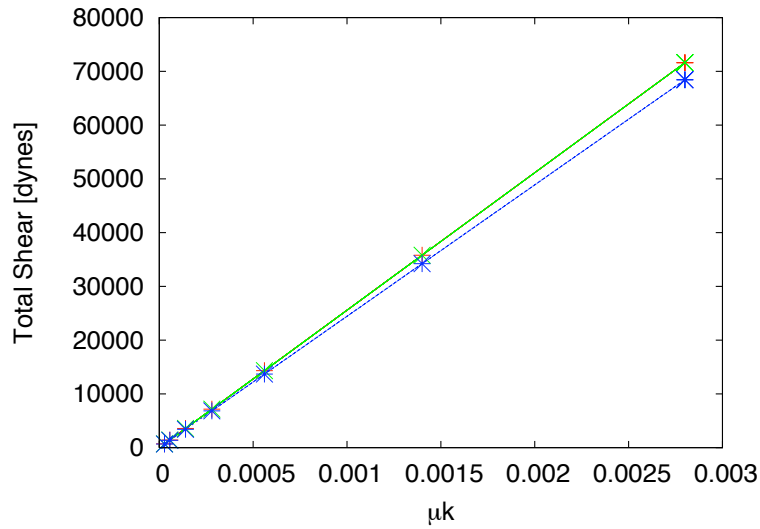


Figure 4.10: The total shear force on the cell as a function of μk for three different cell shapes; circular (red), and ellipsoids orientated parallel (green) and perpendicular (blue) to the flow (see section 6.3). The red and green trends are identical. μ has units of $g \mu m^{-1} s^{-1}$, and k s^{-1} . So μk is in units of $g \mu m^{-1} s^{-2}$.

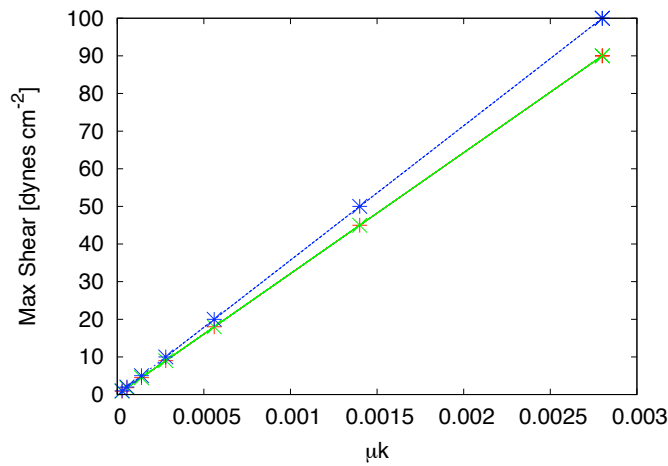


Figure 4.11: The maximum value of shear stress on the cell as a function of μk for three different cell shape; circular (red), and ellipsoids orientated parallel (green) and perpendicular (blue) to the flow (see section 6.3). The red and green trends are identical. μ has units of $g \mu m^{-1} s^{-1}$, and k s^{-1} . So μk is in units of $g \mu m^{-1} s^{-2}$.

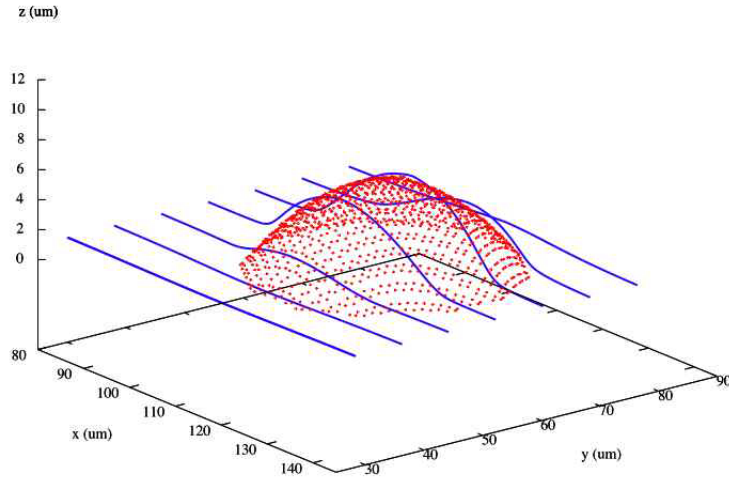


Figure 4.12: Streamlines taken at different starting points. The surface of the cell is shown by marking the collocation points as dots.

Physically these correspond to the path a particle or a portion of the fluid takes respectively.¹⁸ Equation 4.71 is integrated for different initial conditions with the results in figure 4.12. The streamlines are perturbed by the cell surface. Since the surface is symmetrical the fluid flow - evidenced by the streamlines - is also symmetrical. This is because Stokes flow is reversible: if \mathbf{u} is a solution then so is $-\mathbf{u}$ for the same boundary conditions. Since Stokes flow is steady, the flow at time t is the same as at all other times.

The third validation, is application of the method to a different geometry, a hemisphere. There is an analytical approximation to the solution for the total force on the hemisphere, $F_a = 4.30\pi$ (Price, 1985). The numerical solution linearly converges to the analytical solution as the side length, L , of the hexagons (which discretise the plane) approaches zero, figure 4.13. In solving for the fluid flow over an EC the ratio L/R (where $R = 20 \mu m$ is the radius of the area of the plane covered by the cell) is taken to be 0.04. In figure 4.13 this corresponds to an error of about 1.7%, however it is anticipated that the EC case is more accurate than the hemispherical case because of the discretisation method. The method applied here is to project a discretisation of the x-y plane onto a surface to generate a meshing of that surface. This method is suitable

¹⁸Usually visualised by dropping dye into the fluid.

for the EC case because they are relatively flat, however for a hemisphere the method coarsely meshes the regions near where the hemisphere joins the plane.

Figure 4.13 illustrates some anomalous data, where error increases, briefly, for a reduction in L . These anomalies occur where L/R is large (≈ 0.18 and ≈ 0.24). For L/R in this range the algorithm is desensitised to the value of L (decreasing L/R does not necessarily increase the number of surface elements because the meshing algorithm requires that only hexagons entirely contained within the prescribed area are mapped to the surface). With the error plotted against the number of surface elements (inset plot of figure 4.13) these anomalies appear attenuated. However the anomalies are still present. Since each meshing is not optimal it may be the case that errors cancel out for certain choices of L , it is evident that a given meshing's accuracy at approximating the solution depends on other factors other than simply L or the number of surface elements.

One possibility as a factor that may generate these anomalies is the orientation of elements; each meshing will generate a slightly different proportion of elements with a given normal vector and a given proportion may provide a better approximation to the solution than a meshing that has (slightly) more surface elements but in a different orientation. The difference in the orientation of elements will be greater between two meshings that have large L/R , this may generate the anomalies. The proportion of elements in any given orientation converges (because the surface meshing approaches the true geometry) to some value as $L \rightarrow 0$, hence the anomalies should also be smoothed out as $L \rightarrow 0$. It remains to be seen if this is the case, figure 4.13 illustrates that this effect, or something similar, may be occurring. Nevertheless, the numerical solution does converge to the analytical solution.

The process of EC polarisation and elongation is usually referred to as a shear stress activated process. So it is of immediate interest and relevance to describe the shear stress over the entirety of the cell (figure 4.14). Recall that the shear rate k is calculated from the Poiseuille flow which itself was parametrised using physiological observations. Hence figure 4.14 should give shear stresses in the range estimated physiologically, and as typically used in *in vitro* experiments (Fleming *et al.*, 2005; Jalali *et al.*, 1998; Wojciak-Stothard & Ridley, 2003; Goldfinger *et al.*, 2008; Tzima *et al.*, 2001, 2002). Typically these experiments are carried out with shear stresses of about 5 – 15 dynes

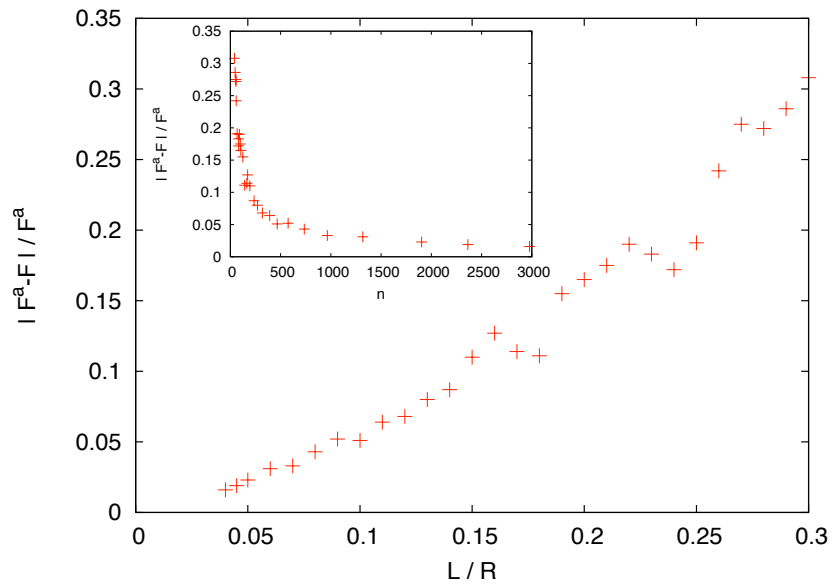


Figure 4.13: Convergence of the numerical method. Main plot: L is the length of the hexagons which discretise the plane, R is the radius of the area of the plane covered by the cell, F and $F^a = 4.30\pi$ (Price, 1985) are the total force on the hemisphere due to fluid flow (viscosity, $\mu = 1$ cP and shear rate $k = 1 \text{ s}^{-1}$) calculated numerically and analytically respectively. The absolute normalised error $|F^a - F|/F_a \rightarrow 0$ as $L/R \rightarrow 0$, with approximately linear dependence on L/R . Inset plot: Absolute normalised error $|F^a - F|/F_a$ plotted against the number of surface elements, n .

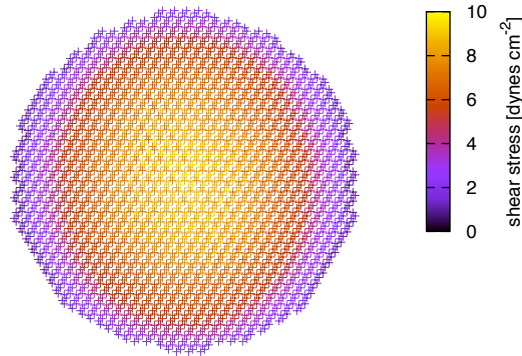


Figure 4.14: The shear stress on the endothelial cell for a shear rate $k=280\text{ s}^{-1}$. The maximum shear stress is 10 dynes cm^{-2} , typical of the value used in *in vitro* experiments. Note the symmetry between the downstream and upstream parts of the cell. The flow is left to right.

cm^{-2} . Generally these are calculated as the wall shear stress

$$\tau_w = \mu \left. \frac{\partial u}{\partial z} \right|_{z=0} \quad (4.73)$$

where u is the flow speed along the boundary at $z = 0$. The exact expression for τ_w depends on the geometry of the flow boundaries. For the Poiseuille flow in the cylinder (expression 4.16) the wall shear stress solves to be

$$\tau_w = \mu \frac{4Q}{a^3\pi} \quad (4.74)$$

with Q and a defined as the flow rate and vessel (or cylinder) radius respectively. With the parameters taken as before ($Q = 6\text{ ml s}^{-1}$ and $a = 3\text{ mm}$) the wall shear stress $\tau_w = 6.2\text{ dynes cm}^{-2}$, which is comparable to the more detailed map of shear stress over an EC in figure 4.14. $\tau_w = 6.2\text{ dynes cm}^{-2}$ is also comparable to the typical values used in *in vitro* experiments.

Figure 4.14 is of biological relevance, in particular in light of the comments made about spatial heterogeneity in signalling (section 1.1.1): it is clear that the shear stress can not be the progenitor of the heterogeneity. This does not rule it out as having an important role in signalling, but it would appear (due to up/downstream symmetry) that this signalling can not be localised to the downstream edge. Other possibilities could occur, for example cytoskeleton components could be linked to the cell surface creating

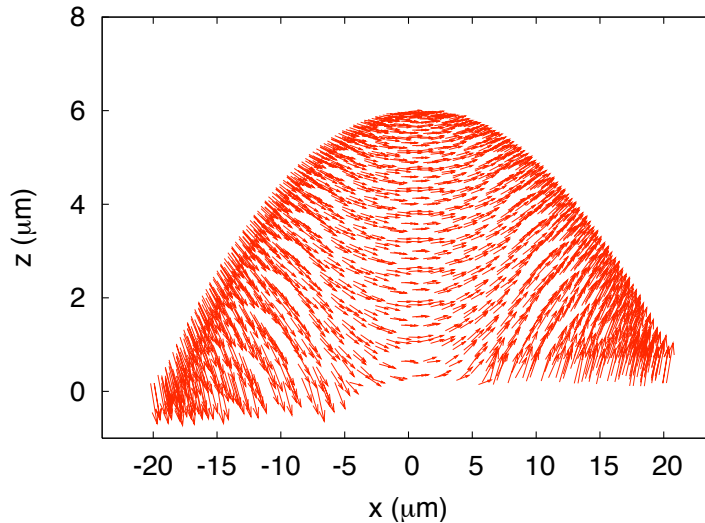


Figure 4.15: Unit force, \hat{f} (projected onto the z-x plane), on the surface of the cell (as in figures 4.4 and 4.14) due to laminar fluid flow (left to right). Note that the upstream edge of the cell is in compression and the downstream edge is under tension.

the heterogeneity from being in a pre-orientated state. The discussion on mechano-transduction will be extended in chapter 5.

If shear stress is not a candidate for introducing the spatial heterogeneity in signalling, then it must be the component of force normal to the surface. That this could be the case can be observed in figure 4.15, where the cell is viewed from the side. Here the downstream edge of the cell is under tension and the upstream edge in compression. Hence a mechano-transducer that can respond to being stretched (or the reverse) could interpret this force on the cell.

Figure 4.16 is a different projection of the unit force than figure 4.15, in this case the force on cell surface is projected to the x-y plane. In the case of figure 4.16 if cytoskeleton elements (or ion channels) are pre-orientated (for example from the nucleus out) then in principle the flow direction could be interpreted, however here the tension and compression argument is favoured.

This model has illustrated that the likely source of localised signalling is response, in some manner, to the normal force on the cell surface. This is in contrast to the usual paradigm of EC polarisation and elongation being a shear stress activated process, It is not argued that a signalling response to shear stress is not necessary but rather that

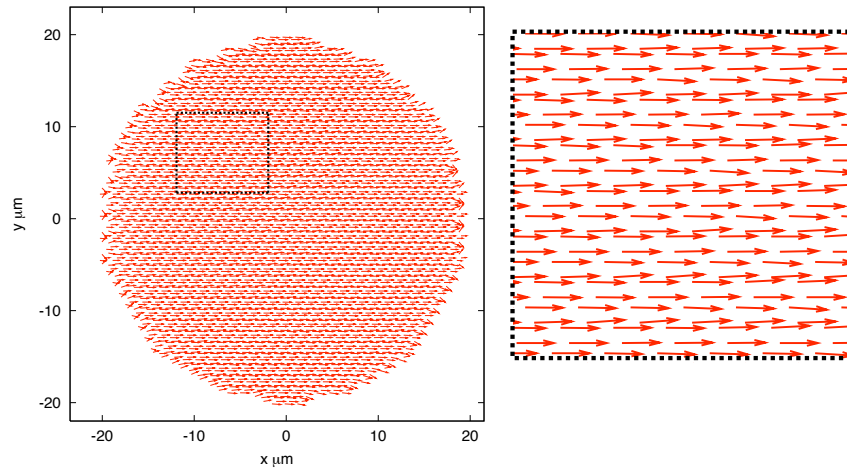


Figure 4.16: Left: Projection on to the x-y plane of unit force, \hat{f} , on the surface of the cell (as in figures 4.4 and 4.14) due to laminar fluid flow (left to right) . Right: magnification of the projection of \hat{f} . Note this projection of \hat{f} is parallel to the direction of fluid flow (left to right).

the normal force initiates the polar response. Although that the normal force may play a role has been suggested previously (Wang & Dimitrakopoulos, 2006*a,b*), it is not widely considered. Is the normal force acting (directly or in-directly) onto a mechano-transducer a plausible hypothesis? This hypothesis is explored in the next chapter by modelling normal force induced mechanical transduction.

5 Modelling Endothelial Cell Mechano-transduction

In this section the flow model is coupled via a simple mechano-transducer model to a biochemical output. The widely proposed mechanisms that a cell could employ for conversion of a mechanical signal into a biochemical one are introduced. One such mechanism is hypothesised to account for the spatial heterogeneity in signalling. This mechano-transducer is modelled using a Kelvin-Body model and parameters derived to fit experimental data by Bausch *et al.* (1998).

These parameters were previously applied in a model of EC mechano-transduction by Mazzag *et al.* (2003) in modelling EC mechano-transduction. Their approach was to couple together spring-like models in series and in parallel representing structural cytoskeletal elements. Here a different approach is taken. It will be argued that the mechano-transducer is likely to be attached to the basal surface of the cell and that the force from the fluid is transmitted directly to this point.

The first novel contribution of this chapter is the direct linking of an explicit solution for the flow over an EC (chapter 4) to a (previously proposed) model of mechano-transduction. The second novel contribution is coupling this mechano-transduction model to a biochemical output with parameters fitted to match experimental data.

5.1 Candidate Mechano-transducers

There are two main mechanisms for mechano-transduction of force on a cell and it is likely they are both involved in initiating the signalling network that governs morphological change in ECs. The first is influx of ions through stretch-activated ion channels and the second is alteration of protein binding characteristics due to increased tension or compression. In the second case there are several different possible candidates.

In vivo ECs are covered with a thin ($0.5 \mu\text{m}$) layer of membrane bound molecules known as the glycocalyx. The structure of the glycocalyx and its linkage to the cytoskeleton may play a significant role in the EC response to fluid flow with consequences for either of the main mechanisms of mechano-transduction.

5.1.1 Ion Channels

Ion channels are multimeric protein assemblies that form selective pores through the cell membrane. Typically these pores are selective enough so as to only allow specific ions through. Importantly, ion channels can be gated so that they are only open in certain conditions. For example binding to specific ligands, due to an electrochemical potential across the cell membrane or stretch activation. The latter case is of particular relevance to this project. There are many examples of ion channels responding to fluid flow over a cell, leading to (depending on the type of ion channel) influx of K^+ , Cl^- , or Ca^{2+} (Hoger *et al.*, 2002; Yamamoto *et al.*, 2000; Gautam *et al.*, 2006).

There are three possible mechanisms for shear stress-induced ion channel activation, (Barakat *et al.*, 2006):

- The fluid exerts enough force on the ion channel to alter the structure of its constituent protein(s) in such a manner to open the channel.
- The flow alters membrane fluidity (the relative speed of diffusion on the membrane) which lowers membrane tension allowing the channel to open.
- Tethering of the channel to the cytoskeleton allows gating in response to cytoskeletal reorganisation.

Of these Barakat *et al.* (2006) argue that the flow can not impart enough force for the first mechanism to occur.

There is evidence that shear stress can indeed alter membrane fluidity (Butler *et al.*, 2001), although how this precisely relates to membrane tension is unclear. However, it is apparent that ion channels can become activated in response to changes in membrane tension (Martinac, 2004).

Tethering of ion channels to the cytoskeleton is a more likely candidate for channel activation. Hoger *et al.* (2002) report that disruption of the cytoskeleton inhibits current through channels. Furthermore, as discussed below, the glycocalyx (a layer of proteins on the membrane) screens the membrane, but not the cytoskeleton, from shear stress.

Ion channels are an elegant possibility as a mechano-transducers, regardless of the gating method, not least because the coupling of signals from different ion channels could be used to interpret different flow signals. For example K^+ and Cl^- channels are

fast and slow activating respectively, so a pulsatile flow (depending on its frequency) activates K^+ channels but not Cl^- channels, yet a steady flow activates both of these, (Barakat *et al.*, 2006). Hence in principle a cell can sense different types of flow.

Ion channels evidently play a signalling role in the response of ECs to fluid flow. However it is clear that they are not the simplest model to answer the questions raised in section 1.2 - in particular regarding the formation of local regions of activated proteins. Since these ion channels respond to forces parallel to the cell membrane and not normal to it (Martinac, 2004), and because of the upstream/downstream symmetry in the shear stress pattern (figure 4.14) it is difficult to imagine how ion channels could generate such a pattern if they themselves are not activated locally (the symmetric shear force suggests global activation of targets for a uniform channel distribution). Small ions could diffuse quickly throughout the cell, and it will be demonstrated (chapter 6) that, with this model, relatively slow diffusion is necessary to maintain this local zone of activity and although ions could be sequestered locally, this would require polarity to be established prior to ion-channel signalling.

The role of ion-channel activation can not be completely assigned to establishing global signalling properties. It is not clear if a cell could extract directional information from ion-channels activated by shear stress, but it is plausible that in response to fluid flow the distribution of ion-channels becomes non-uniform (either by re-organisation by the cell or as a direct result of the fluid flow) and this leads to a directional bias. In principle any directional information (even if it is highly transient) could create distinct zones of activation by a bi-stable mechanism, this has been established in models of migratory cells (Jilkine *et al.*, 2007), although generally models of this type require a specific balance of fast and slow diffusion for inhibitors and activators respectively.

5.1.2 Glycocalyx-Cytoskeleton transduction

The thin ($0.5\mu m$) glycocalyx is a complex mix of glycoproteins, glycosaminoglycans and proteoglycans as well as molecules bound from the flow itself (VanTeefelen *et al.*, 2007). Here the aspect of interest is the mechanical properties of the glycocalyx.

Models of the structure of the glycocalyx indicate that the flow within the glycocalyx layer (due to flow over the cell) is practically zero and hence the shear stress at the membrane is also zero (Weinbaum *et al.*, 2007). This is further evidence against stretch activated ion channels being gated by shear stress.

The glycocalyx and not the cell membrane therefore experiences the fluid flow (note that this does not alter the results of the fluid flow model, section 4.6 - the discretised surface just needs to be reinterpreted as the glycocalyx layer rather than the cell membrane). The glycocalyx transmits the force to the cytoskeleton via connections to the actin cortical cytoskeleton, a polygonal structure of actin filaments beneath the cell membrane (Weinbaum *et al.*, 2003).

This leads to one proposed mechanism of mechanotransduction (Thi *et al.*, 2004). Their hypothesis is that the components of the glycocalyx acts as rigid rods and transmit the force to the actin cortical cytoskeleton. In confluent layers of cells this leads to a bending moment across the cell and, for shear stresses above a certain threshold, breaking of cell-cell adhesions - leading to intra-cellular signalling. This model does not explain localised activation (the torque on the cytoskeleton should break cell-cell adhesions at both the upstream and downstream edges), nor indeed polarisation in non-confluent endothelial cells. However, recent work (Chiu *et al.*, 2008) has demonstrated that PECAM-1, a protein present in endothelial cell-cell adhesions, can act as a mechano-transducer, and in response to fluid flow does get activated (via tyrosine phosphorylation) in confluent layers of ECs (Tzima *et al.*, 2005). Goldfinger *et al.* (2008) attribute integrin activation in downstream regions to PECAM-1 activation.

5.1.3 Focal Adhesions as Signalling Centres

Given the results from the flow model (chapter 4) local activation and asymmetry in cell signalling appears to be due to the upstream and downstream edges of the cell being under compressive and tensile normal forces respectively. Hence the obvious mechanism to generate local, downstream, activation is using the signal from a mechano-transducer that can respond to this pattern.

The leading candidates for mechanotransduction via tension-induced conformational change are integrin complexes: protein assemblies that are (often) bound to the extra-cellular matrix (ECM) and are named after the trans-membrane heterodimers that bind to the ECM (figure 5.1). Following the onset of fluid flow these complexes must be under increased tensile force if the cell is to remain adhered to the ECM.

Integrins are composed of α and β units that each have extra-cellular, transmembrane and cytoplasmic regions (figure 5.1). The integrin family of distinct α and β sub-units allows sensing of the ECM via specific receptor binding, for example $\alpha_5\beta_1$ is the main

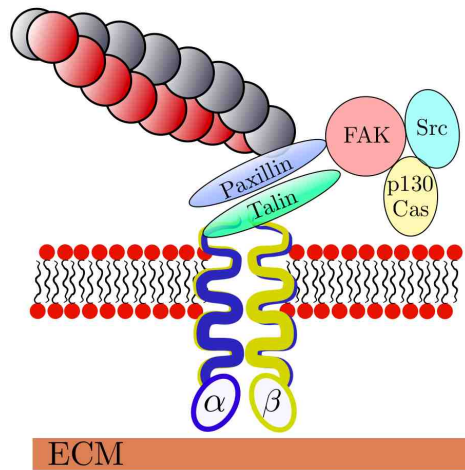


Figure 5.1: Cells adhere to the ECM via integrin binding. Integrins, composed of α and β sub-units, recruit other proteins including paxillin, talin, Src, FAK (focal adhesion kinase) and p130 Cas. The complex attaches to actin filaments. Bundling of these filaments leads to focal contacts which (in the right conditions, for example if they are under tension) mature into focal adhesions.

receptor for fibronectin (Geiger *et al.*, 2001).

Integrins cluster into focal complexes and then mature into focal adhesions (FA) which are adhesive centres of signalling and structural proteins. Typically FAs include α -actinin (for bundling of connected actin filaments, section 2.1.3.), talin, vinculin, Src, p130 Cas and FAK (figure 5.1). Talin and paxillin bind to integrins and mediate binding of vinculin and FAK to the complex (Sastry & Burridge, 2000).

It is believed that Rac induces focal contact formation in lamellipodia (Rottner *et al.*, 1999), however Rho (and acto-myosin tension) induces maturation into FA (Ridley & Hall, 1992). The role in mediating endothelial alignment of FAs and integrins is evidenced by both early remodelling and alignment of FAs in the direction of flow (Davies *et al.*, 1994).

Formation of FAs is force-dependent. However this force can be externally applied, so Rho induced acto-myosin contraction is not necessary for maturation of FAs. Interestingly, the force generated by an individual myosin II protein is ≈ 2 pN (Tyska *et al.*, 1999). The flow model predicts a surface force, $|\mathbf{f}|$, of the order of 10 dynes cm^{-2} , or 1 pN μm^{-2} . Hence it is conceivable that the force due to the fluid itself could instigate FA maturation directly, rather than an effector of the mechano-transducer inducing a

Rho dependent pathway.

FAs attach stress fibres to the basal surface of the cell (Pellegrin & Mellor, 2007). It was suggested in section 2.2.3 that formins may play an important role in nucleating directed polymerisation of actin and initiating stress fibre (and presumably, FA) alignment. Formins cap the barbed ends of actin filaments, however they still allow polymerisation at this point - for this reason they are referred to as a 'leaky cap' for the filament. It has been shown that application of a pN force on the filament via the 'leaky cap' increases the polymerisation rate of actin (Kozlov & Bershadsky, 2004) and that the formin mDia1 is sufficient (as oppose to pathways initiating acto-myosin contraction) for FA formation in the presence of external force (Riveline *et al.*, 2001). Hence formins can up-regulate actin polymerisation and FA formation in response to mechanical signals.

p130 Cas, an adaptor protein, is another known mechano-transducer associated with FAs. It has recently been shown to become activated in response to mechanical stretching (Sawada *et al.*, 2006), and has also been shown to be activated following fluid flow in a manner dependent on Src (a tyrosine kinase) activation (Okud *et al.*, 1999).

These examples illustrate two points, firstly that mechano-transduction via FAs is not only feasible, but probable. Secondly, mechano-transduction in FAs could involve activation of synergistic, or even competing, pathways.

The exact role for integrins remains unclear. Increased tension at cell-ECM contact points leads to further recruitment of integrin and FA-associated proteins suggesting some initial mechano-transduction, but further signalling could be due to new integrin binding to the ECM (Katsumi *et al.*, 2004) - giving a possible method of signal amplification by positive feedback.

Tzima *et al.* (2005) suggest that PECAM-1 and VEGFR2 (vascular endothelial growth factor receptor 2) act as the initial transducers of mechanical force at cell-cell adhesions, inducing integrin activation and substrate binding via a PI(3)-K (Phosphatidylinositol-3-OH kinase) mediated mechanism as well as Src activation. Recently integrins have been shown to be activated in the downstream regions of ECs exposed to fluid flow via this pathway (Goldfinger *et al.*, 2008), although a FA induced pathway may contribute to the activation of this pathway. Chiu *et al.* (2008) argue for two mechanisms of Src activation, a hypothesis that is supported by observations that EC polarisation is not dependent on PI(3) kinases, (Wojciak-Stothard & Ridley, 2003). However basal levels of active PECAM-1 may be necessary for Src activation.

5.2 Modelling Mechano-transduction

The focus therefore is on modelling mechanical transduction by integrin complexes and its downstream effectors. Given that it is likely that several mechano-transduction pathways arise from different FA associated proteins, each transducing the force independently, a way to simplify this complexity is sought. Rather than model each mechano-transducer explicitly a model of one of its effectors is taken as a ‘read out’ from the system.

The tyrosine kinase Src is chosen to take on this role. In ECs Src has been shown to be activated by fluid flow (Jalali *et al.*, 1998; Fleming *et al.*, 2005) and *in vivo*, Src has been shown to be quickly activated in response to artificial forces applied to cell surfaces (Wang *et al.*, 2005). Also tyrosine kinases have been linked to ion channel activation, Hoger *et al.* (2002) showed that inhibition of tyrosine kinases prevented ion channel opening in ECs responding to flow.

Src is a good candidate to act as a barometer of mechano-transduction at FAs because of its centrality in the signalling network with respect to components known to play an important role in EC elongation in response to fluid flow. Evidently Src is closely linked to mechano-transduction, and as will be discussed in chapter 6 may play a role in linking (directly or indirectly) mechano-transduction and Rho GTPases.

A simple scheme is used to link the flow model to Src activity. The flow normal to the cell surface is taken to act on the mechano-transducer (which, seeing as only the Src activity is tracked, can be identified as the integrin complex as a whole, rather than specific components). As discussed the normal force is the best candidate for the initial cause of asymmetry in cell signalling. However shear forces could play an important role in initiating other aspects of the signalling pathways, via ion channels or increased tension at cell-cell adhesions.

In this work the PECAM-1 pathway is ignored. Thi *et al.* (2004) suggest signalling at cell-adhesions due to torque across the cell arising from shear-stress, it is believed this pathway may play a role in the case of confluent layers (Goldfinger *et al.*, 2008). The model initially consists of a lone cell that has no cell-cell attachments, so signalling can not be initiated by increased tension at these points, although PECAM-1 could respond to tension in single, non-attached, cells via cytoskeletal linkages. Here the mechano-transducer that leads to local zones of signalling is hypothesised to be located in integrin complexes.

5.2.1 Modelling the mechanical effect of normal surface force

The force normal to the cell surface is taken to act on a viscous-spring (Kelvin body) model of a mechano-transducer. Then the extension of the body is taken to (non-linearly) up-regulate Src activity. The parameters are ascertained from a simplified analytical estimation so that the maximum fold increase in active Src matches experimentally found values and the time to reach this maximum is also matched to experimental data.

The first modelling assumption made is that the mechano-transducer has a uniform distribution across the basal surface of the cell. As discussed, integrins cluster together to form FAs, composed of discrete groups of integrins. However targets of this signalling network do not (at experimental resolutions) show discrete points of activation, even if they are spatially localised to the downstream edge, for example Rac activation (Tzima *et al.*, 2002). Hence, from a modelling perspective, it is anticipated this assumption does not affect the outcome. That withstanding, it shall be shown that this discrete localisation of integrins to FAs may play a role in attenuating the signalling network in cells aligned in the direction of flow (chapter 6).

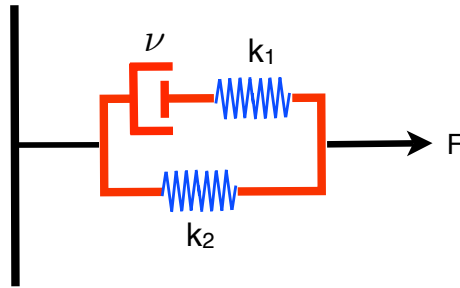


Figure 5.2: Kelvin body model of integrin complex deformation. For integrin complexes the parameters have been established, by modelling experimental data, as $\nu = 6.33 \times 10^{-5} \text{ Pa m s}$, $k_1 = 1.25 \times 10^{-3} \text{ Pa m}$ and $k_2 = 1.61 \times 10^{-3} \text{ Pa m}$, (Bausch *et al.*, 1998; Mazzag *et al.*, 2003).

The mechano-transducer is modelled as a Kelvin body (figure 5.2) which is a visco-elastic body comprised of two springs of spring constants k_1 and k_2 and a dashpot of viscosity ν . These parameters have been estimated, (Bausch *et al.*, 1998), for integrin complexes by attaching a micro-bead to the surface and applying a force. Bausch *et al.* (1998) assumed the resulting visco-elastic response consisted of the response of integrins, membrane and cytoskeleton and found corresponding parameters by fitting

Kelvin body models to each of these responses.

To prescribe the load on the mechano-transducer it is assumed that the force (calculated from the flow model) on a triangular surface element adds to the total force on a hexagon at $z = 0$ (cf. figure 4.3), hence the total force on a hexagon is a sum of four surface forces. Each of these hexagons has its own mechano-transducer, modelled as a Kelvin body. Note that the extension does not change the geometry of the 3D cell, here its only purpose is to use in an expression for Src up-regulation.

The equation governing the Kelvin body (Mazzag *et al.*, 2003), given that the force is constant, is

$$v \left(1 + \frac{k_1}{k_2} \right) \frac{dz_e}{dt} = k_1 z_e - F \quad (5.1)$$

where F is the force on the body and z_e is its extension. The normal force to each surface element is calculated by $E^m(\mathbf{f}^m \cdot \hat{\mathbf{n}}^m)$ where \mathbf{f}^m is the surface force on the m^{th} surface element, as in the discretised boundary integral representation (equation 4.53), $\hat{\mathbf{n}}^m$ and E^m are the normal to and area of the m^{th} element respectively.¹⁹

To apply the parameters found experimentally (figure 5.2) the force on each hexagon needs to be scaled. This is because these parameters were obtained by attaching a microbead to the cell with an estimated area of approximately $6 \mu m^2$ in contact with the cell, (Bausch *et al.*, 1998), hence, if the density of integrins per μm^2 is I_N then the force applied (experimentally) is shared between $6I_N$ integrins. So the parameters actually correspond to the response of $6I_N$ integrins complexes in parallel, which assuming they respond identically is equivalent to each integrin bearing an equal fraction of the force.

If the area of a hexagon is denoted H the number of integrins on the hexagons is $I_N H$ and if the force, F_N , is scaled by

$$F_K = F_N \frac{6I_N}{I_N H} = 6 \frac{F_N}{H} \quad (5.2)$$

then Kelvin body parameters can be applied. Hence if $H > 6 \mu m^2$ the extension is reduced because F_K is scaled down; the force is split between more integrin complexes than in the original experiment, whereas if $H < 6$ then the force is scaled up because the same force is split between less complexes - resulting in each complex experiencing a greater force.

¹⁹More precisely, this is calculated for each hexagon by summing the normal component of the force on the four surface elements that constitute a hexagon in the projection and multiplying the result by the total area.

In this analysis it is assumed that the density of integrin complexes in the experiments of Bausch *et al.* (1998) are characteristic of a typical cell and that integrin complexes only respond to tensile and not compressive forces, hence the Kelvin-body extension was taken as $z_e \geq 0$.

With these assumptions the force on the virtual cell leads to the deformation pattern shown in figure 5.3. Remarkably, given the multitude of assumptions regarding both the fluid and the mechano-transducer, this gives a realistic value for the deformation of a mechano-transducer. It is perfectly feasible that a 10 nm stretch could expose cryptic binding sites, or significantly change the binding affinity of ligands. Note, this corresponds to the stretch of a mechano-transducer complex - not a deformation across the whole basal-apical thickness of the cell.

This deformation is a prediction of the extension of the complex as a whole due to forces normal to the surface. Conclusions about any specific tension-induced activation mechanisms can not be drawn. For example the total extension could be due to conformational change of several proteins, or due to an unfurling (with no conformational change in the constituent proteins) of the complex as a whole

Note that the shear component of the surface force and internal (acto-myosin for example) forces are deliberately excluded from acting on the mechano-transducer. The latter on the grounds of simplicity. The shear component was ignored because, as was argued, it is unlikely to establish cell polarity. It is important to point out that this model is dependent on a mechano-transducer that responds to normal and not shear forces (for example if F applied to the Kelvin body was simply the magnitude of the surface force vector, rather than the magnitude of the normal component, then the deformation would be symmetrical in the up and downstream regions). Since integrins bound to the ECM are always in a similar orientation (roughly normal to the ECM) it is plausible to suggest that one component of the complex responds to normal forces but is screened from shear forces.

5.2.2 Transducing the Mechanical Signal

To convert the mechanical force into a biochemical signal the tyrosine kinase Src is taken as a barometer of FA signalling. Since little is known about the parameters governing mechano-transducers the Src output is matched against experimental data. This is more prescriptive than desirable, although less so than carrying out the equivalent

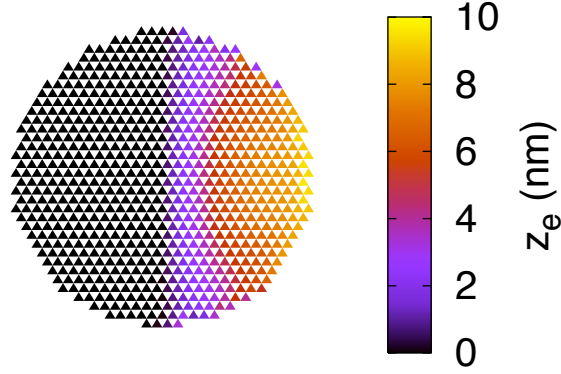


Figure 5.3: The force normal to the cell surface is applied to equation 5.1 which represents the Kelvin body (figure 5.2). This gives a predicted steady-state pattern of integrin complex deformation. Note that compressive forces were ignored and integrin clustering was coarse grained into a uniform distribution.

in a non-spatial model because only the whole cell time course is matched (not least because specific experimental data on localised activity and spatial gradients of Src activation is not available), whereas the distribution of Src activation is not fixed.

Src is modelled simply as having an inactive and active state (*), with transition between the two governed by a back rate k_- and forward rate $k_+(z'_e)$, where z'_e is the relative extension of integrin complexes such that $z'_e = z_e/k_z$, with $k_z = 1$ nm.



the forward rate depends on the integrin complex extension, z'_e , and is taken to be

$$k_+(z'_e) = k_+ + \frac{k_m}{1 + e^{10 - z'_e}} \quad (5.4)$$

figure 5.4 shows the form of the $k_+(z'_e)$ function, with the parameter choices for k_+ and k_m . For the maximal extension, 10 nm, a significant increase in forward rate is assumed, whereas for extensions less than 5 nm there is little effect. Large extensions achieve the maximum forward rate. k_+ , figure 5.4 is only valid for flows in the physiological range.

To establish estimates for these rates two observations are noted; typical peak active Src following the onset of physiological flow (12 dynes/cm²) and the time in which this peak is obtained. It has been observed that there is a 2-6 fold peak of Src activation

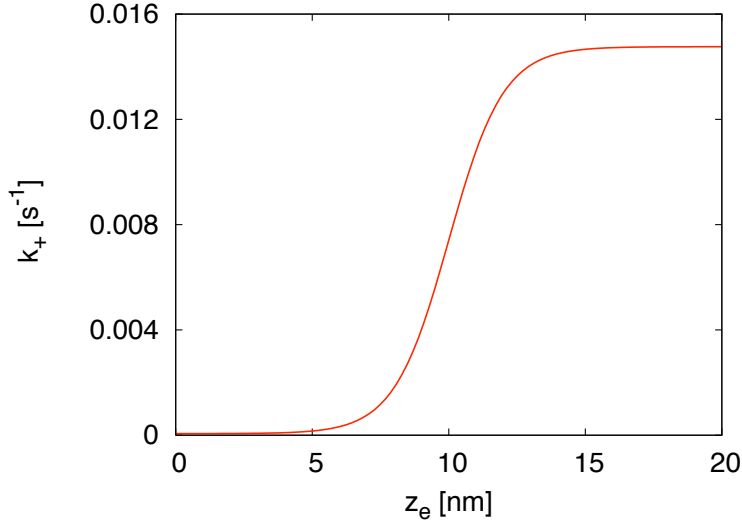


Figure 5.4: Up-regulation of the forward Src activation rate $k_+(z_e)$, equation 5.3, as a function of mechano-transducer extension z_e : $k_+(z_e') = 0.0006 + 0.0147/(1 + e^{(10-z_e')})$, where $z_e' = z_e/k_z$ and $k_z = 1$ nm

approximately 5 minutes following the onset of shear flow (Jalali *et al.*, 1998; Fleming *et al.*, 2005). Since three parameters need to be established (k_+ , k_- and k_m), one other relationship has to be assumed. This is taken that $k_+ = 0.01k_-$, which implies that initially only approximately 1% of total Src is active. This is a biologically reasonable assumption, made previously by Fuß *et al.* (2007) for modelling Src family kinase deactivation.

In order to proceed, the total Src is normalised to one, so that reaction 5.3 is described by one ordinary differential equation for the active Src, S^*

$$\begin{aligned} \frac{dS^*}{dt} &= k_+(z_e')(1 - S^*) - k_-S^* \\ &= k_+(z_e') - (k_+(z_e') + k_-)S^* \end{aligned} \quad (5.5)$$

where, due to the normalisation, $S^* + S = 1$. Diffusion is being ignored for this analysis, so the only spatial component comes from the positional dependence of z_e' . The solution to equation 5.5 is

$$S^* = \frac{-De^{-(k_+(z_e') + k_-)t} + k_+(z_e')}{k_+(z_e') + k_-} \quad (5.6)$$

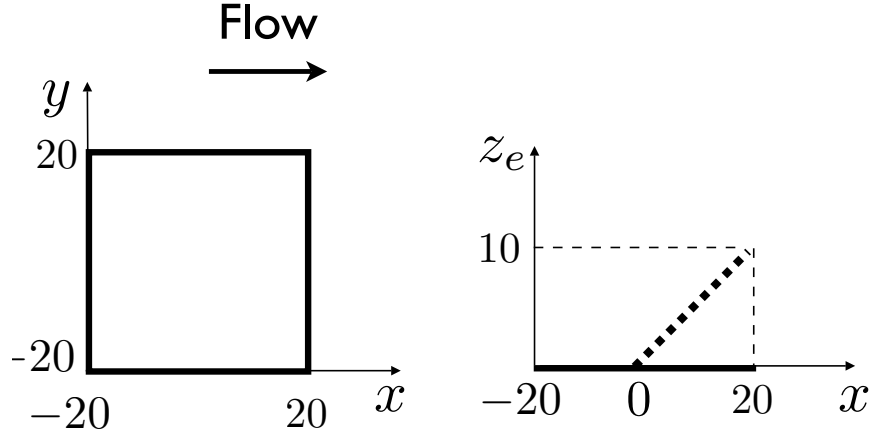


Figure 5.5: Approximation to the model results. The cell is assumed to have a square projection (left figure), and the fluid flow (left to right) induced extension of the mechano-transducer (right figure) is assumed linear between 0 at $x = 0$ to 10 nm at $x = 20 \mu\text{m}$. z'_e is assumed constant in the y direction.

where D is some positive constant depending on the initial conditions. Hence, according to this expression, active Src asymptotically approaches its maximal value $k_+(z'_e)/(k_+(z'_e) + k_-)$, as the exponential term decays. Since this is observed to be obtained in about 300 s the value of $300(k_+(z'_e) + k_-)$ is taken so the exponential term is negligible, placing a restriction upon the parameters, k_+ , k_m and k_- .

To find the total Src activation analytically, in terms of k_+ , k_- and k_m , an approximation to the cell and the mechano-transducer extension (figure 5.3) is employed (figure 5.5). The cell is approximated by a square region of length $40 \mu\text{m}$ and the extension of the mechano-transducer is characterised as increasing linearly from 0 to 10 nm in the downstream half of the cell.

Assuming that the active Src is at steady state, which is

$$\hat{S}^* = \frac{k_+ + k_m / (1 + e^{10 - z'_e})}{k_+ + k_- + k_m / (1 + e^{10 - z'_e})}. \quad (5.7)$$

Denote the basal level of active Src by S_b^* . Then the total level of active Src, T , is

$$T = 20.40 \cdot S_b^* + \int_0^{20} 40 \hat{S}^* dx \quad (5.8)$$

by changing variables and by substituting the linear approximation for z'_e as $z'_e = mx$ (where $m = \frac{1}{2} \mu m^{-1}$, figure 5.5) the integral can be solved as

$$T = 40 \left[\frac{k_+ x}{k_+ + k_-} + \frac{2k_m k_- \log(e^{10}(k_- + k_+) + (k_m + k_- + k_+)e^{x/2})}{(k_m + k_- + k_+)(k_+ + k_-)} \right]_0^{20}. \quad (5.9)$$

The fold increase in Src is $F_S = T / (40^2 S_b^*)$, taking $S_b^* = k_+ / (k_+ + k_-)$ gives F_S as

$$F_S = 1 + \frac{1}{20} \frac{k_m k_-}{k_+ (k_m + k_- + k_+)} \log \left(\frac{e^{10}(k_- + k_+) + e^{10}(k_- + k_+ + k_m)}{e^{10}(k_- + k_+) + (k_- + k_+ + k_m)} \right). \quad (5.10)$$

By dividing top and bottom of the argument by e^{10} the logarithmic term is of the form $\log[(a + a + b)/(a + d)]$ where $d \ll 1$, assuming $O(k_m) = O(k_-)$ the logarithm is approximately 3, $\log(3) \approx 1$ for natural logarithms, and recalling $k_+ = 0.01k_-$ gives

$$F_S \approx 1 + \frac{100}{20} \frac{k_m}{(k_m + k_-)}. \quad (5.11)$$

Experimental data reports F_S to be in the range 2-6 (Jalali *et al.*, 1998; Fleming *et al.*, 2005), here this implies

$$0.7 \approx \frac{k_m}{(k_m + k_-)} \quad (5.12)$$

So $0.7k_- = 0.3k_m$. Since $300(k_+(z'_e) + k_-)$ must be large²⁰ $300(k_m + k_-)$ must also be large. In order to estimate the parameters $300(k_m + k_-) = 6$ was found to be a suitable choice (this means the exponential term in equation 5.6 corresponds to 0.00247). These considerations give the parameters as $k_- = 0.0006 \text{ s}^{-1}$, $k_m = 0.0147$ and $k_+ = 0.006 \text{ s}^{-1}$.

The flow model can now be coupled to the model of Src activity. Here reaction is implemented on the discretised cell, with the forward reaction rate a function of mechano-transduction extension as described. In this numerical solution diffusion is also considered, hence equations for both active and inactive Src are solved, although Src is plasma membrane associated and hence has slow diffusion. Numerically solving diffusion equations on this hexagonal lattice will be described in section 6.

Figure 5.6 shows the average increase in active Src over the cell following the onset of flow at 500 s. As demanded it reproduces typical Src activation reported in *in vivo* experiments. Although this outcome is prescribed, one aspect of Src activation that is

²⁰In the sense that $e^{-(300(k_+(z'_e) + k_-))}$ is small

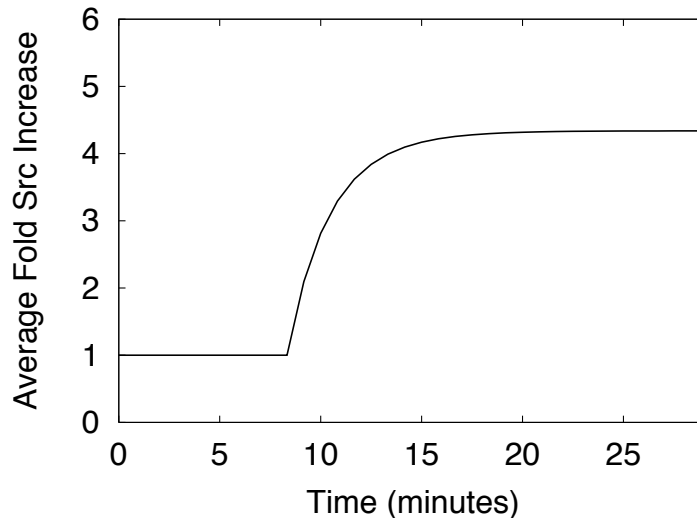


Figure 5.6: Fold Src increase as a whole cell average. The parameters of Src activation due to Kelvin-body extension are fixed so this matches experimental data

not fully fixed is the spatial localisation of Src activation. The pattern generated using this model is shown in figure 5.7. Such a pattern is not experimentally verified (to the author’s knowledge), and hence would be a good test of this model. However, if Src activation turned out not to be activated in a spatially localised fashion this would not necessarily mean this model was incorrect - but that a different candidate ‘read-out’ from protein FA could play the role of Src.

It will be argued in chapter 6 that Src could play a key role in regulating Rho GTPases during EC polarisation, specifically Rac and Rho. Given that Rac is known to be activated only at the downstream edge (Tzima *et al.*, 2002), it is clear that there should be some spatial localisation of the components of the signalling network that link Rac activation to mechano-transduction. Logically, however, only one intermediary component is required to be spatially localised, that is to say that if there is a linear chain $A \rightarrow B \rightarrow \text{Rac}$ then both A and B would necessarily have to be localised whereas if a number of signalling molecules act synergistically to promote Rac activation only one need be spatially localised, for example $A \rightarrow B \rightarrow \text{Rac} \leftarrow C$ implies that A and B might be globally activated as long as C is locally activated.

In this model, and in the absence of better experimental data suggesting which signalling network components are activated at the downstream edge, it is assumed that

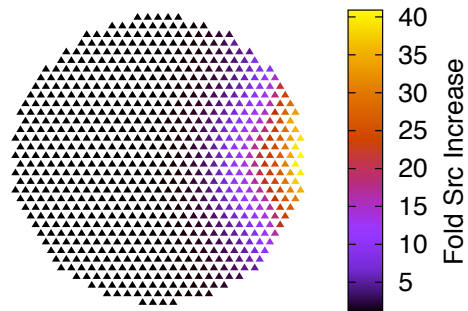


Figure 5.7: Distribution of Src in a single cell as a result of activation via the Kelvin body model.

a linear chain of interacting components lead to Rac spatial activation, and hence each component is itself localised. Specifically, $\text{Src} \rightarrow \text{Rac GEF} \rightarrow \text{Rac}$.

6 Modelling Rho GTPase Activity

In this section the Rho GTPases Rho and Rac are coupled to the force-activation model by Src activation of a Rac GEF and Rho GAP, leading to Rac activation and Rho inhibition.

The coupling of the fluid flow model (via a simple model of mechano-transduction, chapter 5.1) to a model of Rho GTPase activation is a novel contribution and (to the authors knowledge) represents the only spatial model of Rho GTPase activation in response to fluid flow in ECs.

6.1 Rho GTPase Background

6.1.1 Rho GTPase Regulation

The Rho family of small G-proteins is a subfamily of the Ras superfamily of GTPases and contains 20 members (Boureux *et al.*, 2007). They are crucial in regulating many responses involving cytoskeletal re-organisation including; cell migration, mitosis, lamellipodia formation and filopodia formation (Ridley, 2001; Narumiya & Yasuda, 2006; Ridley, 2006; Jaffe & Hall, 2005)

Rho GTPases switch between inactive GDP-bound, or an active GTP-bound state where they can interact with target effectors (figure 6.1), and as such they are often referred to as molecular switches. Switching between these states occurs on the membrane and is regulated by (membrane bound) guanine nucleotide exchange factors (GEFs), and GTPase activating proteins (GAPs), Bos *et al.* (2007). Some Rho GTPases are regulated by guanine nucleotide dissociation inhibitors (GDIs) which prevent the GTPase interacting with the plasma membrane (and hence subsequent activation) (DerMardirossian & Bokoch, 2005).

It is in their active, GTP-bound state that the Rho GTPases can regulate cellular networks (figure 6.1). In this state they interact with specific targets which become activated via a conformational change upon GTPases binding (Jaffe & Hall, 2005).

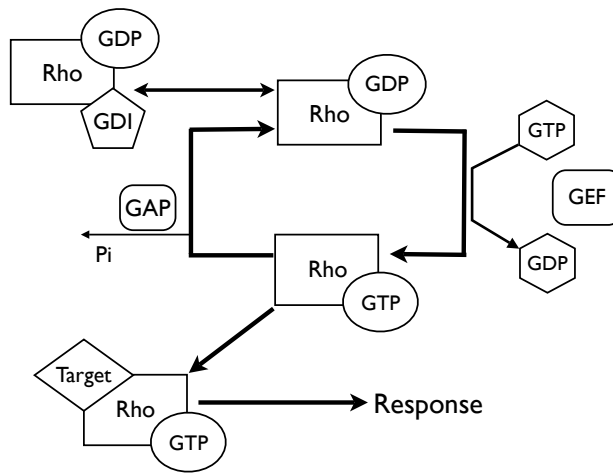


Figure 6.1: Rho GTPase regulation by GTPase activating proteins (GAPs), guanine nucleotide exchange factors (GEFs) and guanine nucleotide dissociation inhibitors (GDIs). In the inactive state (GDP bound) the interaction of GTPases with the plasma membrane is inhibited by interaction with a GDI, which in turn prevents activation by binding of a GEF at the membrane. The GEF removes GDP from the GTPase followed by removal of the GEF. Binding of GTP occurs quickly (because of the high ratio of GTP to GDP in cells). Hydrolysis of Rho GTP is induced by binding of a GAP.

6.1.2 Rho GTPase Targets

The most studied Rho GTPases are Rho, Rac and Cdc42. Rac and Rho have isoforms (for example, RhoA, RhoB and RhoC) within the Rho GTPase family, which are referred to here collectively as Rac and Rho with no distinction made between them. Rho, Rac and Cdc42 have been shown to be necessary for endothelial cell elongation, however the process of establishing polarity is not Cdc42-dependent (Wojciak-Stothard & Ridley, 2003). The GTPase targets that are important in this process are summarised in figure 6.2. Rac and Cdc42 lead to membrane protrusions induced by actin: both can contribute to formation of lamellipodia and Cdc42 can lead to filopodia. Conversely Rho is generally associated with actomyosin contraction of the cell (although Rho can also induce actin polymerisation via the Diaphanous-related formin mDia).

The small GTPase Rho is one of the most studied components of the signalling network. When endothelial cells polarise it has been demonstrated that the process has two stages, firstly cell rounding/contraction orchestrated by Rho and then Rho and Rac - mediated cell elongation (Wojciak-Stothard & Ridley, 2003). Rho induces actomyosin

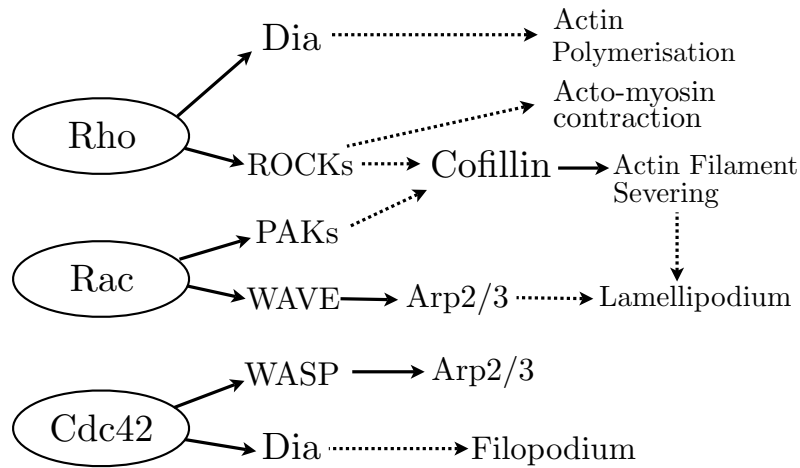


Figure 6.2: Rho GTPase targets involved cell protrusions, migration, contractions and EC elongation.

contraction by increasing the kinase activity of ROCKs (Rho Kinases) which stimulate phosphorylation of myosin light chain (Riento & Ridley, 2003). ROCKs and myosin light chain kinase (MLCK) phosphorylate one of the light chains of myosin II (figure 6.3). Once activated, myosin II moves along filaments, forcing them to slide over one another. Accordingly, it has been shown that inhibition of ROCK results in the slowing of the viscoelastic retraction of a single stress fibre (Kumar *et al.*, 2006). Another target (via LIM kinases, LIMKs) of activated ROCKs, as well as Rac, is de-activation of cofilin, resulting in an increase in polymerised actin, (Ridley, 2006). Cofilin severs filaments and is important in lamellipodia for formation of short branched filaments (chapter 3).

Rho induces an increase in both filaments and contraction, and it is tempting to speculate that both of these factors are invoked to guide the cell towards an isotropic state ready for elongation in the flow direction. Furthermore increased tension in filaments leads to maturation and maintenance of focal complexes into focal adhesions. Rac however induces formation of focal complexes, (Rottner *et al.*, 1999), which are usually located at the edge of the lamellipodium, (Geiger *et al.*, 2001).

During elongation in ECs due to fluid flow Rac is activated at the downstream edge of the cell, (Tzima *et al.*, 2002). In this local region Rac initiates *de novo* polymerisation nucleated by the Arp2/3 complex via WAVE (leading to a branched network of actin, as described by the Brownian dynamic model in section 3.1). Although Cdc42 can also

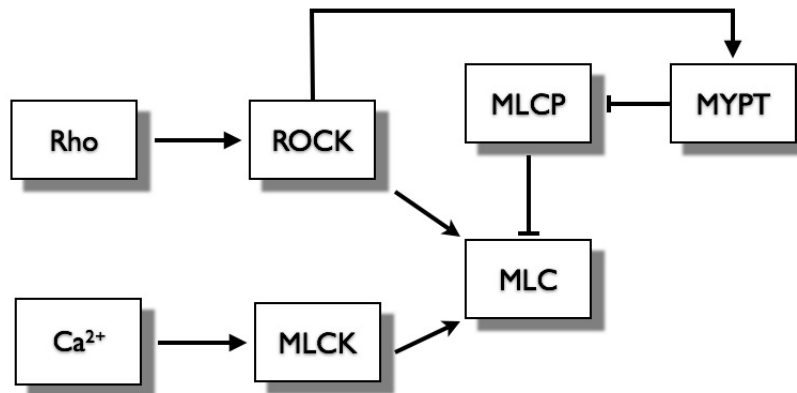


Figure 6.3: The regulatory myosin light chain (MLC) of Myosin II is phosphorylated by both ROCK and myosin light chain kinase (MLCK). Once phosphorylated MLC can induce actomyosin contraction. Myosin light chain phosphatase (MLCP) inhibits this contraction by dephosphorylation of MLC. ROCK might inhibit action of MLCP by phosphorylation of myosin phosphatase target subunit (MYPT). MYPT is a subunit of MLCP, upon phosphorylation by ROCK it dissociates from MLCP - this might inhibit MLCP activity (Kawano *et al.*, 1999; Riento & Ridley, 2003).

activate Arp2/3 via WASP (Jaffe & Hall, 2005), it has been shown that WASP knockouts still form lamellipodia (Snapper *et al.*, 2001), which suggests that although both Rac and Cdc42 contribute to this process it is Rac that plays the more important role in mediating cell elongation from the downstream edge (rather than the alternate possibility that the cell extends equally in both the downstream and upstream directions).

6.1.3 Rho GTPase Crosstalk

Migrating cells establish front and back pathways to orchestrate both elongation at the leading edge as well as contraction at the rear. It is argued, from a modelling perspective, that crosstalk between the GTPases is necessary in maintaining these pathways, although the exact mathematical mechanism to achieve this varies (Jilkin *et al.*, 2007; Narang, 2006; Otsuji *et al.*, 2007).

The nature of the crosstalk appears to be context dependent. There is evidence for ROCK activating FilGAP which leads to Rac inhibition. Hence Rho can inhibit Rac by the ROCK pathway (Ohta *et al.*, 2006). Rac can inhibit Rho via a redox-dependent pathway (Nimmual *et al.*, 2003), although there is also evidence for Rho activation by

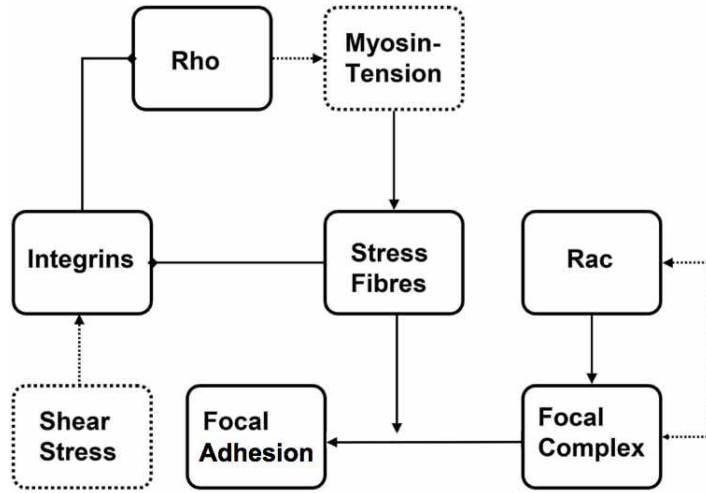


Figure 6.4: The model proposed by Geiger & Bershadsky (2001) and described mathematically by Civelekoglu-Scholey *et al.* (2005). Arrows indicate up-regulation or activation, diamond indicates down-regulation or deactivation.

Rac and Cdc42 (Nobes & Hall, 1995).

Transient coupled changes in activity of Rho and Rac has been previously modelled by Civelekoglu-Scholey *et al.* (2005). This model reproduced similar dynamics of Rho and Rac as reported by Tzima *et al.* (2001, 2002). Their heuristic approach describes the interaction of Rho and Rac with integrins, focal complexes, focal adhesions and stress fibres. Geiger & Bershadsky (2001) originally proposed the schema of interaction of these elements (figure 6.4). Clearly with a heuristic model the finer details are lost, and interactions are greatly simplified. The advantage is that it is far more readily understood and computationally cheaper. Mathematically Civelekoglu-Scholey *et al.* (2005) represent figure 6.4 as:

$$\begin{aligned}
 \frac{di}{dt} &= -k_1 g(s) i \\
 \frac{d\rho}{dt} &= k_2 (1 - k_3 i - \rho) \\
 \frac{dc}{dt} &= k_4 (1 - sc) + k_5 c \\
 \frac{df}{dt} &= k_4 (sc - f) \\
 \frac{ds}{dt} &= k_6 (\rho - s)
 \end{aligned} \tag{6.1}$$

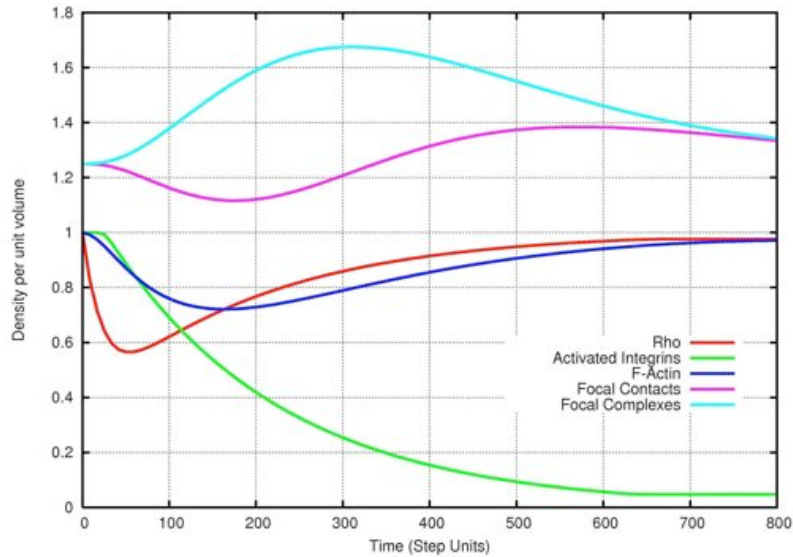


Figure 6.5: Numerical solution of coupled equations 6.1 (Civelekoglu-Scholey *et al.*, 2005). Transient changes in Rho, activated integrins, F-actin, focal adhesions and focal complexes are shown. Rho and Rac (here proportional to focal contact activity) dynamics are qualitatively similar to those observed (Tzima *et al.*, 2001, 2002).

where i , ρ , r , c , f and s are the ligated activated integrins, activated Rho, activated Rac, focal complexes, focal adhesions and stress fibres respectively and where $g(s) = 0$ or 1 depending on a critical value of stress fibre concentration. Civelekoglu-Scholey *et al.* (2005) assume that integrin activation is fast compared with the modelled processes and that decay of this signalling is ‘triggered by a change in intracellular tension’, so the signal decay is halted if the number of stress fibres (or tension) falls below a threshold level. The remaining terms arise from normalising so that in the absence of integrin signalling the components of the model have concentration 1. Rac concentration is approximately proportional to the density of focal complexes. The results of this model are shown in figure 6.5.

In this model integrin activation decays once F-actin falls below the threshold level. Stress fibre concentration drops due to inhibition of Rho and focal complex concentration increases due to less being converted into focal adhesions due to stress fibre concentration falling.

Although this model captures the dynamics of the system faithfully (partly from some

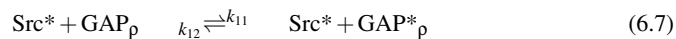
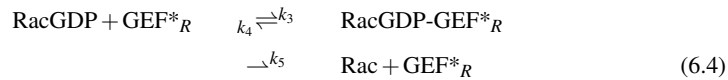
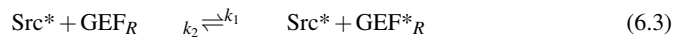
judicious parameter choices) it does not describe spatially localised activation. Furthermore the schema of interaction (figure 6.4) is not the hypothesis the author would prefer to make. The network suggested by Geiger & Bershadsky (2001) is highly speculative (figure 6.4). In the next sub-section a network describing dynamics of Rho and Rac is put forward. The advantage of this approach is that it describes (mostly) direct interactions for which there is specific evidence for their occurrence. This model serves as a reductionist template for regulation of cell morphogenesis because Rho and Rac are known to mediate contraction and extension respectively.

6.2 Modelling the Role of GTPases in Endothelial Cell Elongation

Given the importance of both Rho and Rac in mediating EC polarisation and elongation it is instructive to model their direct response to Src activation. It is not obvious that such a hypothesis would lead to local Rac activation, because if diffusion (of Src, Rac GEF or Rho GTP) is fast enough then the resulting Rac GTP distribution may not be restricted to the downstream edge.

Src has been shown to be able to activate a Rac GEF, Vav2 (Garrett *et al.*, 2007), and conversely integrin binding can activate a Rho GAP (p190RhoGAP) via a Src dependent mechanism (Arthur *et al.*, 2000). There is no suggestion that Src activates Rac GEFs or Rho GAPs exclusively, or indeed that *in vivo* GEFs and GAPs are necessarily specific to distinct GTPases. Here though it is assumed that Src activates a GEF exclusive to Rac and inhibits a GAP exclusive to Rho. In this context activation of Rac and Rho crosstalk is modelled as mutual inhibition via Rac inhibition of a Rho GEF and Rho activation of a Rac GEF (figure 6.6).

The reactions governing this network are



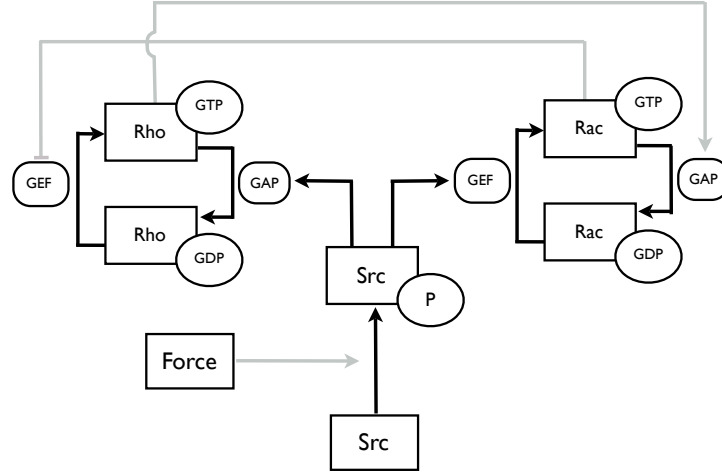
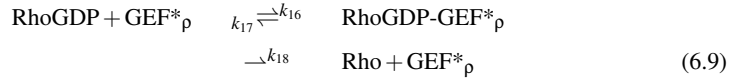


Figure 6.6: Proposed Rho, Rac and Src network. Mechanical force on the cell leads too (indirectly) Src tyrosine phosphorylation. Phosphorylated Src can activate a Rho GAP as well as a Rac GEF - leading to Rac activation and Rho inhibition. Rho and Rac mutually inhibit each other: Rho-GTP activates a Rac GAP and Rac-GTP inhibits Rho by inhibiting a Rho GEF. Direct interactions in black, indirect interactions in grey.



where the subscript R refers to Rac and ρ to Rho, for example GAP_{ρ} is a GAP for Rho. These equations model Rho and Rac regulation by GEFs and GAPs, Src activation and inactivation and Rho-Rac mutual inhibition. The influence of GDIs, which sequester Rho GTPases away from the membrane, is not modelled although the effect of this sequestration can be modelled by assuming a quasi-steady state between GDI bound and unbound GTPase and a modified diffusion coefficient (Jilkin *et al.*, 2007). This approach is followed here: a diffusion coefficient of D_m refers to a species solely mem-

brane bound, whereas D_{mc} represents weighted average diffusion on the membrane and in the cytosol.

Reactions (6.2)-(6.14) are modelled mathematically as first order mass action differential equations with diffusion, for example for a complex A_j interacting with complexes A_i $0 \leq i \leq n$ the time evolution of the concentration of A_i at time t and position \mathbf{x} , $A_i(\mathbf{x}, t)$, is modelled as:

$$\frac{\partial A_i}{\partial t} = \sum_{j=0}^n \alpha_j A_j + \sum_{k=0}^n \sum_{i=0}^n \beta_{jk} A_j A_k + D_i \nabla^2 A_i. \quad (6.15)$$

If the interaction between A_j and A_k does not occur then $\beta_{jk} = 0$. Applying this expression for each component of the network (figure 6.6) leads to

$$\begin{aligned} \frac{\partial(\text{Src}^*)}{\partial t} &= k_+(z_e)(\text{Src}) - k_-(\text{Src}^*) + D_m \nabla^2(\text{Src}^*) \\ \frac{\partial(\text{Src})}{\partial t} &= k_-(\text{Src}^*) - k_+(z_e)(\text{Src}) + D_m \nabla^2(\text{Src}) \\ \frac{\partial(\text{RacGDP})}{\partial t} &= k_8(\text{RacGAP}) + k_4(\text{RacGEF}) - k_3(\text{RacGDP})(\text{GEF}_R) \\ &+ D_{mc} \nabla^2(\text{RacGDP}) \\ \frac{\partial(\text{RacGTP})}{\partial t} &= k_5(\text{RacGEF}) - k_6(\text{RacGTP}).(\text{GAP}_R) + k_7 \text{RacGAP} \\ &+ D_m \nabla^2(\text{RacGTP}) \\ \frac{\partial(\text{RhoGDP})}{\partial t} &= k_{15}(\text{RhoGAP}) + k_{17}(\text{RhoGEF}) - k_{16}(\text{RhoGDP})(\text{GEF}_\rho) \\ &+ D_{mc} \nabla^2(\text{RhoGDP}) \\ \frac{\partial(\text{RhoGTP})}{\partial t} &= k_{18}(\text{RhoGEF}) - k_{15}(\text{RhoGTP}).(\text{GAP}_\rho) + k_{14} \text{RhoGAP} \\ &+ D_m \nabla^2(\text{RhoGTP}) \\ \frac{\partial(\text{GEF}_\rho^*)}{\partial t} &= k_{27} \text{GEF}_\rho - k_{28} \text{GEF}_\rho^* + (k_{17} + k_{18}) \text{RhoGEF} - k_{16} \text{GEF}_\rho^* \cdot \text{RhoGTP} \\ &+ D_m \nabla^2(\text{GEF}_\rho^*) \\ \frac{\partial(\text{GEF}_R^*)}{\partial t} &= k_{23} \text{GEF}_R - k_{24} \text{GEF}_R^* + (k_4 + k_5) \text{RacGEF} - k_3 \text{RacGDP} \cdot \text{GEF}_R^* \\ &+ k_{20} \text{RacGTP} \cdot \text{GEF}_R - k_{19} \text{RacGTP} \cdot \text{GEF}_R^* - k_2 \text{Src}^* \cdot \text{GEF}_R^* + D_m \nabla^2(\text{GEF}_R^*) \\ \frac{\partial(\text{GAP}_\rho^*)}{\partial t} &= k_{21} \text{GAP}_\rho - k_{22} \text{GAP}_\rho^* + (k_{14} + k_{15}) \text{RhoGAP} - k_{13} \text{RhoGTP} \cdot \text{GAP}_\rho^* \\ &+ k_{11} \text{Src} \cdot \text{GAP}_\rho - k_{12} \text{Src} \cdot \text{GAP}_\rho^* + D_{mc} \nabla^2(\text{GAP}_\rho^*) \\ \frac{\partial(\text{GAP}_R^*)}{\partial t} &= k_{25} \text{GAP}_R - k_{26} \text{GAP}_R^* + (k_7 + k_8) \text{RacGAP} + k_9 \text{RhoGTP} \cdot \text{GAP}_R^* \end{aligned}$$

$$\begin{aligned}
& - k_{10}\text{RhoGTP} \cdot \text{GAP}_R^* - k_6\text{RacGTP} \cdot \text{GAP} + D_{\text{mc}}\nabla^2(\text{GAP}_R^*) \\
\frac{\partial(\text{GEF}_\rho)}{\partial t} &= -k_{27}\text{GEF}_\rho + k_{28}\text{GEF}_\rho^* + D_{\text{m}}\nabla^2(\text{GEF}_\rho) \\
\frac{\partial(\text{GEF}_R)}{\partial t} &= -k_{23}\text{GEF}_R + k_{24}\text{GEF}_R^* - k_{20}\text{RacGTP} \cdot \text{GEF}_R + k_{19}\text{RacGTP} \cdot \text{GEF}_R^* \\
& + D_{\text{m}}\nabla^2(\text{GEF}_R) \\
\frac{\partial(\text{GAP}_\rho)}{\partial t} &= -k_{21}\text{GAP}_\rho + k_{22}\text{GAP}_\rho^* - k_{11}\text{Src} \cdot \text{GAP}_\rho D_{\text{mc}}\nabla^2(\text{GAP}_\rho) \\
\frac{\partial(\text{GAP}_R)}{\partial t} &= -k_{25}\text{GAP}_R + k_{26}\text{GAP}_R^* - k_9\text{RhoGTP} \cdot \text{GAP}_R^* + k_{10}\text{RhoGTP} \cdot \text{GAP}_R^* \\
& + D_{\text{mc}}\nabla^2(\text{GAP}_R) \\
\frac{\partial(\text{RacGEF})}{\partial t} &= k_3\text{RacGDP} \cdot \text{GEF}_R^* - (k_4 + k_5)\text{RacGEF} + D_{\text{m}}\nabla^2(\text{RacGEF}) \\
\frac{\partial(\text{RhoGEF})}{\partial t} &= k_{16}\text{RhoGDP} \cdot \text{GEF}_\rho^* - (k_{17} + k_{18})\text{RhoGEF} + D_{\text{m}}\nabla^2(\text{RhoGEF}) \\
\frac{\partial(\text{RhoGAP})}{\partial t} &= k_{13}\text{RhoGTP} \cdot \text{GAP}_\rho^* - (k_{14} + k_{15})\text{RhoGAP} + D_{\text{mc}}\nabla^2(\text{RhoGAP}) \\
\frac{\partial(\text{RacGAP})}{\partial t} &= k_6\text{RacGTP} \cdot \text{GAP}_R^* - (k_7 + k_8)\text{RacGAP} + D_{\text{mc}}\nabla^2(\text{RacGAP})
\end{aligned}$$

It is assumed that free Rac or Rho (not bound to GDP or GTP) quickly binds to GTP due to the high ratio of GTP to GDP in the cell (Detimary *et al.*, 1995). The temporal component of these equations was discretised by a simple Euler method, where the solution for $df(t)/dt = g(t)$ is approximated by

$$f(t+h) = f(t) + h.g(t) \quad (6.16)$$

where h is the time-step, and the initial condition $f(0)$ needs to be prescribed.

The spatial part, which describes diffusion, was discretised using central differences defined on the regular hexagonal discretisation of the plane (section 4.5.1).

For the spatial discretisation consider a function f , in cartesian co-ordinates diffusion of f is modelled as

$$\nabla^2 f(x,y,t) = \frac{\partial^2 f}{\partial x^2} + \frac{\partial^2 f}{\partial y^2}. \quad (6.17)$$

So to discretise the operator ∇^2 it is necessary to discretise the second derivatives with respect to x and y . In the x direction the central difference approximation is

$$\frac{\partial^2 f_i}{\partial x^2} \approx \frac{f_{i+1} - 2f_i + f_{i-1}}{h^2} \quad (6.18)$$

where f_i is the value of the function f at the i th interval. Here equation 6.18 is applied for the approximation in the x direction, where f_{i-1} and f_{i+1} are the values of the function f at the hexagons immediately to the left and right of hexagon i respectively (figure 6.7).

In the y -direction the approximation is altered to

$$\frac{\partial^2 g_j}{\partial x^2} \approx \frac{g_{j+1} + g_{j+2} - 4g_j + g_{j-1} + g_{j-2}}{2h^2} \quad (6.19)$$

where g_{j+1} , g_{j+2} , g_{j-1} and g_{j-2} are the values of a second function g (introduced for clarity) above and below the j^{th} hexagon (figure 6.7). This alteration ensures diffusion

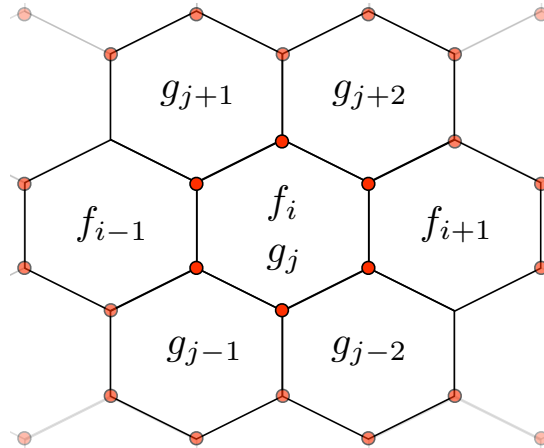


Figure 6.7: Diffusion on the hexagonal lattice is estimated by a modified central difference taken from the surrounding hexagons. See equations 6.18 and 6.19.

is approximated by taking the difference of all surrounding hexagons. For example equation 6.19 characterises the flux into the j^{th} hexagon from above, as an average of flux from hexagons $j + 1$ and $j + 2$. A similar approach could have been taken in the x -direction, however it was found this made no noticeable difference in this modelling, and complicated implementation of the boundary conditions.

It was assumed that there was no flux in or out of the cell of any of the proteins. Hence, the total amount (in all forms) of a protein in the cell is constant. No flux of f across a boundary C implies that the derivative in the direction normal to the boundary is zero

$$\nabla f \cdot \mathbf{n}|_C = 0 \quad (6.20)$$

where \mathbf{n} is the unit normal to the boundary. To implement this reflective boundary conditions are used (figure 6.8).

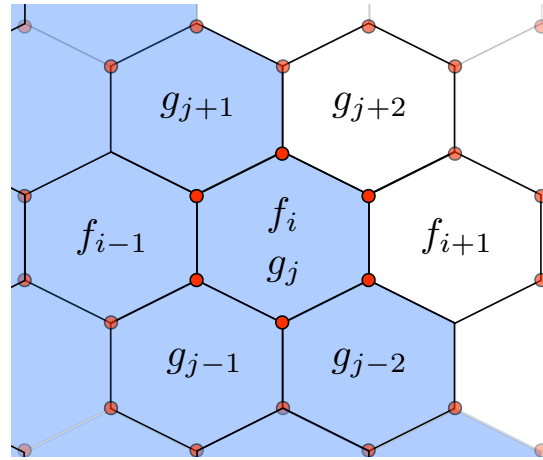


Figure 6.8: Diffusion on the boundary (shaded hexagons are in the cell). No flux is imposed by reflective boundary conditions, here for example by applying equations 6.18 and 6.19 with $g_{j+1} := g_{j-1}$ and $f_{i+1} := f_{i-1}$. This means there is no flux into the adjacent $j + 1$ th and i th hexagons.

The parameters used in this model are in the table below. For the GAP and GEF activation rates it was found that these were not the rate limiting steps in the network, figure 6.6. It was found that if the GEF activation rate was sufficiently fast then Rac activation occurred on a similar time scale to observed experimentally (Tzima *et al.*, 2002), hence it is necessary to have the Rac GEF activating quickly, on the order of a minute. Similarly for the Rho GAP. Rates for the Rac GAP and Rho GEF were taken to be comparable to the Rho GAP and Rac GEF, however they were altered slightly so that there were similar basal levels of the active forms of Rho and Rac (otherwise the basal level of Src gives a bias to the Rho GAP and the Rac GEF). Rates were finally fixed by demanding a low ratio initially of active to inactive forms, and that following the onset of flow the new level of active GAP or GEF was still significantly less than the total, so for physiological flows the active form does not completely dominate. Initial total concentrations of Rac and Rho (either active, inactive or bound in an intermediary complex) was taken to be $10 \mu\text{M}$ of each, which is a typical cellular amount (Jilkin *et al.*, 2007; Goryachev & Pokhilko, 2006). Total concentration of Rac GAP and Rho GAP, Rho GEF and Rac GEF was taken to be $1 \mu\text{M}$, $1 \mu\text{M}$, $2 \mu\text{M}$ and $2 \mu\text{M}$ respectively; with corresponding initial active concentrations of $0.46 \mu\text{M}$, $0.75 \mu\text{M}$, $0.41 \mu\text{M}$ and 0.2

Parameter	Value	Units	Parameter	Value	Units
D_m	0.1	$\mu m^2 s^{-1}$	k_{13}	0.017	$\mu M^{-1} s^{-1}$
D_{mc}	10	$\mu m^2 s^{-1}$	k_{14}	0.05	μs^{-1}
$k_+(z_e)$	fig 5.4	s^{-1}	k_{15}	8.3	μs^{-1}
k_-	0.006	s^{-1}	k_{16}	0.0034	$\mu M^{-1} s^{-1}$
k_1	0.83	$\mu M^{-1} s^{-1}$	k_{17}	1.1×10^{-6}	s^{-1}
k_2	0	$\mu M^{-1} s^{-1}$	k_{18}	0.094	s^{-1}
k_3	0.0034	$\mu M^{-1} s^{-1}$	k_{19}	0	$\mu M^{-1} s^{-1}$
k_4	1.1×10^{-6}	s^{-1}	k_{20}	0.0001	$\mu M^{-1} s^{-1}$
k_5	0.094	s^{-1}	k_{21}	0.002	s^{-1}
k_6	0.017	$\mu M^{-1} s^{-1}$	k_{22}	0.009	s^{-1}
k_7	0.05	s^{-1}	k_{23}	0.00045	s^{-1}
k_8	8.3	s^{-1}	k_{24}	0.09	s^{-1}
k_9	0.001	$\mu M^{-1} s^{-1}$	k_{25}	0.002	s^{-1}
k_{10}	0	$\mu M^{-1} s^{-1}$	k_{26}	0.004	s^{-1}
k_{11}	0.8	$\mu M^{-1} s^{-1}$	k_{27}	0.00045	s^{-1}
k_{12}	0	$\mu M^{-1} s^{-1}$	k_{28}	0.015	s^{-1}

$4\mu M$.

The parameters governing GTPase cycling between GTP and GDP bound states were found to be the most significant in governing the response, fortunately experimental data (previously used in modelling GTPases, Goryachev & Pokhilko (2006)) were available for these (Zhang *et al.*, 1997, 2000).

It would be interesting to conduct some form of sensitivity analysis on this system. To do so it would be necessary to identify target outputs from which the different simulation runs could be characterised. One of the important questions that this model aims to address is whether Rac activation (due to fluid flow) could be as a result of mechano-transduction by integrin complexes, here the total level of active Rac (Rac-GTP) is not as relevant as the resulting pattern in the cell. A general pattern is difficult to quantify in a manner that would facilitate application of standard sensitivity analysis techniques.

6.3 Rho GTPase Model - Results

With the model described above, a pattern of downstream activation for Rac is generated (figure 6.9), due to Src activation leading to activation of a Rac GEF and conversion of Rac-GDP into Rac-GTP. The whole cell response for Rac (figure 6.10), is

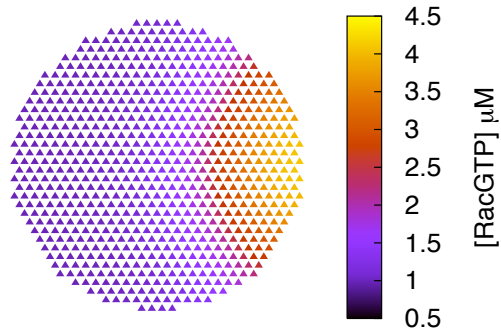


Figure 6.9: Cellular distribution of Rac-GTP according to the Rho GTPase model. Local activation of Src leads to local Rac GEF activation and subsequent conversion of Rac-GDP into Rac-GTP.

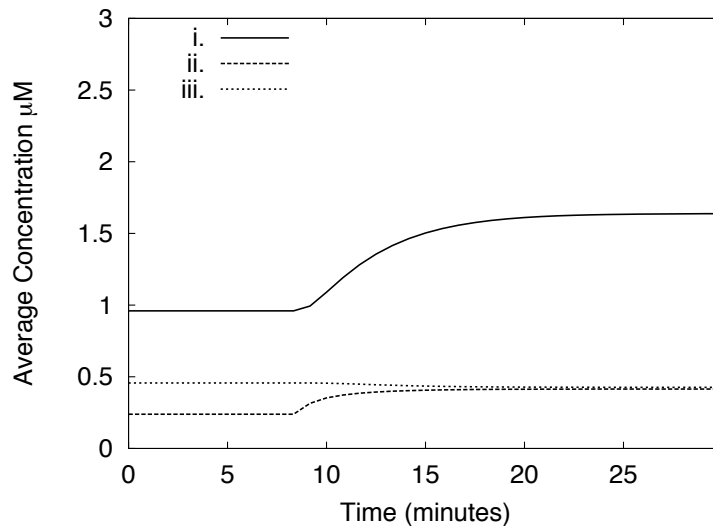


Figure 6.10: Whole cell responses of Rac-GTP (i), a Rac GEF (ii) and a Rac GAP (iii). Rac-GTP up-regulation is similar (in both magnitude and timing) to reported experimentally (Tzima *et al.*, 2002). This appears to be due to rates determining binding of GEF_R to Rac-GDP and consequent Rac-GTP formation rather than the rate of GEF_R activation by Src, which (in the model) happens much faster.

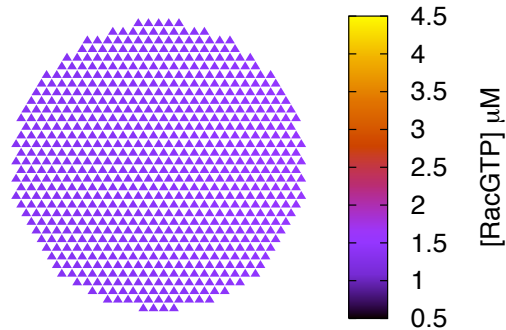


Figure 6.11: The effect on Rac-GTP distribution of allowing the Rac-GDP-GEF intermediary (reaction 6.4) to diffuse in the cytosol and on the membrane as opposed to just on the membrane as in figure 6.3. A localised pattern of activation is not generated.

slightly less than reported (Tzima *et al.*, 2002), however it does give a comparable time scale of activation. Interestingly the rates of GEF_R activation due to active Src reached new steady states relatively quickly, and it is actually the rates of reactions 6.4 and 6.5 which are the rate limiting ones (note in figure 6.10 that the Rac GAP is very slightly down-regulated. This is a balance between increased Rac-GTP-GAP complexes and decreased GAP activation by Rho-GTP).

The pattern of Rac activation (figure 6.9) is generated by localised Src activation, however it is maintained due to mutual Rho and Rac inhibition (though with removal of this cross talk a similar, though less distinct, pattern to figure 6.9 occurs - not shown) and slow diffusion of the active membrane bound Rac-GTP. It is also crucial that the RacGDP-GEF intermediary is membrane bound. Figure 6.12 shows the same equations solved whilst taking this intermediary as diffusing both on the membrane and in the cytosol. With this higher diffusion rate, of this relatively short lived intermediary, the Rac activation pattern is destroyed. Interestingly the whole cell measure of Rac activation (figure 6.12) is broadly similar to figure 6.10, suggesting that, in this case at least (and presumably in the case of cell migration), whole cell profiles of activation characterise the system poorly. Hence there is a need for experiments that can quantify local activation.

Previous experimental work has shown activation of Rac and inhibition of Rho returning to basal levels after an extended period of time (Tzima *et al.*, 2001, 2002; Wojciak-Stothard & Ridley, 2003). In this model there is no feedback, so the new steady states are maintained. However it is not necessarily the case that there must be direct bio-

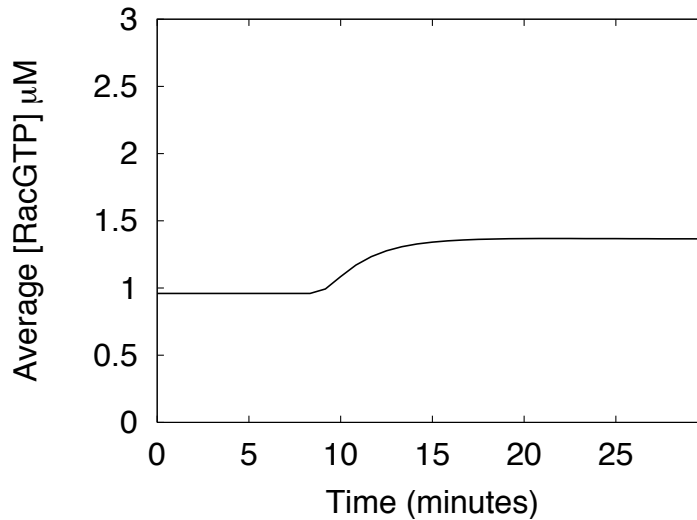


Figure 6.12: The effect of allowing the RacGDP-GEF intermediary (reaction 6.4) to diffuse in the cytosol and on the membrane as opposed to just on the membrane as in figure 6.9. The average [Rac-GTP] is similar to figure 6.10.

chemical feedback. To investigate the hypothesis that a change in cell morphology could lead to a different mechanical signal the same equations (including the Stokes equation for the fluid flow) were solved on two further morphologies; one parallel to the flow and one perpendicular to the flow, so the equation for the cell surface, equation 4.56, was modified from $a = b = 1$ to $a = 0.333, b = 3$ (parallel) and $a = 3, b = 0.333$ (perpendicular). These three different morphologies have comparable volumes and surface areas.

Rac activation for these different shapes can be seen in figures 6.13 and 6.14. Figure 6.15 suggests it maybe the case that the change in morphology itself is enough to damp the system back to basal levels, i.e. as the cell polarises the signal from the flow is reduced. This effect may be attenuated by clustering of integrins; if they are localised in focal adhesions then the position of them could be important. For example in a cell orientated as in figure 6.13 the mechano-transducer in FAs will only become activated if the FA is near the downstream edge of the cell, which is unlikely. However in a cell orientated as in figure 6.14 more FAs will be in regions where they will become activated.

The results from the different morphologies are further evidence for the normal force on

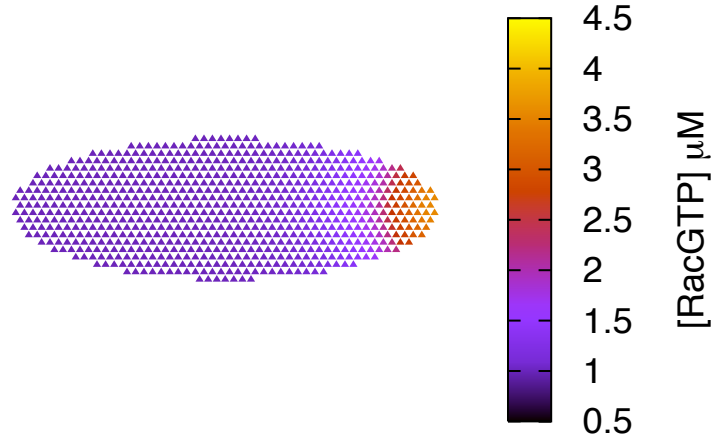


Figure 6.13: Activation of Rac is decreased in a cell aligned parallel to the flow (left to right). Figure 6.15 compares average Rac activation over three cells of differing orientation to the flow.

the cell surface playing an important role in this process, for although Rac activation (in the model) is responsive to the flow orientation the shear stress (both total and maximum) on the cell is not (figures 4.10 and 4.11). **Although a flattening of the cell may attenuate the EC response by a shear-stress mediated pathway Barbee *et al.* (1994).**

Figure 6.16 shows Rho inhibition across the cell, which is similar to experimental observations (Tzima *et al.*, 2001). The concentration distribution of Rho-GTP is more diffuse (not shown) than the Rac-GTP distribution, Src activates GAP_{ρ} locally, however because diffusion of the GAP occurs relatively quickly the local deactivation is spread.

Some experiments report rapid transient activation of Rho (Wojciak-Stothard & Ridley, 2003), which could be mediated through one of the different mechanisms of mechanical transduction mentioned (section 5.1). This observation also highlights a complication in the parameter choices: even with rapid Rho GEF activation (which is not modelled here) corresponding GTPase activation would be slower than reported by Wojciak-Stothard & Ridley (2003) for transient Rho activation. It may be that the parameters for different GEFs and GAPs are highly variable (a mechanism the cell could employ in regulating the time-scale of GTPase activation), or fast activation of a GEF coupled with GAP inhibition might speed up the GTPase response (although this would actually increase the level of GTPase activation).

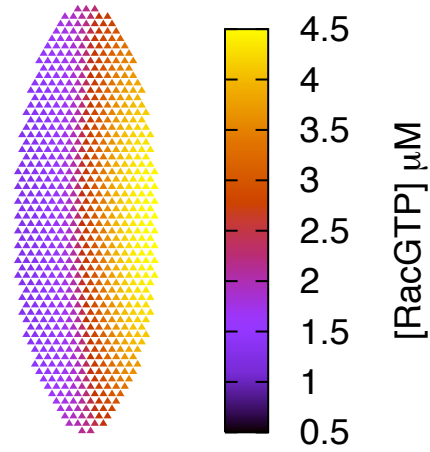


Figure 6.14: Activation of Rac is increased in a cell aligned perpendicular the flow (left to right).Figure 6.15 compares average Rac activation over three cells of differing orientation to the flow.

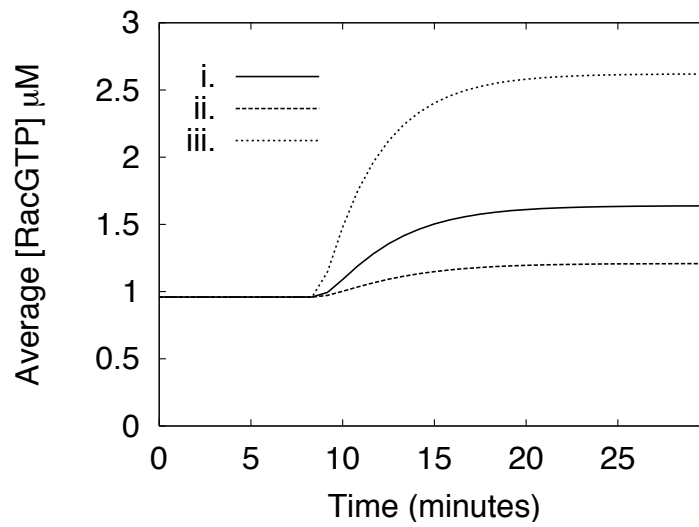


Figure 6.15: Whole cell average of Rac activation in three different morphologies; circular (i), perpendicular to flow (ii) and parallel to flow (iii).

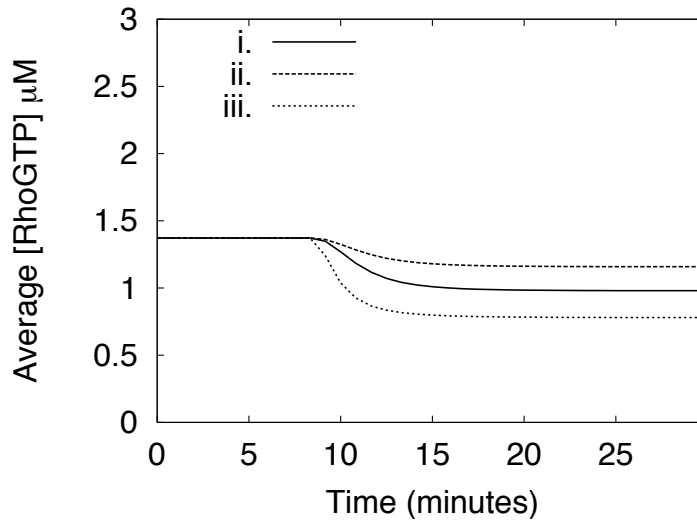


Figure 6.16: Whole cell average of Rho inactivation in three different morphologies; circular (i), perpendicular to flow (ii) and parallel to flow (iii).

It is almost certainly the case that other mechanisms contribute to localised Rac-GTP upregulation, but this modelling has clearly demonstrated that this pathway could give rise to the observed downstream Rac activation. It is also likely that a change in morphology could down-regulate the signalling network.

This model represents a plausible pathway whereby ECs interpret flow direction and mediate the correct response. Time courses for whole cell averages match experimental data, and the pattern of Rac activation is qualitatively similar to reported (Tzima *et al.*, 2002). As might be expected, both biologically and mathematically, the model is sensitive to the ratios of active to inactive GAPs and GEFs. Unfortunately experimental data is not available for *in vivo* time courses of Rho and Rac GEFs and GAPs in ECs responding to fluid flow, however this does give a testable prediction that the Rac GEF should be quickly activated (within 1-2 minutes, figure 6.10) so that conversion from Rac-GDP to Rac-GTP is not rate limited and gives the observed characteristic time scale of activation. If future experiments did not illustrate this then it would (assuming the parameters governing the Rac-GDP and Rac GEF reaction are characteristic) suggest that it is inhibition of the Rac GAP that leads to Rac activation.

7 Conclusion

In this chapter the research reported in this thesis is reviewed, with particular emphasis on the questions raised at the beginning of this report.

The mathematical modelling of actin stress fibre alignment (chapter 2), lamellipodia formation (chapter 3), fluid flow (chapter 4), mechanical transduction (chapter 5) and Rho GTPases (chapter 6) has formed the author's own hypothesis regarding how ECs polarise and elongate in the direction of fluid flow which is put forward as the conclusion to this thesis.

7.1 Project Goals

In the introduction to this project several points were raised, section 1.2. The modelling presented in the preceding sections has elucidated answers to these questions. Here those questions are recalled and the conclusions related to them summarised.

Which cell component interprets physical force?

The modelling of chapter 4, 5 and 6 has focused on the aspects of signalling which give rise to EC polarity, in this section the focus is the same.

The model of flow over a cell suggests that there must be a cell component that can transduce a mechanical force that acts normal to the cell surface. This is because the heterogeneous pattern in signalling suggests a response to a heterogeneous pattern of force. The shear stress on the cell surface is symmetric with respect to the up and downstream edges, indicating the cell must respond to the force normal to the surface in order to determine flow direction. However, a shear-stress activated pathway is still presumed to be crucial to EC alignment, as early EC signalling events in response to fluid flow include calcium influx and potassium channel activation (Ballerman *et al.*, 1998; Davies, 1995; Yamamoto *et al.*, 2000). Ion channel signalling may be activated by a stretching of the channel (Hoger *et al.*, 2002). However the precise mechanism of shear stress activation of ion channels remains unclear (Barakat *et al.*, 2006).

In the author's opinion the best candidate to respond to the normal force is integrins and their associated complexes. They are known to contain components which become

activated in response to tension (for example p130 Cas has been shown to become activated in response to mechanical stretching (Sawada *et al.*, 2006)). and one of their constituents, Src, has been shown to be able to activate guanine nucleotide exchange factors (GEFs) and GTPase activating proteins (GAPs) which are crucial in Rho GTPase regulation (Arthur *et al.*, 2000; Garrett *et al.*, 2007). The model of force deformation of integrin complexes suggests, for a physiological flow, that the extension of the complex is of the order of tens of nm - a feasible length for altered binding characteristics. Note that the 'window of opportunity' for this prediction is quite slim, an order of magnitude smaller and the extension would be competing with random brownian motion of the complex, and an order magnitude larger would mean an extension larger than the complex itself.

For this hypothesis it was assumed that the mechano-transducer could respond to normal forces. This assumption needs further study, although it is plausible for a mechano-transducer in the integrin complexes to respond to normal forces.

Furthermore it is not immediately clear that a normal force applied to the surface necessarily results in a normal force at the basal surface. Force on the surface is borne by the cytoskeleton which, ultimately, is attached to the ECM at FAs. The exact relationship between forces on the surface as a whole and forces at FAs is not clear. In this work adhesion to the ECM was assumed to be homogeneous rather than at discrete points of attachment, hence it was natural to assume that the force on the surface and cytoskeleton was transferred directly to the basal surface.

The effect of modelling the load on stress fibres and FAs due to fluid flow is unexplored, and would require some careful implementation. It may be possible to calculate the force on FAs by summing the contributing forces from smaller cytoskeletal units. For example the fluid causes a force on the surface of the glycocalyx which is transferred (according to the hypothesis by Thi *et al.* (2004)) to the cortical web of actin beneath the cell surface, which is attached to stress fibres. In a cell responding to fluid flow the force a stress fibre bears would be dependent on its position in the cell and the density of stress fibres at that point (more stress fibres would reduce the load borne by each individual fibre).

Another complication for the mechanical transduction model arises from consideration of internal forces in the cell, the most significant of which is tension arising from myosin induced stress fibre contraction. The fluid flow model predicts surface forces of the order of $1 \text{ pN } \mu\text{m}^{-2}$ and a single myosin can generate several pN of force, so the two

may be comparable. If the density of stress fibres terminating at the actin cortical web is, for example, $0.5 \mu\text{m}^{-2}$, then each stress fibre would bear ≈ 2 pN force (to balance the $1 \text{ pN } \mu\text{m}^{-2}$ surface force). Hence it may be the case that a mechano-transducer confuses internal and external forces. However, it has been observed (Tzima *et al.*, 2001) that stress fibres are initially disassembled in response to fluid flow (presumably in response to a global signal, possibly from stretch activated ion channels). This lowers stress fibre density, and hence any remaining stress fibres bear a larger proportion of the surface force and a mechano-transducer can establish polarity appropriately.

Improving the modelling of mechano-transduction, and in particular how the force on the surface relates to the force at discrete points of attachment is a direction of future research. There are several other directions that this work could be taken in, these ideas are briefly explored in the next and final chapter of this thesis.

How does this component initiate signalling?

Components of integrin complexes are known to respond to force. However the exact nature of the mechano-transduction is unclear. Src, a tyrosine kinase associated with integrins, has been shown to be quickly activated in response to force (Wang *et al.*, 2005). Src has also been shown to regulate both GAPs and GEFs, hence (in this context) it could play a key role in linking Rho GTPase regulation with force. In this work Src was taken as a biochemical measure of EC response to force and hypothesised to link directly to Rac GEF and Rho GAP activation

This hypothesis was tested with a simple model of Rho GTPase cross-talk and cycling (between GTP and GDP bound forms). Modelling showed that this hypothesis could lead to GTPase activation comparable to the reported levels for whole cell averages and qualitatively similar to regions of activation of Rac. In principle this hypothesis could be valid in an alternate form with a different ‘read out’ from integrin complex signalling and a different link between GEFs and GAPs and the mechano-transducer.

How is polarity established and maintained?

Modelling has supported a hypothesis of spatial heterogeneity arising from ECs responding to the normal force on a cell, leading to local activation of Src, Rac GEF and Rac GTP (figures 5.7 and 6.9 show the model prediction of active Src and Rac

GTP distribution in an EC responding to fluid flow). Modelling has also shown that association to the cell membrane is crucial in maintaining this local signalling as this limits diffusion. Relaxing the condition of the Rac-GEF intermediary being bound to the membrane is enough to destroy the pattern of activation. It may be that this is a standard mechanism employed by cells, in different contexts, to generate local signalling. Although other methods to do this (by establishing a bi-stability for example) are possible.

How could this hypothesis, that Src activates a Rac GEF, be verified? One possibility is tracking Rac GEF and Rac GAP activation experimentally (although the exact Rac GEFs and GAPs involved in this context are not known and may be numerous). This model predicts that GEF activity should be upregulated in the downstream region and that (due to the faster diffusion of GAPs) it cannot be the case that Rac activation is due to GAP inhibition because then activation would not be restricted to this region. If experiments reported GAP inhibition in the absence of GEF activation then it would suggest there must be a more complicated mechanism for maintaining polarity other than local activation and limited diffusion.

The proposed mechanism of maintaining polarity is slightly different from that suggested in migrating cells, where separate zones of activation are proposed to be maintained by: mutual inhibition of signalling agents or whole pathways (Narang, 2006); a bi-stable system bifurcating into two stable states spatially separated (Jilkine *et al.*, 2007) and/or a local excitation global inhibition (LEGI) type mechanisms (Levine *et al.*, 2006). The latter of these is reminiscent of the case here and indeed the model by Levine *et al.* (2006) included a membrane bound activator and cytosolic inhibitor. The inhibitor can attach to the membrane where it can switch off the activator, similar to the Rho GTPase model (chapter 6) where the GAP can attach to the membrane and induce conversion from a GTP bound state to GDP bound state.

How is cytoskeleton reorganisation mediated?

There are two important components to cytoskeleton reorganisation in non-confluent layers of ECs responding to fluid flow, lamellipodia formation in downstream signalling regions and stress fibre alignment.

The modelling in chapter 3 illustrated that *de novo* polymerisation nucleated by Arp2/3 could lead to extension of the membrane and supported the Brownian ratchet hypothe-

sis of polymerisation inducing force. The model also suggested that the polymerisation of actin into branched structures must be closely regulated if actin is to be continually polymerised and a consistent force provided. One of the ways to do this is for the network to be severed consistently to provide a pool of actin monomers available for new polymerisation. In the BD model of membrane extension (chapter 3) regular severing of the network stopped the membrane extension from stalling. Capping of the filaments was also necessary to generate a network of branched actin filaments qualitatively similar to the *in vivo* case. The exact significance of the branched network and the distinctive angle that Arp2/3 nucleates new filaments at is not known. It may be that generation of the tree like structure is important in providing a force over a broad area of membrane, in contrast to filopodium formation.

It was argued in chapter 2 (section 2.2.3) that stress fibre alignment could not occur as a result of isotropic polymerisation, but filaments could spontaneously align in response to certain biological signals, for example up-regulation of a bundling protein. In the absence of any external cues, alignment occurs in a direction dependent on random noise (according to the model, section 2.2.3), but it was suggested that directed polymerisation nucleated by formins could provide a bias to promote alignment in the flow direction.

How is the signalling network shut off?

In section 6.3 it was demonstrated that the model (mechano-transduction of the force due to fluid flow and Rho GTPase activation) could respond to different cell morphologies - Rac GTP activation was less (on average) in a geometry aligned with the flow. Maximum shear stress and total shear were the same for geometries of cells of the same surface area, regardless of the orientation with respect to the flow (figures 4.10 and 4.11). Hence it may be the case that a change in cell morphology diminishes the effect of signalling in the downstream region. However, after long term exposure to shear-stress ECs flatten, which does reduce the total and maximum shear on their surface (Barbee *et al.*, 1994).

This property of the model may be attenuated by considering the effect of forces being borne by discrete adhesions sites: In the model mechano-transducers that become activated up-regulate Src in response to the normal force on the surface directly above them, in reality the force on a region is likely to be borne by the surrounding FAs (as in the decentralised model of mechano-transduction Davies (2008)). Hence for a FA

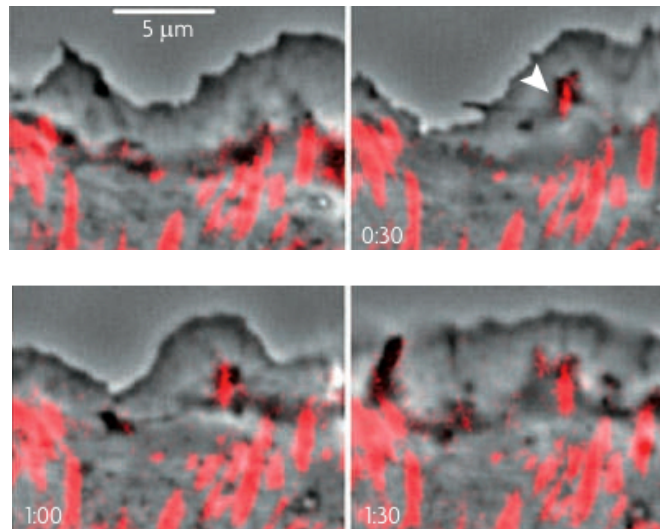


Figure 7.1: Maturation and locality of FAs, reproduced (and modified) from Alexandrova *et al.* (2008). Phase contrast image of rat fibroblasts superimposed with a fluorescence image of nascent and mature FAs tagged with YFP-paxillin (red). Nascent FAs (arrow) form underneath the lamellipodia, mature FAs define a distinct region (the lamellum) behind the lamellipodia (Alexandrova *et al.*, 2008). Time (top left, top right, bottom left and bottom right): 0, 30 s, 1 min, 1 min 30 s.

to become activated it would have to be in a region that is under sufficient tension on average, rather than locally sufficient tension. It may be that mature FAs are less likely to be located in a down-stream region in a cell aligning via lamellipodial extension, figure 7.1.

In response to fluid flow endothelial cells extend and flatten to approximately 50% of their original height (Barbee *et al.*, 1994). This flattening will clearly reduce the maximum and total shear stress on the cell. Hence it is interesting that in the model of an aligned cell, which in the model has the same maximum height, the cell does have attenuated signalling, figure 6.15. It may be the case that this attenuation is superfluous, and that reducing the shear stress signal (by flattening) is sufficient for a cessation of signalling. A time course of EC height following the onset of fluid flow may establish whether the additional attenuation, due to planar morphology, is necessary.

It is suggested, (Ballerman *et al.*, 1998), that ECs stiffen and adhere more strongly to the substratum (presumably through increase in number or size of FAs). This would effectively reduce the load on each FA, and attenuate force induced FA signalling. Al-

though others have shown very clearly that the adhesion area of cells subjected to flow and no flow remains within 10% of initial values in both cases (Davies *et al.*, 1994), so morphology rather than altered adhesion appears to be a better candidate to attenuate signalling. However Davies *et al.* (1994) also showed that formation and loss of FAs was highly dynamic, and ultimately led to FAs aligning in the flow direction (presumably correlated with stress fibre alignment), this alignment may lead to a stiffening of the cell in the direction of fluid flow. This maybe a more attractive hypothesis for attenuation of EC signalling in response to fluid flow: if signalling is shut-off by a flattening of the cell then a flattened EC will not re-align with flow in a different direction (it is 'flat' in all directions), but if signalling is attenuated by planar morphology or the stiffness properties of the cell then a change in flow direction could still lead to signalling. However, it should be noted that it is most likely that all these factors act co-operatively in the EC signalling response.

7.2 Endothelial Cell Polarisation and Elongation: A Hypothetical Overview

In this section the process of EC alignment in the direction of fluid flow is described with emphasis on the aspects of the process that the modelling in this project has provided new or supported existing hypotheses. For clarity references and competing hypotheses that have been discussed in this (and previous) chapters are not repeated here.

Flow over an EC either *in vivo* (in large arteries at least the flow is quasi-steady Hazel & Pedley (2000)) or *in vitro* is well characterised by Stokes flow, which represents steady, viscous flow. This flow exerts a force, \mathbf{f} , on the surface. In terms of the boundary integral representation of the flow, equation 4.48, $-\mathbf{f}$ weights the Green's function and ensures that the boundary condition (no flow on the surface) is satisfied. Solution of equation 4.48 requires determination of the value of \mathbf{f} over the cell surface.

It is apparent (figure 4.15) that the normal force may play a role in establishing polarity in ECs as it is negative (with respect to the z-axis) in the upstream region and positive in the downstream region.

This observation favours a hypothesis of polar signalling resulting from FAs, which become activated only in the downstream regions of the cell, and hence establish polarity. It is likely that several components of FAs can respond to force, however the precise

nature of the mechanism is not known. It is known that the FA associated tyrosine kinase Src can respond rapidly to mechanical force and is activated in response to fluid flow. Src has also been shown to activate GEFs and GAPs for Rac and Rho, and hence may play a role in linking mechano-transduction with cytoskeleton regulators.

Inhibition of Rho initiates stress fibre disassembly (myosin II activity drops and lowers the tension needed to maintain the fibres) which may amplify the signal to mechano-transducers. An increase in tension in the downstream edge up-regulates formin induced actin polymerisation, and provides the directional bias required for stress fibre alignment.

Activation of Rac induces lamellipodium formation and mediates Arp2/3 activation as well as severing of actin filaments. Arp2/3 binds onto the side of existing filaments and forms a binding site homologous to the barbed end of actin. Polymerisation induces a force on the membrane via a Brownian ratchet mechanism: as the membrane and filament undergo brownian motion, space for monomer addition becomes available, and the membrane gets ratcheted forward. This leads to a change in cell morphology and, along with stress fibre alignment, alignment of the EC.

The signalling network may be attenuated by a change in height (Ballerman *et al.*, 1998) and/or the planar dimensions of the EC (figure 6.15). However it may also be the case that the change in internal structure (for example FA and stress fibre alignment) reduces mechano-transduction.

7.3 Experimental Evidence and Model Validation

The model of EC response to fluid flow (chapters 4, 5 and 6) has three key components: response to the force normal to the surface, Src activation (as a marker for FA signalling) and Rac activation at the leading edge.

The mechano-transduction model (chapter 5) assumed the force normal to the surface acted on a mechano-transducer. This is an attractive hypothesis because it naturally gives rise to upstream and downstream signalling regions without having to make assumptions about pre-aligned cytoskeletal or membrane structures. This hypothesis is assumed complementary (and not contradictory) to the usual paradigm of ECs responding to the force parallel to their surface. An experiment to distinguish the effect of each component is difficult to conceive, because in reality, at the intra-cellular level, the effect of these two force components is likely to be confounded - it is hypothesised that

the force at the cell surface is decentralised to different mechano-transducers, such as FAs and PECAM-1 (Davies, 2008). For example, Mathur *et al.* (2000) illustrated that application of an approximately normal force (to the apical surface) can lead to a global re-organisation of cellular adhesion. Mathur *et al.* (2000) ascribe this response to the re-distribution of the local nN force they applied through the cytoskeleton and consequently across the cell. However, given that points of adhesion are well known to be signalling hubs (Sastry & Burridge, 2000; Katsumi *et al.*, 2004) this may be a result of transduction of local force into global signalling. In contrast to this it has been shown that elastic deformation is strongly screened at distances more than several μm (Bausch *et al.*, 1998). This, once again, suggests that the complicated material properties of the cell need to be carefully considered when considering the transduction of force across the cell.

Traditionally the EC response to fluid flow is referred to as a shear stress activated process (Goldfinger *et al.*, 2008; Tzima *et al.*, 2001, 2002, 2005; Wojciak-Stothard & Ridley, 2003; Hoger *et al.*, 2002). Semantically (on the scale of an individual cell), this may prove to be only part of the story. The author is aware of no experiments which can de-couple the effects of parallel and normal components of force on the cell. Separately applying normal and parallel forces is clearly possible, however in this case the difficulty lies in understanding how these forces distribute throughout the cell. This ‘de-centralization’ of the force, (Davies, 2008), is a hugely interesting avenue of further research. As discussed above the assumption that the normal force on the surface gets transferred directly to the basal surface (chapter 5) is a huge simplification, clearly shear forces will be transduced to FAs as well. However as an area of future research, a more realistic, carefully constructed and experimentally supported, model of mechano-transduction could be supplanted into this modelling framework (chapters 4, 5 and 6) very easily.

The role of shear-stress should not be underplayed. There is excellent evidence for a direct response to shear-stress, for example Yamamoto *et al.* (2000) illustrate flux of Ca^{2+} ions (with an ATP concentration of 250 nM/L) increases step-wise for step-wise increases in shear-stress.²¹ In this case the hypothesis of ion channels opening as a direct response to shear stress is the best and most attractive one. Furthermore as noted above, the transduction of shear forces throughout the cell could still give rise to signalling at FAs, cell-cell junctions (for example PECAM-1) as well directly acting on ion channels (possibly via the glycocalyx Thi *et al.* (2004)). I hypothesise that the

²¹Although, due to the approximate linearity of low-Reynolds number flow an increase in the magnitude of shear-stress corresponds to a proportional increase in the magnitude of the normal force.

role of shear-stress is complemented by the action of the normal force.

The hypothetical role I put forward for the force normal to the surface is to generate the polar response. In chapters 4, 6 and 5 a model of signal amplification and localisation (by limited diffusion) was described. It remains to be seen if this is the case. However, it may be that the effect of the normal force need only be very slight to establish polarity. In the case of chemotaxis (cell migration either up or down a chemical gradient) the chemical gradient need only be very shallow, hence the difference in concentration across the length of the cell is very small. The mechanism of how this very slight difference may lead to polarity (to migrate cells typically establish front and back signalling regions) has been extensively studied from a modelling perspective, reviewed by (Devreotes & Janetopoulos, 2003). A similar mechanism may be employed by ECs.

Integrins, a key component of FAs, have been shown to become activated in downstream signalling regions of ECs (Goldfinger *et al.*, 2008), this supports the hypothesis of polarity arising from FA signalling. Although it should be noted Goldfinger *et al.* (2008) hypothesise this activation as arising from PECAM-1 signalling via phosphoinositide 3-kinases (PI3Ks), and not as a direct result of FA mechano-transduction. The role of this pathway is unclear, PI3Ks have been shown not to be necessary for EC polarisation and alignment (Wojciak-Stothard & Ridley, 2003), however (in the case of chemotaxis) it has been shown cellular polarity can be generated by parallel pathways (Chen *et al.*, 2007). In migrating cells PI3Ks respond to an external chemical gradient to establish polarity (Devreotes & Janetopoulos, 2003), in the case of ECs responding to fluid flow the external stimulus is the force on the cell. Precisely how the cell translates this stimulus into spatially localised activation remains an open question. However further experimental characterisation of the spatial-temporal dynamics of the EC response to fluid flow would elucidate which pathway establishes polarity. The modelling of this project has provided a quantitative and testable hypothesis.

Coupling of mechano-transduction to a model of Rho-GTPase signalling (chapter 6) leads to whole cell time courses (figures 6.10 and 6.16) that resembles experimental data (Tzima *et al.*, 2001, 2002). However, modelling has shown that whole cell averages of protein activity need to be applied judiciously. Figure 6.10 (plot i.) and figure 6.12 are comparable, yet the corresponding spatial distributions of Rac-GTP are not (figures 6.9 and 6.3). However, this hypothesis does make a prediction of whole cell averages from individual cells aligned perpendicular or parallel to the flow which, in principle, could be tested (figure 6.15).

More detailed data regarding gradients of Src and Rac-GTP in the downstream edge of ECs responding to fluid flow could be used to test the hypothesis of mechano-transduction and consequent Rac-GTP activation (biosensors for RhoA and Rac1 can now yield precise data on the spatial and temporal activation of GTPase (Pertz & Hahn, 2004)), in particular the Src gradient is predicted to be increasing (in the direction of flow) approximately linearly (figure 5.7).

However the conclusions of such an analysis would have to be carefully drawn. It may be the case that EC polarity is established by the force normal to their surface but that the simple approximation to force transduction through the cytoskeleton is a poor assumption.

If the stimulus from the flow model (chapter 4) is halted then the network modelled in chapter 6 returns to basal levels of activation. Hence it is interesting that the model predicts a change in morphology does inhibit signalling, for otherwise an elongated cell still responds to the flow. Some models of cell migration are self-sustaining, so that on removal of the initial stimulus the cell remains polarised and motile (Jilkin *et al.*, 2007). Hence an experiment that compares alignment of ECs after being in flow conditions for different periods (for example ECs left for 24h with the first 1h, 2h,...24h in flow conditions) would show whether a persistent stimulus is required for EC polarisation, elongation and/or alignment. It might aid investigation into how the network is inhibited; if the network remains active following the removal of the flow signal then it suggests the network must be inhibited by a feedback mechanism rather than the change in morphology.

It may be the case that further modelling will in itself validate the hypothesis proposed above. The next chapter briefly explores possible future research directions

8 Future Work

In this section future directions of research in this area is described. The research reported in the previous chapters has focused on the response to fluid flow of a single cell with a fixed surface. This section briefly explores: extending the flow model (coupled with mechano-transduction and Rho GTPase models) to multiple cells and modelling morphogenesis for both single and multiple cells.

Following this, other directions of future work are discussed (but not explored) including: coupling the BD model to the Rho GTPase model, modelling the signalling network in more detail and modelling the endothelium.

8.1 Multiple Cells

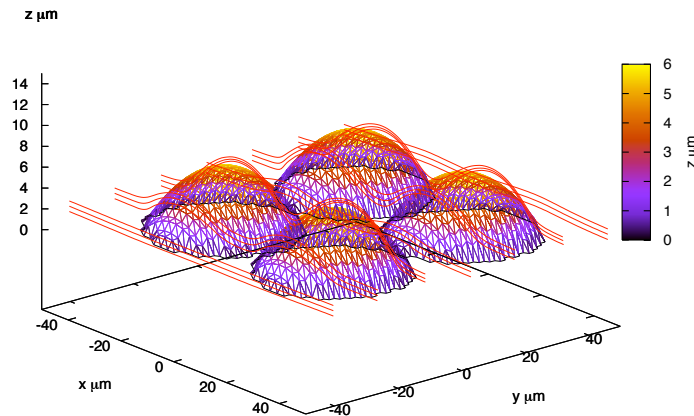


Figure 8.1: Streamlines (red lines) of the flow (in the increasing x direction) over four cells touching at their extremities. The streamlines flow over the cell (the impression otherwise is due to the method to used to generate the figure). Notice that the streamlines over the downstream cells are identical to the pattern over the upstream cells.

In vivo the fluid flows over the endothelium. The flow model (chapter 4) describes the force on the surface of a single cell attached to a planar surface. To investigate whether the fluid flow over the endothelium produces a different pattern the BIR representation (equation 4.48) was extended so that the surface P was the surface of four round cells

touching at their extremities.

Solving equation 4.48 in this new geometry (by applying the same method described in chapter 4) gives the force on each of the four cells as being identical to the force on a lone cell (figures 4.15-4.16). Figure 8.1 shows the streamlines in this geometry and illustrates that the incoming streamlines for downstream and upstream cells are identical. Hence the modelling of a single cell is also valid for cells in confluent layers. This was verified computationally (not shown) and gave identical results (for each cell) to those reported in chapters 4, 5 and 6.

However the mechanics of an EC elongating are different for cells in confluent layers. For example, in the model of membrane extension (chapter 3) the membrane was implicitly assumed to be extending into empty space - as oppose to a region occupied by a different cell. One way to consider the mechanics of whole cells and their associated morphogenesis is the cellular Potts methodology.

8.2 Cellular Potts Modelling

Cellular Potts Models (CPMs) describe the time evolution of cell morphology. To do this in 2D the plane is discretised into lattice sites (for example a hexagonal grid as employed in chapters 5 and 6). Each grid site i (in this case a hexagon) is assigned a state $\sigma(i)$. Here $\sigma(i) = 0$ refers to i being a grid site that is not part of any cell (i.e. ECM) and $\sigma(i) = m$, where m is an integer implies that the i^{th} site is in the m^{th} cell. Then the morphology of the m^{th} cell changes when grid sites change state to or from $\sigma = m$.

To govern the changing of states a Hamiltonian is constructed. This is not a Hamiltonian in the formal sense - it does not characterise the total energy of the system. However, in the case of a single cell, it is often considered to be the effective energy of the cell.

The standard definition of the Hamiltonian is (Anderson *et al.*, 2007):

$$H = \sum_{(i,j)} J_{\sigma(i),\sigma(j)} (1 - \delta(\sigma(i), \sigma(j))) + \lambda(a - A)^2. \quad (8.1)$$

The sum is over all (i,j) neighbour grid sites. The first term is the contribution to the effective energy of the cell boundary (where if $\sigma(i) \neq \sigma(j)$ then $J_{\sigma(i),\sigma(j)}$ is added to

the Hamiltonian). The dependence on $\sigma(i)$ and $\sigma(j)$ means that in principle cell-cell boundaries and cell-ECM boundaries can confer different energy to the Hamiltonian. The second term, $\lambda(a - A)^2$ quantifies the energy arising from the difference in the cell's area (a) and its target area, (A). So the Hamiltonian is large if the cell is large or small relative to A .

The dynamics of the CPM (how the states of the grid sites evolve over time) are governed by the Metropolis algorithm, which is:

- Select a grid site, i , at random.
- At random choose a site that neighbours site i , denote this neighbour by j .
- Calculate $\Delta H = H_f - H_i$, where H_f is calculated from equation 8.1 evaluated with the state of site j copied to the state of site i , hence $\sigma(i) = \sigma(j)$. and H_i is the Hamiltonian calculated before this copying.
- The copying (of the state of site j to the state of site i) is accepted with probability:

$$p(\sigma(i) \rightarrow \sigma(j)) = \begin{cases} 1 & \text{if } \Delta H \leq -H_b \\ e^{-(\Delta H + H_b)/T} & \text{if } \Delta H \geq -H_b \end{cases} \quad (8.2)$$

where T is the 'temperature' of the simulation and H_b represents the resistance of the membrane to force (Marè *et al.*, 2006). If the copying of states decreases the value of the Hamiltonian by more than H_b the copying is accepted, if not it is accepted with a probability that decreases exponentially for increasing ΔH . If the grid has N sites in total then N applications of this algorithm is defined as one Monte-Carlo time step (MCS).

Figure 8.2 illustrates the cell morphology generated by applying this algorithm and equation 8.1. Initially the cell shape was circular with area $1300 \mu\text{m}^2$. With $A = 1100 \mu\text{m}^2$ the final area reached is $1098 \mu\text{m}^2$ - so the cell shrinks. The CPM can also be applied to multiple cells (figure 8.3). In this case there are two values of the coupling constant: J_{ce} and J_{cc} . Where J_{ce} is the coupling energy between cell and ECM, and J_{cc} the coupling energy between two different cells. If $J_{cc} < J_{ce}$ then cell-cells binding is energetically favourable.

The Cellular potts approach is very flexible because the Hamiltonian can be modified to include other forces. For example Marè *et al.* (2006) modify the Hamiltonian to

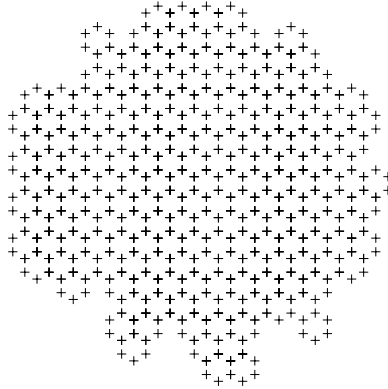


Figure 8.2: Cell morphology generated by the Metropolis algorithm and equation 8.1 after 1000 MCS. $H_b = 46 \mu\text{m}^{-1}$, $A = 1100 \mu\text{m}^2$, $T = 8 \mu\text{m}^{-1}$, $\lambda = 1$ and $J = 0.7 \mu\text{m}^{-1}$. J is the coupling energy between the cell and ECM.

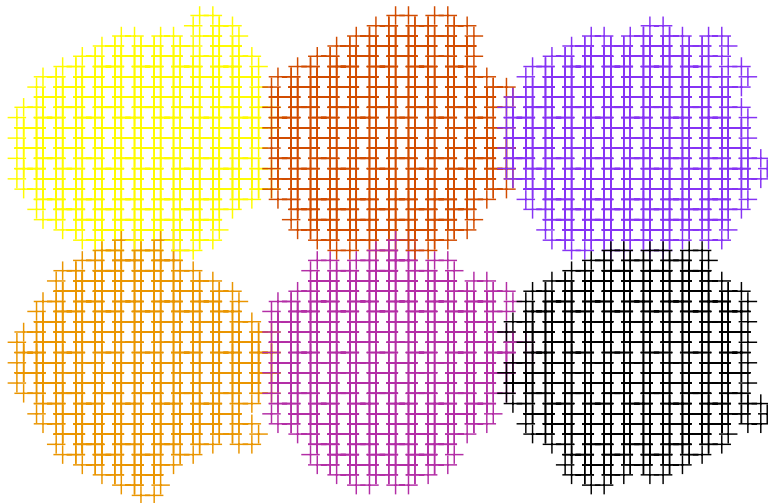


Figure 8.3: Cell morphology of six cells generated by the Metropolis algorithm and equation 8.1 after 1000 MCS. $H_b = 46 \mu\text{m}^{-1}$, $A = 1100 \mu\text{m}^2$, $T = 8 \mu\text{m}^{-1}$, $\lambda = 1$, $J_{ce} = 0.02 \mu\text{m}^{-1}$ and $J_{cc} = 0.02 \mu\text{m}^{-1}$. J_{ce} and J_{cc} are the coupling energies between cell-ECM and cell-cell respectively

include the effect of Rho and barbed ends by shifting ΔH :

$$\begin{aligned}\Delta H' &= \Delta H - P + \xi(\rho - \rho_{th}) && \text{- cell extension} \\ \Delta H' &= \Delta H + P - \xi(\rho - \rho_{th}) && \text{- cell retraction}\end{aligned}\quad (8.3)$$

where P is the force exerted by barbed ends pushing towards the membrane and ρ is the concentration of Rho, which causes contraction when it is above the threshold ρ_{th} and is weighted by the parameter ξ . With these shifts in ΔH the copying trial for copying of a cell state to an empty state (cell extension) it is more likely if P is high and copying of an empty state onto a cell state (cell retraction) is more likely if ρ is large. With this definition (and coupled models for P and ρ) Marè *et al.* (2006) generate a model for keratocyte migration.

In this case a CPM would have to be in 3D to dynamically evolve the three dimensional geometry (required as an input to the flow model). Furthermore, to bestow meaningful mechanical properties (to the virtual EC) a CPM would necessarily include modelling of FAs and FA turnover (so that the cell is more resistant to migration than the keratocyte migration model by Marè *et al.* (2006)).

8.3 Other Research Directions

One of the goals of this Ph.D. is to integrate models of different aspects of the EC response to fluid flow; in particular linking the mechanical force on the cell due to fluid with the network it activates.

The Rho GTPase aspect of this network is modelled in chapter 6 using partial differential equations. In principle, at least, it would be interesting to link that model with the stochastic model presented in chapter 3. However the linking of stochastic and differential models is a generically difficult problem, especially when the models are on totally different scales: the Rho GTPase model is on the scale of μm and minutes, whereas the BD model of membrane extensions is on the nm and μs scales. Hence (if there was a sensible connection between the two models) to run the models in parallel it would be necessary for simulations with a fold increase in computations of the order of hundreds of millions, which is clearly impractical!

Therefore to link these models a more pragmatic solution is necessary. Here the Langevin equation (3.1), is solved by Monte-Carlo simulation. A different and com-

putationally cheaper approach is to track the probability density function (pdf) of particles. This pdf then satisfies the Fokker-Planck equation, (Siegman, 1979).

This is a possible direction of future research. However, this would still present some significant technical and theoretical challenges. One of which would be how to interpret a model where the dynamics of interest occur on both the μs and minute time scales.

In this project a small portion of the signalling network is modelled in detail (chapter 6). Future work could model the network with wider scope. Of particular interest would be inclusion of ion channel signalling, modelling of which may validate the hypothesis of EC polarisation being due to a response to the force normal to the cell surface.

The approach here could also be extended to modelling the endothelium using a cellular Potts model. A model of the endothelium would aid further investigation into the pathogenesis of atherosclerosis.

References

- Abraham, V., Krishnamurthi, V., Taylor, D. L. & Lanni, F. 1999. The actin-based nanomachine at the leading edge of migrating cells. *Biophysical Journal*, 77, 1721–1732.
- Alberts, B., Johnson, A., Walter, P., Lewis, J., Raff, M. & Roberts, K. 2008. *Molecular Biology of the Cell*. 5 rev. edition. edition, Garland Publishing Inc, US;.
- Alexandrova, A. Y., Arnold, K., Schaub, S., Vasiliev, J. M., Meister, J.-J., Bershadsky, A. D. & Verkhovsky, A. B. 2008. Comparative dynamics of retrograde actin flow and focal adhesions: formation of nascent adhesions triggers transition from fast to slow flow. *PLoS Computational Biology*, 3 (9), 1–9.
- Allen, R. 2005. *The Mathematical Modelling of Morphological Changes in Endothelial Cells in Response to Fluid Flow by Considering the Effect of Mechanical Pressure on the Cell*. Mres thesis UCL.
- Amann, K. J. & Pollard, T. D. 2001. The arp2/3 complex nucleates actin filament branches from the side of pre-existing filaments. *Nat. Cell. Biol.* 3, 306–310.
- Anderson, A. R., Chaplain, M. A. & Rejniak, K. A., eds 2007. *Single-Cell-Based Models in Biology and Medicine*. Birkhäuser.
- Arbel, Y., Dvir, D., Feinberg, M. S., Beigel, R. & Shechter, M. 2007. The association between right coronary artery morphology and endothelial function. *International Journal of Cardiology*, 115, 19–23.
- Arthur, W., Petch, L. & Burridge, K. 2000. Integrin engagement suppresses rhoa activity via a c-src dependent mechanism. *Current Biology*, 10, 719–722.
- Ballerman, B., Dardik, A., Eng, E. & Liu, A. 1998. Shear stress and the endothelium. *Kidney International*, 67 (54), 100–108.
- Barakat, A., Lieu, D. K. & Gojova, A. 2006. Secrets of the code: do vascular endothelial cells use ion channels to decipher complex flow signals? *Biomaterials*, 27, 671–678.
- Barbee, K. A., Davies, P. F. & Lal, R. 1994. Shear stress-induced reorganization of the surface topography of living endothelial cells imaged by atomic force microscopy. *Circ. Res.* 74 (1), 163–171.

- Bausch, A., Ziemann, F., Boulbich, A., Jacobson, K. & Sackmann, E. 1998. Local measurements of viscoelastic parameters of adherent cell surfaces by magnetic bead microrheometry. *Biophysical Journal*, 75, 2038–2049.
- Bengtsson, H. & Eden, P. 2003. A simple model for the arterial system. *Journal of Theoretical Biology*, 221 (3), 437–43.
- Berliner, J. A., Navab, M., Fogelman, A. M., Frank, J. S., Demer, L. L., Edwards, P. A., Watson, A. D. & Lusic, A. J. 1995. Atherosclerosis: basic mechanisms. *Circulation*, 91, 2488–2496.
- Blake, J. 1971. A note on the image system for a stokeslet in a no-slip boundary. *Proc. Comb. Phil. Soc.* 70 (303-310).
- Bos, J., Rehmann, H. & Wittinghofer, A. 2007. GEFs and GAPs: critical elements in the control of small G proteins. *Cell*, 129 (5), 865–877.
- Boureux, A., Vignal, E., Faure, S. & Fort, P. 2007. Evolution of the rho family of ras-like gtpases in eukaryotes. *Mol. Biol. Evol.* 24 (1), 203–216.
- Britton, N. 2003. *Essential Mathematical Biology*. Springer.
- Butler, P., Norwich, G., Weinbaum, S. & Chien, S. 2001. Shear stress induces a time- and position-dependent increase in endothelial cell membrane fluidity. *Am. J. Physiol. Cell Physiol.* 280, C962–969.
- Carlsson, A. 2001. Growth of branched actin networks against obstacles. *Biophysical Journal*, 81 (4), 2907–2918.
- Carlsson, A. 2003. Growth velocities of branched actin networks. *Biophysical Journal*, 85 (2907-2918).
- Chang, L. & Goldman, R. 2004. Intermediate filaments mediate cytoskeletal crosstalk. *Nature Reviews Molecular Cell Biology*, 5, 601–613.
- Chen, L., Iijima, M., Tang, M., Landree, M. A., Huang, Y. E., Xiong, Y., Iglesias, P. A. & Devreotes, P. N. 2007. PlA2 and pi3k/pten pathways act in parallel to mediate chemotaxis. *Development Cell*, 12 (4), 603–614.
- Chiu, Y.-J., McBeath, E. & K.Fujiwara 2008. Mechanotransduction in an extracted cell model: fyn drives stretch- and flow-elicited pecam-1 phosphorylation. *Journal of Cell Biology*, 182 (4), 753–763.

- Civelekoglu, G. & Edelstein-Keshet, L. 1994. Modelling the dynamics of f-actin in the cell. *Bulletin of Mathematical Biology*, 56 (4), 587–616.
- Civelekoglu, G., Tardy, Y. & Meister, J. 1998. Modeling actin filament reorganization in endothelial cells subjected to cyclic stretch. *Bulletin of Mathematical Biology*, 60, 1017–1037.
- Civelekoglu-Scholey, G., Orr, A., Novak, I., Meister, J.-J., Schwartz, M. & Mogilner, A. 2005. Model of coupled transient changes of Rac, Rho, adhesions and stress fibers alignment in endothelial cells responding to shear stress. *Journal of Theoretical Biology*, 232, 569–585.
- Clark, K., Langeslag, M., Figdor, C. G. & van Leeuwen, F. N. 2007. Myosin II and mechanotransduction: a balancing act and mechanotransduction: a balancing act. *Trends Cell Biology*, 17 (4), 178–86.
- Cooper, J. & Schafer, D. 2000. Control of actin assembly and disassembly at filament ends. *Current Opinion in Cell Biology*, 12, 97–103.
- Craig, S. & Chen, H. 2003. Lamellipodia protrusion: moving interaction of vinculin and arp2/3. *Current Biology*, 13 (R236-R238).
- Davies, P. 1995. Flow-mediated endothelial mechanotransduction. *Physiol. Rev.* 75 (519-569).
- Davies, P., Barbee, K., Volin, M., Robotewskyj, A., Chen, J., Joseph, L., Griem, M., Wernick, M., Jacobs, E., Polacek, D., Depaola, N. & Barakat, A. 1997. Spatial relationships in early signalling events of flow-mediated endothelial mechanotransduction. *Annu. Rev. Physiol.* 59, 527–549.
- Davies, P., Robotewskyj, A. & Griem, M. 1994. Quantitative studies of endothelial cell adhesion: directional remodelling of focal adhesion sites in response to flow forces. *J. Clin. Invest.* 93, 2031–2038.
- Davies, P. F. 2008. Hemodynamic shear stress and the endothelium in cardiovascular pathophysiology. *Nature Clinical Practice Cardiovascular Medicine*, 6 (16-25).
- Dawes, A., Ermentrout, G., Cytrynbaum, E. & Edelstein-Keshet, L. 2006. Actin filament branching and protrusion velocity in simple 1d model of a motile cell. *Journal of Theoretical Biology*, 242 (2), 265–279.
- Dembo, M. 1986. The mechanics of motility in dissociated cytoplasm. *Biophysical Journal*, 50 (6), 1165–83.

- Dembo, M. & Harlow, F. 1985. Cell motion, contractile networks, and the physics of interpenetrating reactive flow. *Biophysical Journal*, 50, 109–121.
- DerMardirossian, C. & Bokoch, G. 2005. GDIs: central regulatory molecules in rho GTPase activation. *Trends Cell Biol.* 15 (7), 356–363.
- Detimary, P., den Berghe, G. V. & Henquin, J.-C. 1995. Concentration dependence and time course of the effects of glucose on adenine and guanine nucleotides in mouse pancreatic islets. *The Journal of Biological Chemistry*, 271 (34), 20599–20565.
- Devreotes, P. & Janetopoulos, C. 2003. Eukaryotic chemotaxis: distinctions between directional sensing and polarization. *The Journal of Biological Chemistry*, 278 (23), 20445–20448.
- Evangelista, M., Pruyne, D., Amberg, D. C., Boone, C. & Bretscher, A. 2002. Formins direct arp2/3-independent actin filament assembly to polarize cell growth in yeast. *Nature Cell Biology*, 4 (3), 260–9.
- Fleming, I., Fisslthaler, B., Dixit, M. & Busse, R. 2005. Role of pecam-1 in the shear-stress-induced activation of akt and the endothelial nitric oxide synthase (enos) in endothelial cells. *Journal of Cell Science*, 118 (18), 4103–4111.
- Footer, M. J., Kerssemakers, J. W. J., Theriot, J. A. & Dogterom, M. 2007. Direct measurement of force generation by actin filament polymerization using an optical trap. *PNAS*, 104, 2181–2186.
- Fuller, B. 1961. Tensegrity. *Portfolia Art News*, 4, 112–127.
- Fuß, H., Dubitzky, W., Downes, C. & Kurth, M. 2007. Deactivation of Src family kinases: hypothesis testing using a monte carlo sensitivity analysis of systems-level properties. *Journal of Computational Biology*, 14 (9), 1185–1200.
- Garrett, T., Buul, J. V. & Burrige, K. 2007. VEGF-induced Rac1 activation in endothelial cells is regulated by the guanine nucleotide exchange factor Vav2. *Experimental Cell Research*, 313, 3285–3297.
- Gautam, M., Shen, Y., Thirkill, T., Douglas, G. & Barakat, A. 2006. Flow-activated chloride channels in vascular endothelium. *The Journal of Biological Chemistry*, 281 (48), 36492–36500.
- Geigent, E., Ladizhansky, K. & Mogilner, A. 1998. An integrodifferential model for orientational distributions of f-actin in cells. *J. Appl. Math.* 59 (3), 787–809.

- Geiger, B. & Bershadsky, A. 2001. Assembly and mechanosensory function of focal contacts. *Current Opinion in Cell Biology*, 13, 584–592.
- Geiger, B., Bershadsky, A., Pankov, R. & Yamada, K. M. 2001. Transmembrane extracellular matrix-cytoskeleton crosstalk. *Nature Reviews Molecular Cell Biology*, 2 (793-805).
- Goldfinger, L., Tzima, E., Stockton, R., Kiosses, W. B., Kinbara, K., Tkachenko, E., Gutierrez, E., Groisman, A., Nguyen, P., Chien, S. & Ginsberg, M. H. 2008. Localized 4 integrin phosphorylation directs shear stress-induced endothelial cell alignment. *Circ. Res*, 103, 177–185.
- Goley, E. D. & Welch, M. D. 2006. The Arp2/3 complex: an actin nucleator comes of age. *Nature Reviews Molecular Cell Biology*, 7, 713–126.
- Goryachev, A. & Pokhilko, A. 2006. Computational model explains high activity and rapid cycling of Rho GTPases within protein complexes. *PLoS Computational Biology*, 2 (12), e172.
- Hawkins, B., Abbruscato, T., Egleton, R., Brown, R., Huber, J., Campos, C. & Davis, T. 2004. Nicotine increases in vivo blood-brain barrier permeability and alters cerebral microvascular tight junction protein distribution. *Brain Res*. 19 (1027(1-2)), 48–58.
- Hazel, A. & Pedley, T. 2000. Vascular endothelial cells minimize the total force on their nuclei. *Biophysical Journal*, 78, 47–64.
- Herant, M., Marganski, W. A. & Dembo, M. 2003. The mechanics of neutrophils: synthetic modeling of three experiments. *Biophysical Journal*, 84 (5), 3389–413.
- Herrmann, H., Bär, H., Kreplak, L., Strelkov, S. V. & Aebi, U. 2007. Intermediate filaments: from cell architecture to nanomechanics. *Nature Reviews Molecular Cell Biology*, 8, 562–573.
- Higdon, J. 1985. Stokes flow in arbitrary two-dimensional domains: shear flow over ridges and cavities. *J. Fluid. Mech.* 159, 195–226.
- Hoger, J. H., Ilyin, V. I., Forsyth, S. & Hoger, A. 2002. Shear stress regulates the endothelial kir2.1 ion channel. *PNAS*, 99 (1), 7780–5.
- Holmes, K., D.Popp, W.Gebhard & W.Kabsch 1990. Atomic model of the actin filament. *Nature*, 347, 44–49.

- Ingber, D. 2006. Cellular mechanotransduction: putting all the pieces back together again. *The FASEB Journal*, 20, 811–827.
- Jaffe, A. & Hall, A. 2005. Rho GTPases: biochemistry and biology. *Annu. Rev. Cell. Dev. Biol.*, 21, 247–69.
- Jalali, S., Li, Y.-S., Sotoudeh, M., Yuan, S., Li, S., Chien, S. & Shyy, J. Y.-J. 1998. Shear stress activates p60src-Ras-MAPK signaling pathways in vascular endothelial cells. *Arterioscler. Throm. Vasc. Biol.* 18, 227–234.
- Jilkine, A., Marèe, A. & Edelstein-Keshet, L. 2007. Mathematical model for spatial segregation of the Rho-family GTPases based on inhibitory crosstalk. *Bulletin of Mathematical Biology*, 69 (6), 1943–1978.
- Kamm, R. 2002. Cellular fluid mechanics. *Annu. Rev. Fluid Mech.* 34, 211–232.
- Katsumi, A., Wayne Orr, A., Tzima, E. & Schwartz, M. 2004. Integrins in mechanotransduction. *The Journal of Biological Chemistry*, 279 (13), 12001–12004.
- Kawano, Y., Fukata, Y., Oshiro, N., Amaon, M., Nakamura, T., Ito, M., Matsumura, F., Inagaki, M. & Kaiibuchi, K. 1999. Phosphorylation of myosin binding submit (mbs) of myosin phosphatase by Rho-kinase *in vivo*. *Journal of Cell Biology*, 147 (1023-1037).
- Keren, K., Pincus, Z., Allen, G. M., Barnhart, E. L., Marriott, G., Mogilner, A. & Theriot, J. A. 2008. Mechanism of shape determination in motile cells. *Nature*, 453 (7194), 475–480.
- Kim, T. 2007. *Simulation of Actin Cytoskeleton Structure and Rheology*. Massachusetts Institute of Technology, MSc Thesis.
- Kovar, D. 2006. Arp2/3 ATP hydrolysis: to branch or debranch? *Nature Cell Biology*, 8, 783–785.
- Kozlov, M. M. & Bershadsky, A. D. 2004. Processive capping by formin suggests a force-driven mechanism of actin polymerization. *Journal of Cell Biology*, 167 (6), 1011–7.
- Kumar, S., Maxwell, I., Heisterkamp, A., Polte, T. R., Lele, T., Salanga, M., Mazur, E. & Ingber, D. E. 2006. Viscoelastic retraction of single living stress fibres and its impact on cell shape, cytoskeletal organization and extracellular matrix mechanics. *Biophysical Journal*, 90, 3762–3773.

- Lennard-Jones, J. E. 1931. Cohesion. *Proc. Phys. Soc*, 43 (5), 461–482.
- Levine, H., Kessler, D. A. & Rappel, W.-J. 2006. Directional sensing in eukaryotic chemotaxis: a balanced inactivation model. *PNAS*, 103 (26), 9761–6.
- Lowan, A., Davids, N. & Levenson, A. 1942. Table of the zeros of the legendre polynomials of order 1-16 and the weight coefficients for gauss' mechanical quadrature formula. *Bulletin of the American Mathematical Society*, 48 (10).
- Lusis, A. 2000. Atherosclerosis. *Nature*, 407 (233-241).
- Lykostratis, K. 2005. *Mathematical modelling of shear stress signalling in endothelial cells*. PhD thesis, University College London.
- Marè, A., Jilkine, A., Grieneisen, A. D. V. & Edelstein-Keshet, L. 2006. Polarization and movement of keratocytes: a multiscale modelling approach. *Bulletin of Mathematical Biology*, 68, 1169–1211.
- Marshall, I., Papathanasopoulou, P. & Wartolowska, K. 2004. Carotid flow rates and flow division at the bifurcation in healthy volunteers. *Physiol. Meas.* 25, 691–697.
- Martinac, B. 2004. Mechanosensitive ion channels: molecules of mechanotransduction. *Journal of Cell Science*, 117, 2449–2460.
- Mathur, A. B., Truskey, G. A. & Reichert, W. M. 2000. Atomic force and total internal reflection fluorescence microscopy for the study of force transmission in endothelial cells. *Biophysical Journal*, 78, 1725–1735.
- Mazzag, B., Tamareisis, J. & Barakat, A. 2003. A model for shear stress sensing and transmission in vascular endothelial cells. *Biophysical Journal*, 84, 4087–4101.
- McCue, S., Danjnowiec, D., Xu, F., Zhang, M., Jackson, M. & Languille, B. L. 2006. Shear stress regulates forward and reverse planar cell polarity of vascular endothelium *in vivo* and *in vitro*. *Circ. Res.* 98, 939–946.
- Mogilner, A. & Edelstein-Keshet, L. 1996. Spatio-angular order in populations of self-aligning objects: formation of oriented patches. *Physica D*, 89, 346–367.
- Mogilner, A. & Oster, G. 1996. Cell motility driven by actin polymerisation. *Biophysical Journal*, 71, 3030–3045.
- Mott, R. E. & Helmke, B. P. 2007. Mapping the dynamics of shear stress-induced structural changes in endothelial cells. *AJP: Cell Physiology*, 293 (5), C1616–1626.

- Mullins, D., R., Heuser, J. & Pollard, T. 1998. The interaction of Arp2/3 complex with actin: nucleation, high affinity pointed end capping, and formation of branching networks of filaments. *Proc. Natl. Acad. Sci.* 95 (11), 6181–6186.
- Narang, A. 2006. Spontaneous polarization in eukaryotic gradient sensing: a mathematical model based on mutual inhibition of frontness and backness pathways. *Journal of Theoretical Biology*, 4 (21), 538–553.
- Narumiya, S. & Yasuda, S. 2006. Rho gtpases in animal cell mitosis. *Current Opinion in Cell Biology*, 18 (2), 199–205.
- Nimnual, A., Yatsula, B. & Bar-Sagi, D. 2003. Redox dependent downregulation of Rho by Rac. *Nat. Cell. Biol.* 5, 236–241.
- Nobes, C. & Hall, A. 1995. Rho, Rac and Cdc42 GTPases regulate the assembly of multimolecular focal complexes associated with actin stress fibres, lamellipodia and filopodia. *Cell*, 81, 53–62.
- Ohta, Y., Hartwig, J. & Stossel, T. 2006. FilGAP, a Rho- and ROCK-regulated GAP for Rac binds filamin a to control actin remodelling. *Nature Cell Biology*, 8, 803–814.
- Okud, M., Takahashi, M., Suero, J., Murry, C. E., O.Traub, Kawakatsu, H. & Berk, B. 1999. Shear stress stimulation of p130cas tyrosine phosphorylation requires calcium-dependent c-src activation. *The Journal of Biological Chemistry*, 274 (28), 26803–26809.
- Otsuji, M., Ishihara, S., Kaiibuchi, K., Mochizuki, A. & Kuroda, S. 2007. A mass conserved reaction-diffusion system captures properties of cell polarity. *PLoS Computational Biology*, 3 (6), 1040–1054.
- Pedley, T. 1980. *The Fluid Mechanics of Large Blood Vessels*. Cambridge University Press.
- Pellegrin, S. & Mellor, H. 2007. Actin stress fibres. *Journal of Cell Science*, 120, 3491–3499.
- Peng, J., Wallar, B., Flanders, A., Swiatek, P. & Albert, A. 2003. Disruption of the diaphanous-related formin drf1 gene encoding mdial reveals a role for drf3 as an effector for cdc42. *Current Biology*, 13 (7), 534–545.
- Pertz, O. & Hahn, K. M. 2004. Designing biosensors for rho family proteins — deciphering the dynamics of rho family gtpase activation in living cells. *Journal of Cell Science*, 117, 1313–1318.

- Peskin, C., Odell, G. & Oster, G. 1993. Cellular motions and thermal fluctuations: the brownian ratchet. *Biophysical Journal*, 65 (316-324).
- Polak, J., Kronmal, R., Tell, G., O'Leary, D., Savage, P., Gardin, J., Rutan, G. & Borhani, N. 1996. Compensatory increase in common carotid artery diameter. *Stroke*, 27, 2012–2015.
- Pollard, T., Mullins, R. & Blanchoin, L. 2000. Molecular mechanisms controlling actin filament dynamics in nonmuscle cells. *Annu. Rev. Biophys. Biomol. Struct.* 29, 545–576.
- Ponti, A., Machacek, M., Gupton, S. L., Waterman-Storer, C. M. & Danuser, G. 2004. Two distinct actin networks drive the protrusion of migrating cells. *Science*, 305, 1782–1786.
- Pozrikidis, C. 1992. *Boundary integral and singularity methods for linearized viscous flow*. Cambridge University Press.
- Pozrikidis, C. 1997. Shear flow over a protuberance on a plane wall. *Journal of Engineering*, 31, 29–42.
- Price, T. 1985. Slow linear shear flow past a hemispherical bump in a plane wall. *Q. J. Mech. Appl. Math*, 38 (93-104).
- Rathod, H., Nagaraja, K. & Ramesh, N. 2004. Gauss legendre quadrature over a triangle. *J. Indian. Inst. Sci*, 84, 183–188.
- Raucher, D. & Sheetz, M. P. 2000. Cell spreading and lamellipodial extension rate is regulated by membrane tension. *Journal of Cell Biology*, 148 (1), 127–136.
- Reese, J. & Thompson, D. 1998. Shear stress in arterial stenoses: a momentum integral model. *Journal of Biomechanics*, 31 (11), 1051–7.
- Ridley, A. 2001. Rho gtpases and cell migration. *Journal of Cell Science*, 114 (2713-2722).
- Ridley, A. 2006. Rho gtpases and actin dynamics in membrane protrusions and vesicle trafficking. *Trends Cell Biol.* 16 (10), 552–559.
- Ridley, A. & Hall, A. 1992. The small GTP-binding protein rho regulates the assembly of focal adhesions and actin stress fibres in response to growth factors. *Cell*, 70, 389–399.

- Riento, K. & Ridley, A. 2003. ROCKs: multifunctional kinases in cell biology. *Rev. Mol. Cell. Biol*, 4 (446-456).
- Riveline, D., Zamir, E., Balaban, N. Q., Schwarz, U. S., Ishizaki, T., Narumiya, S., Kam, Z., Geiger, B. & Bershadsky, A. D. 2001. Focal contacts as mechanosensors: externally applied local mechanical force induces growth of focal contacts by an mdial-dependent and rock-independent mechanism. *Journal of Cell Biology*, 153 (6), 1175–86.
- Robertson, R., Turbedsky, K., Kaiser, D., Marchand, J., Higgs, H., Choe, S. & Pollard, T. 2001. Crystal structure of Arp2/3 complex. *Science*, 294, 1679–1684.
- Ross, R. 1999. Atherosclerosis - an inflammatory disease. *Mechanism of Disease, The New England Journal of Medicine*, 340 (2), 115–126.
- Rottner, K., Hall, A. & Small, J. 1999. Interplay between Rac and Rho in the control of substrate dynamics. *Current Biology*, 9 (640-648).
- Rouiller, I., Xu, X.-P., Amann, K. J., Egile, C., Nickell, S., Nicastro, D., Li, R., Pollard, T. D., Volkman, N. & Hanein, D. 2008. The structural basis of actin filament branching by the Arp2/3 complex. *Journal of Cell Biology*, 5 (180), 887–895.
- Saad, Y. 1981. Krylov subspace methods for solving large unsymmetric linear systems. *Mathematics of Computation*, 37 (155), 105–126.
- Sablin, E., Dawson, J., VanLoock, M., Spudlich, J., Egelman, E. & Fletterick, R. 2002. How does ATP hydrolysis control actin's associations? *Proc. Natl. Acad. Sci.* 99 (17), 10945–10947.
- Sandersius, S. A. & Newman, T. J. 2008. Modeling cell rheology with the subcellular element model. *Physical biology*, 5 (1), 15002.
- Sastry, S. & Burridge, K. 2000. Focal adhesions: a nexus for intracellular signalling and cytoskeletal dynamics. *Experimental Cell Biology*, 261, 25–36.
- Sawada, Y., Tamada, M., Dubin-Thaler, B. J., Cherniavskaya, O., Sakai, R., Tanaka, S. & Sheetz, M. 2006. Force sensing by mechanical extension of the src family kinase substrate p130cas. *Cell*, 127, 1015–1026.
- Schafer, D. & Cooper, J. 1995. Control of actin assembly at filament ends. *Annu. Rev. Cell. Dev. Biol*, 11, 497–518.

- Schaub, S., Meister, J.-J. & Verkhovsky, A. 2006. Analysis of actin filament network organization in lamellipodia by comparing experimental and simulated images. *Journal of Cell Science*, 120, 1491–1500.
- Seabra, M. C. 1998. Membrane association and targeting of prenylated Ras-like GTPases. *Cellular Signalling*, 10 (3), 167–172.
- Shao, D., Forge, A., Munro, P. & Bailly, M. 2006. Arp2/3 complex-mediated actin polymerisation occurs on specific pre-existing networks in cells and requires spatial restriction to sustain functional lamellipod extension. *Cell Motility and the Cytoskeleton*, 63, 295–414.
- Sherratt, J. & Lewis, J. 1993. Stress-induced alignment of actin filaments and the mechanics of cyto gel. *Bulletin of Mathematical Biology*, 55 (3), 637–654.
- Siegmán, A. 1979. Simplified derivation of the fokker-planck equation. *American Journal of Physics*, 47 (6).
- Sima, A. V., Stancu, C. & Simionescu, M. 2009. Vascular endothelium in atherosclerosis. *Cell Tissue Research* 2009, 335, 191–203.
- Snapper, S. B., Takeshima, F., Antón, I., Liu, C.-H., Thomas, S. M., Nguyen, D., Dudley, D., Fraser, H., Purich, D., Lopez-Illasaca, M., Klein, C., Davidson, L., Bronson, R., Mulligan, R. C., Southwick, F., Geha, R., Goldberg, M. B., Rosen, F. S., Hartwig, J. H. & Alt, F. W. 2001. N-WASP deficiency reveals distinct pathways for cell surface projections and microbial actin-based motility. *Nature Cell Biology*, 3 (10), 897–904.
- Snelson, K. 2008. <http://www.kennethsnelson.net/>.
- Stamenovic, D., Fredberg, J., Wang, N., J.P. Butler & Ingber, D. E. 1996. A microstructural approach to cytoskeletal mechanics based on tensegrity. *J. Theor. Biol*, 181, 125–136.
- Suciu, A., Civelekoglu, G., Tardy, Y. & Meister, J. 1997. Model for the alignment of actin filaments in endothelial cells subjected to fluid shear stress. *Bulletin of Mathematical Biology*, 59 (6), 1029–1046.
- Svitkana, T. & Borisy, G. 1999. Arp2/3 complex and actin depolymerization factor/cofilin in dendritic organization and treadmilling of actin filament array in lamellipodia. *Journal of Cell Biology*, 145 (1009-1026).

- Takahashi, F., Higashino, Y. & Miyata, H. 2003. Probing of the cell peripheral movements by optical trapping technique. *Biophysical Journal*, 84 (2664–2670).
- Thi, M., Tarbell, J. M., Weinbaum, S. & Spray, D. 2004. The role of the glycocalyx in reorganization of the actin cytoskeleton under fluid shear stress: a "bumper-car" model. *Proc. Natl. Acad. Sci.* 101 (47), 16483–16488.
- Tyska, M. J., Dupuis, D. E., Guilford, W. H., Patlak, J. B., Waller, G. S., Trybus, K. M., Warshaw, D. M. & Lowey, S. 1999. Two heads of myosin are better than one for generating force and motion. *PNAS*, 96 (8), 4402–7.
- Tzima, E., del Pozo, M., Kiosses, W., Mohamed, S. & Schwartz, M. 2002. Activation of Rac1 by shear stress in endothelial cells mediates both cytoskeletal reorganization and effects on gene expression. *The EMBO Journal*, 21 (24), 6791–6800.
- Tzima, E., del Pozo, M., Shattil, S. J., Chien, S. & Schwartz, M. 2001. Activation of integrins in endothelial cells by fluid shear stress mediates Rho-dependent cytoskeletal alignment. *EMBO Journal*, 20 (17), 4639–4647.
- Tzima, E., Irani-Tehrani, M., Kiosses, W., Dejana, E., Schultz, D., Engelhardt, B., Cao, G., Delisser, H. & Schwartz, M. 2005. A mechanosensory complex that mediates the endothelial cell response to fluid shear stress. *Nature*, 437, 426–431.
- Üders, J. & Stearns, T. 2007. Microtubule-organizing centres: a re-evaluation. *Nature Reviews Molecular Cell Biology*, 8, 161–167.
- Underhill, P. & Doyle, P. 2004. On the coarse graining of polymers into bead-spring chains. *J. Non-Newtonian Fluid Mech.* 122 (2004), 3–31.
- VanTeefelen, J., Brands, J., Stroes, E. & H.Vink 2007. Endothelial glycocalyx: sweet shield of blood vessels. *Trens in Cardiovascular Medicine*, 17 (3), 101–15.
- Wade, R. & Hyman, A. 1997. Microtubule structure and dynamics. *Current Opinion in Cell Biology*, 9, 12–17.
- Wang, N. 1998. Mechanical interactions among cytoskeletal filaments. *Hypertension*, 32, 162–165.
- Wang, N., Butler, J. & Ingber, D. E. 1993. Mechanotransduction across the cell surface and through the cytoskeleton. *Science*, 260 (1124–1127).
- Wang, Y., Botvinick, E., Zhao, Y., Berns, M. W., Usami, S., Tsien, R. Y. & Chien, S. 2005. Visualizing the mechanical activation of Src. *Nature*, 434, 1040–1045.

- Wang, Y. & Dimitrakopoulos, P. 2006a. Nature of the hemodynamic forces exerted on vascular endothelial cells or leukocytes adhering to the surface of blood vessels. *Physics of Fluids*, 18, 087107–1.
- Wang, Y. & Dimitrakopoulos, P. 2006b. Normal force exerted on vascular endothelial cells. *Physical Review Letters*, 96, 028106–1.
- Weinbaum, S., Tarbell, J. & Daminano, E. 2007. The structure and function of the endothelial glycocalyx layer. *Annu. Rev. Biomed. Eng.* 9, 121–67.
- Weinbaum, S., Tzeghai, G., Ganatos, P., Pfeffer, R. & Chien, S. 1985. Effect of cell turnover and leaky junctions on arterial macromolecular transport. *Am. J. Physiol.* 248 (H945-H960).
- Weinbaum, S., Zhang, X., Han, Y., Vink, H. & Cowin, S. 2003. Mechanotransduction and flow across the endothelial glycocalyx. *Proc. Natl. Acad. Sci.* 100 (13), 7988–7995.
- Welch, M., Iwamatsu, A. & Mitchison, T. 1997. Actin polymerisation is induced by arp2/3 protein complex at the surface of *listeria monocytogenes*. *Nature*, 385 (265-268).
- Welch, M., J.Rosenblatt, Skoble, J., Portney, D. & Mitchison, T. 1998. Interaction of human arp2/3 complex and the *listeria monocytogenes* acta protein in actin filament nucleation. *Science*, 281, 105–108.
- Winder, S. & Ayscough, K. 2005. Actin-bundling proteins. *Journal of Cell Science*, 118 (651-654).
- Wojciak-Stothard, B. & Ridley, A. 2003. Shear stress-induced endothelial cell polarization is mediated by Rho and Rac but not Cdc42 or PI 3-kinases. *Journal of Cell Biology*, 161 (2), 429–439.
- Yamamoto, K., Korenaga, R., Kamiya, A. & Ando, J. 2000. Fluid shear stress activates Ca^{2+} influx into human endothelial cells via P2X4 purinoceptors. *Circ. Res.* 87, 385–391.
- Zhang, B., Wang, Z.-X. & Zheng, Y. 1997. Characterization of the interactions between the small GTPase Cdc42 and its GTPase-activating roteins and utative effectors. *J. Biol. Chem.* 272 (35), 21999–22007.

- Zhang, B., Zhang, Y., Wang, Z.-X. & Zheng, Y. 2000. The role of Mg^{2+} cofactor in the guanine nucleotide exchange and GTP-hydrolysis reactions of rho family gtp-binding proteins. *J. Biol. Chem.*, 275 (33), 25299–25307.
- Zheng, X., Diraviyam, K. & Sept, D. 2007. Nucleotide effects on the structure and dynamics of actin. *Biophysical Journal*, 93 (1277-1283).
- Zhou, H. & Pozrikidis, C. 1995. Deformation of liquid capsules with incompressible interfaces in simple shear flow. *Journal of Fluid Mechanics*, 283, 175–200.
- Zuo, X., J. Zhang, Y. Z., S. Hsu, D. Z. & Guo, W. 2006. Exo70 interacts with the Arp2/3 complex and regulates cell migration. *Nature Cell Biology*, 8 (1383-1388).

Index

- actin
 - branching, 43
 - bundling, 19
 - contraction, 19
 - crosslinking, 19
 - F-actin, 41
 - G-actin, 41
 - stress fibre alignment, 19
- Arnoldi Method, 83
- Arp2/3, 42
- Boundary Integral Representation
 - discretisation, 73
 - Reduced, 73
- Brownian dynamics, 46
- Brownian ratchet model, 44
- cytogel stress, 25
- cytoskeleton, 17
- delta function, 69
- formins, 38
- glycocalyx, 93
- Green's functions, 69
- integrins, 94
- integro-differential model, 27
 - extension, 30
 - stability, 33
- intermediate filaments, 18
- ion channels, 91
- Krylov Subspace, 82
- lamellipodia, 40
- Langevin equation, 46
- Lennard Jones potential, 46
- microtubules, 17
- Poiseuille, 66
- reciprocal identity, 69
- Reynold's number, 64
- Stokes equation, 67
- stress tensor, 67
- tensegrity, 20